EMERGING ABSORBER MATERIALS FOR SUSTAINABLE PHOTOVOLTAICS

by

Peter James Yates

Thesis submitted for the degree of Doctor of Philosophy

University of Liverpool

November 2018

Abstract

This thesis presents the work performed on emerging materials considered as candidates for the production of low cost, thin film photovoltaics using sustainable feedstock. The two materials investigated here were Cu_3BiS_3 and Sb_2Se_3.

Fabrication of Cu_3BiS_3 films by the sulfurisation of metal precursor films was thoroughly investigated. XRD was used to monitor the phases present in samples sulfurized in the temperature range 375-450°C and having pre-sulfurisation Cu:Bi ratios in the range 18:1 to 3:2. Once the conditions for growth of phase-pure material had been established, devices were grown in the substrate geometry using the structure glass/Mo/window/Cu_3BiS_3/ITO, where the window layer choices were ZnS and CdS. Devices with ZnS window layers rectified but did not produce measurable photocurrent. This lack of photocurrent was attributed to the Cu_3BiS_3 layer and speculated to be due to its high density of trap states observed in other work on the material.

Sb_2Se_3 film growth by physical vapour deposition was investigated, and in particular the relationship between substrate temperature and crystal texture. The material was found not to adhere to the well-known Structure Zone Model, whereby the grain morphology varies systematically with respect to substrate temperature expressed as a fraction of the melting point of the material. Instead the as-deposited films were found to be amorphous for substrate temperatures below 500°C, requiring post-growth annealing to promote a polycrystalline

microstructure. The orientation of the resulting films was found to be very sensitive to the post growth annealing conditions.

An extensive study of Sb_2Se_3 device fabrication and optimisation was performed. Firstly, the importance of the inclusion of a hole transport material was established and a post-P3HT deposition annealing step was found to further improve device performance. The annealing step required to produce crystalline Sb_2Se_3 films was optimised to increase device performance, the best conditions being 350°C in N_2 for 30 minutes. Window layers of ZnS, CdS, TiO_2 and a ZnS/CdS bilayer were investigated. ZnS was found unsuitable due to inability to extract photocurrent, whereas the other candidates all showed promise. The best window layer of was found to be the ZnS/CdS bilayer due to its increased EQE compared to the CdS only case. The variation of the device performance across a 5×5 cm^2 device plate was examined and areas of lower *PCE* correlated with those having low J_{sc}.

The highest performing Sb_2Se_3 devices made in this study had the structure: glass/SnO_2:F/ZnS/CdS/Sb_2Se_3/P3HT/Au, their structure was investigated by TEM and EDX. The champion device working parameters were: η = 5.04%, J_{sc} = 29.3 mA·cm^{-2}, V_{oc} = 380 mV and FF = 45.3%.

Declaration

With the exceptions listed below the results presented in this thesis were obtained by the author. The research here has not been submitted for any other degree.

The XPS measurements in Chapter 5 were performed by Thomas Whittles, University of Liverpool.

ToF SIMS measurements were performed by Mark A. Farnworth, Pilkington Group Ltd.

TEM and TEM/EDX measurements in Chapter 7 were performed by Karl Dawson, University of Liverpool.

Acknowledgements

First and foremost, I owe the utmost gratitude to my supervisor, Professor Ken Durose, for his support throughout my entire PhD; from his continuous guidance and expert ideas to his tireless efforts proof reading this thesis. Without his help this chunk of text would have been half as long and twice as incomprehensible.

Over the course of the last few years I have had the privilege of working with some truly fantastic people. Special thanks to Jonathan Major for his invaluable advice regarding all things device related. Thanks to Silvia Mariotti, Oliver Hutter, Laurie Phillips, Tom Whittles, and everyone else I've had the pleasure of collaborating with; to Enzo Peccerillo, Giorgos Papageorgiou, Annette Pressman, Tom Baines, Jack Swallow, Tom Shalvey, Theo Hobson and Huw Shiel for being great office, lab and drinking buddies.

I would also like to thank all the members of the members of the Stephenson Institute for Renewable Energy past and present for supplying such a wonderful working environment, and Vince Vasey especially for keeping the whole place running.

Finally, I am deeply grateful my parents, Steph and Tony, for their unwavering support throughout my continued education, for all their encouragement, and for always being at the other end of the phone when I need them.

Contents

1. Introduction 1
1.1 The global need for sustainable energy sources 1
1.2 Photovoltaic technologies 2
1.2.1 Overview 2
1.2.2 First generation 4
1.2.3 Second generation 4
1.2.4 Third generation 6
1.3 The solar spectrum 6
1.4 Motivations and considerations in seeking new absorber materials 7
1.5 Emerging PV absorber materials 9
1.6 Scope of this thesis 10
2. Solar cell and junction concepts 14
2.1 The p-n junction 14
2.2 The Shockley equation 17
2.3 Current-voltage behaviour 19
2.4 Power losses in photovoltaic cells 21
2.4.1 Fundamental losses 21
2.4.2 Recombination losses 21
2.4.3 Series and shunt resistances 21
2.4.5 Other losses 22
2.5 Photovoltaic device design 23
3. Literature on Cu_3BiS_3 and Sb_2Se_3 26
3.1 Cu_3BiS_3 26
3.2 Sb_2Se_3 30
4. Experimental methods 39
4.1 Growth techniques 39
4.1.1 Thermal evaporation 39
4.1.2 RF sputtering 40
4.1.3 Spin coating 41
4.1.4 Chalcogenisation 42
4.2 Material characterisation 43
4.2.1 UV-Vis-NIR 43

4.2.2 X-ray diffraction (XRD) 44
4.2.3 Scanning electron microscopy (SEM) 46
4.2.4 Transmission electron microscopy (TEM) 46
4.2.5 Energy dispersive X-ray (EDX) spectroscopy 47
4.2.6 Four-point probe 47
4.3 Device characterisation 48
4.3.1 Current-voltage (*J*-*V*) response 48
4.3.2 External quantum efficiency (EQE) 48
4.3.3 X-ray photoelectron spectroscopy (XPS) 48
4.3.4 Time of flight secondary ion mass spectroscopy (ToF SIMS) 49
4.3.5 Summary of characterisation techniques 49
5. Fabrication of Cu-Bi-S,Se films and device structures 52
5.1 Introduction 52
5.2 Experimental 53
5.2.1 Growth trials and formation of Cu_3BiS_3 53
5.2.2 Growth trials and formation of Cu-Bi-Se 55
5.2.3 Formation of devices 56
5.2.4 Characterisation 56
5.3 Results 56
5.3.1 Results of sulfurisation of metal stacks on glass 56
5.3.2 Formation of Cu_3BiS_3 films on Mo 73
5.3.3 Selenisation 76
5.4 Cu_3BiS_3 device structures and characterisation 78
5.5 Discussion 81
5.6 Conclusions 86
6. Growth of Sb_2Se_3 films 89
6.1 Introduction 89
6.2 Experimental 92
6.2.1 Film growth of Sb_2Se_3 92
6.2.2 Characterisation of Sb_2Se_3 films 94
6.3 Results 94
6.3.1 As-grown evaporated Sb_2Se_3 films on glass 94
6.3.2 Post-growth annealing of evaporated Sb_2Se_3 films 98
6.3.3 Growth of Sb_2Se_3 on InP (100) wafers 108
6.3.4 Growth of Sb_2Se_3 on RF sputtered CdS thin films 111
6.3.5 Comparison of Sb_2Se_3 post growth annealing in a furnace and on a hotplate 113

6.4 Discussion 116
6.5 Conclusions 123
7. Growth of Sb_2Se_3 devices 126
7.1 Introduction 126
7.2 Experimental methods 126
7.3 Results 129
    7.3.1 P3HT pinhole blocking layer 129
    7.3.2 Choice of window layer in evaporated Sb_2Se_3 devices 131
    7.3.3 Sb_2Se_3 post-growth annealing conditions 135
    7.3.4 Uniformity of evaporated Sb_2Se_3 devices 138
    7.3.5 Se- and Sb-rich Sb_2Se_3 devices by co-evaporation 142
    7.3.6 Champion Sb_2Se_3 device 146
7.4 Discussion 154
7.5 Conclusions 160
8. Summary, Conclusions and Suggestions for Future Work 164
8.1 Results summary 164
    8.1.1 Cu_3BiS_3 164
    8.1.2 Sb_2Se_3 films 164
    8.1.3 Sb_2Se_3 devices 165
8.2 Discussion and conclusions 165
    8.2.1 Cu_3BiS_3 165
    8.2.2 Sb_2Se_3 168
    8.2.3 Comparison of the two materials 171
8.3 Recommendations for future work 171

List of Publications

1. Phillips, L. J., Rashed, A. M., Treharne, R. E., Kay, J., Yates, P., Mitrovic, I. Z., Weerakkody, A., Hall, S. & Durose, K. Dispersion relation data for methylammonium lead triiodide perovskite deposited on a (100) silicon wafer using a two-step vapour-phase reaction process. *Data Br.* **5**, 926–928 (2015).

2. Phillips, L. J., Rashed, A. M., Treharne, R. E., Kay, J., Yates, P., Mitrovic, I. Z., Weerakkody, A., Hall, S. & Durose, K. Maximizing the optical performance of planar $CH_3NH_3PbI_3$ hybrid perovskite heterojunction stacks. *Sol. Energy Mater. Sol. Cells* **147**, 327–333 (2016).

3. Zhuang, Q. D., Alradhi, H., Jin, Z. M., Chen, X. R., Shao, J., Chen, X., Sanchez, A. M., Cao, Y. C., Liu, J. Y., Yates, P., Durose, K. & Jin, C. J. Optically efficient InAsSb nanowires for silicon-based mid-wavelength infrared optoelectronics. *Nanotechnology* **28**, (2017).

4. Mariotti, S., Hutter, O. S., Phillips, L. J., Yates, P. J., Kundu, B. & Durose, K. Stability and Performance of $CsPbI_2Br$ Thin Films and Solar Cell Devices. *ACS Appl. Mater. Interfaces* **10**, 3750–3760 (2018).

5. Phillips, L. J., Savory, C. N., Hutter, O. S., Yates, P. J., Shiel, H., Mariotti, S., Bowen, L., Birkett, M., Durose, K., Scanlon, D. O. & Major, J. D. Current enhancement via a TiO_2 window layer for CSS Sb_2Se_3 solar cells: performance limits and high Voc. *Ieee J. Photovoltaics* **Submitted**,

6. Whittles, T. J., Veal, T. D., Savory, C. N., Yates, P. J., Murgatroyd, P. A. E., Gibbon, J. T., Birkett, M., Potter, R. J., Major, J. D., Durose, K., Scanlon, D. O. & Dhanak, V. R. Band Alignments, Band Gap, Core-levels and Valence-Band States in Cu_3BiS_3 for Photovoltaics. *Manuscr. Prep.*

List of Figures

Figure 1.1: 2016 values for shares of electricity production from (a) all sources (b) renewable sources only. Data are taken from IEA. Key world energy statistics 2017.

Figure 1.2: Photovoltaics market share in the years 2000-2017 for the three main thin-film technologies.

Figure 1.3: AM1.5 solar spectrum.

Figure 1.4: Shockley-Queisser limit as a function of band gap.

Figure 1.5: Production rate and price of each of the elements considered here in the year 2017 as reported in the U.S. Geological Survey.

Figure 2.1: Diagram of a p-n junction.

Figure 2.2: Diagram of the energy levels in a homojunction a) before and b) after junction formation.

Figure 2.3: The energy levels before and after a heterojunction is between two materials with a) a negative conduction band offset and b) a positive conduction band offset. The offsets are denoted in green.

Figure 2.4: Generation and separation of an electron-hole pair in a p-n junction.

Figure 2.5: Equivalent circuit of an ideal solar cell.

Figure 2.6: Equivalent circuit of a solar cell with parasitic resistances.

Figure 2.7: Light J-V curve showing the location of each of the solar cell working parameters. The fill factor is the ratio of the areas of the red and grey boxes.

Figure 2.8: The effects of a) increasing series resistance and b) decreasing shunt resistance on the *J-V* response of a photovoltaic cell.

Figure 2.9: Example EQE responses from a device whose absorber and window layer materials have band gaps corresponding to wavelengths of λ_a and λ_w respectively and where λ_g is the wavelength corresponding to the band gap of the transparent conducting oxide. The black trace shows an ideal EQE response, the blue trace shows one with some parasitic absorption from the window layer, and the red trace shows a cell with a buried junction.

Figure 2.10: Schematic diagrams of a) superstrate device configuration and b) substrate device configuration.

Figure 3.1: The crystal structure of Cu_3BiS_3. a) the unit cell of wittichenite b) a CuS_3 structural unit c) the BiS_3 structural unit. Here the Cu atoms are represented in red, the Bi in blue and the S in yellow. These structures were produced using the VESTA software.

Figure 3.2: Ternary phase diagrams of the Cu-Bi-S system at 200 and 300°C, figure from Wang, 1994.

Figure 3.3: The crystal structure of Sb_2Se_3 a) the unit cell of Sb_2Se_3 b) a single chain of Sb_2Se_3 c) view down the covalently bonded c-axis. Here the Sb atoms are represented in blue and the Se in yellow. Recreated using the VESTA software.

Figure 3.4: The binary phase diagram for Sb and Se showing Sb_2Se_3 as the only binary phase. Reproduced from from Bordas *et al.*.

Figure 4.1: Schematic of the sputtering gun and the plasma confinement in a balanced magnetron.

Figure 4.2: A schematic diagram of the apparatus used for the chalcogenisation reactions.

Figure 4.3: The relationship between vapour pressure and temperature for S and Se.

Figure 4.4: A perfect crystal with spacing between planes, d_{hkl}, with the angle θ between the surface and the incident or diffracted beams.

Figure 5.1: Photograph of Cu-Bi-S samples on glass with Cu:Bi atomic ratios varying between 18:1 and 3:2, sulfurised at 375, 400 and 425°C. Precursor films sulfurised at 450°C left bare substrates and thus photographs are not included.

Figure 5.2: XRD spectra of Cu-Bi stacks sulfurised at 375°C with reference spectra for the target phase. Cu_3BiS_3, and other possible ternary, binary and elemental impurity phases. The Cu:Bi atomic ratio of the precursor films is indicated for each experimental XRD pattern. The desired phase was achieved with minimal impurity phases over the Cu:Bi range 9:5-9:2

Figure 5.3 XRD spectra of Cu-Bi stacks sulfurised at 375°C between 2θ angles of 16 and 22°, displaying the (020) and (111) peaks.

Figure 5.4: Segment of XRD spectrum from the 3:1 atomic Cu:Bi ratio film sulfurised at 375°C between 15 and 35° with the Cu3BiS3 reference spectrum.

Figure 5.5: SEM micrographs of 3:1 Cu:Bi ratio Cu_3BiS_3 films sulfurised at (a, b) 375°C, (c, d) 400°C, and (e, f) 425°C. The bright grains most visible in (a) and present in most of the other micrographs were due to charge artefacts.

Figure 5.6: SEM micrographs of 3:1 Cu:Bi ratio Cu_3BiS_3 films sulfurised at (a) 375°C and (b) 400°C. The grains annotated on each were used to estimate the average grain size in the films.

Figure 5.7: XRD spectra of Cu-Bi stacks sulfurised at 400°C with reference spectra for the target phase. Cu_3BiS_3, and other possible ternary, binary and elemental impurity phases. The Cu:Bi atomic ratio of the precursor films is indicated for each experimental XRD pattern. There is a smaller window of successful growth of low impurity films than seen in the 375°C analogue consisting of the four samples in the Cu:Bi range 9:4-18:5.

Figure 5.8: XRD spectra of Cu-Bi stacks sulfurised at 425°C with reference spectra for the target phase. Cu_3BiS_3, and other possible ternary, binary and elemental impurity phases. The Cu:Bi atomic ratio of the precursor films is indicated for each experimental XRD pattern. At this temperature only the 18:7 Cu:Bi ratio film was free of secondary phases.

Figure 5.9: Tauc plots for films of atomic Cu:Bi ratio of 3:1 and 9:4 sulfurised at 375°C and 400°C plotted as (a) direct allowed, (b) indirect allowed, (c) direct forbidden, and (d) indirect forbidden band gaps. Solid lines represent the optical data and dashed lines the extrapolation of the best estimate to the linear portions of each curve.

Figure 5.10: SEM micrograph of a 9:4 atomic Cu:Bi precursor ratio film on a Mo substrate, sulfurised at 375°C. The bright contrast grains are charge artefacts on the surface.

Figure 5.11: XRD spectra of Cu-Bi-S films with sulfurised from (a) Cu:Bi 9:4 on glass, (b) Cu:Bi 9:4 on Mo and (c) Cu:Bi 3:1 on Mo. Peaks marked belong to the Mo layer. Cu_3BiS_3 reference peaks are shown on underneath.

Figure 5.12: XRD spectra of selenised Cu, Bi, and Cu-Bi films. Reference spectra for the elemental constituents, the binary compounds and a potential ternary phase are also shown.

Figure 5.13: Band line-up for Cu_3BiS_3, CdS, and ZnS.

Figure 5.14: J-V responses of (a) glass/Mo/Cu_3BiS_3/CdS/ITO and (b) glass/Mo/Cu_3BiS_3/ZnS/ITO devices under AM1.5 illumination (solid line) and in the dark (dashed line).

Figure 6.1: Grain structure in each zone according to the Structure Zone Model. Replicated from Grovenor *et al.*.

Figure 6.2: XRD spectra of evaporated Sb_2Se_3 films grown on glass with substrate temperatures ranging from 24°C to 550°C. The films are amorphous in nature until substrate temperatures of 500°C are reached, above which they become crystalline. The spectra for the layers showing crystalline peaks have been background subtracted for clarity. Sb_2Se_3 reference peaks are shown at the bottom of the figure.

Figure 6.3: XRD spectra of Sb2Se3 evaporated onto glass substrates at 500 and 550°C without background subtraction or normalisation performed. Sb_2Se_3 reference peaks are shown at the bottom of the figure.

Figure 6.4: Tauc plots for Sb_2Se_3 films evaporated onto glass at substrate temperatures ranging from room temperature to 550°C. They clearly display a reduction of the band gap upon the appearance of polycrystalline structure above 500°C.

Figure 6.5: Effect of post-growth annealing on the XRD patters of Sb_2Se_3 films evaporated onto glass at a) room temperature, b) 150°C and c) 250°C. The annealing took place under nitrogen at 350°C. The Sb2Se3 reference peaks are shown underneath the experimental data.

Figure 6.6: XRD comparison of room temperature grown films (24°C). (a) evaporation run #1, annealing run #1 (b) evaporation run #1, annealing run #2 and (c) evaporation run #2, annealing run #2. Sb_2Se_3 reference peaks are shown underneath.

Figure 6.7: XRD of Sb_2Se_3 films grown on glass simultaneously at 150°C and then post-growth annealed separately at 350°C.

Figure 6.8: XRD of Sb_2Se_3 films grown on glass simultaneously at 250°C and then post-growth annealed separately at 350°C in runs a) and b). Sb_2Se_3 reference peaks are shown underneath.

Figure 6.9: SEM micrographs of Sb_2Se_3 films deposited by thermal evaporation. Shown here are the as grown case (a), film annealed at 350°C for 30 minutes on a hotplate in a N_2 atmosphere (b), and 400°C for 30 minutes on a hotplate in a N_2 atmosphere (c).

Figure 6.10: XRD spectra of Sb_2Se_3 films deposited onto room temperature (100) InP wafers and annealed at 250-400°C. The large peaks at 2θ values of 30.5 and 63.4° belong to the (200) and (400) planes of InP respectively. Sb_2Se_3 reference peaks are shown underneath.

Figure 6.11: XRD spectra of (a) CdS RF sputtered onto TEC15 glass to be used as substrates for the Sb2Se3 films (b) Sb_2Se_3 deposited onto CdS substrates (c) Sb2Se3 deposited onto CdS substrates and annealed at 350°C on a hotplate for 30 minutes in a N_2 atmosphere, and (d) Sb_2Se_3 deposited onto soda-lime glass and annealed at 350°C on a hotplate for 30 minutes in a N2 atmosphere. Sb_2Se_3 reference peaks are shown underneath.

Figure 6.12: Thermally evaporated Sb_2Se_3 films on (a) soda-lime glass (b) RF sputtered CdS on TEC15 glass and (c) (100) InP wafers. Post growth annealing was performed on each for 30 minutes at 350°C in box furnace with N_2 feed in (left) and on a hotplate in a N_2 atmosphere (right).

Figure 6.13: XRD spectra of Sb_2Se_3 films deposited onto RF Sputtered CdS films pre- and post-annealing at 350°C for 30 minutes in a box furnace with a N_2 feed in. Sb_2Se_3 reference peaks are shown underneath.

Figure 6.14: XRD spectra of Sb_2Se_3 films deposited onto (100) InP wafers pre- and post-annealing at 350°C for 30 minutes in a box furnace with a N_2 feed in. Sb_2Se_3 reference peaks are shown underneath.

Figure 7.1: *J-V* response under AM1.5 from (a) Sb_2Se_3 device without P3HT or the annealing step (b) Sb_2Se_3 device without P3HT but with the 150°C anneal (c) Sb_2Se_3 device with a P3HT pinhole blocking layer but no anneal (d) Sb2Se3 device with a P3HT pinhole blocking layer and 150°C anneal.

Figure 7.2: Box plots for the *PCE*, J_{sc}, V_{oc}, and *FF* of devices with the P3HT pinhole blocking layer both with and without the drying step.

Figure 7.3: *J-V* responses under AM1.5 from devices with CdS, ZnS or TiO_2 as a window layer.

Figure 7.4: *J-V* response from the TiO_2 device taken over consecutive days, the initial measurement being 3 days after the growth of the device.

Figure 7.5: ToF SIMS of a CdS/Sb_2Se_3 device.

Figure 7.6: ToF SIMS of a TiO_2/Sb_2Se_3 device.

Figure 7.7: J-V response of typical Sb_2Se_3 devices with respect to the post-growth annealing temperature.

Figure 7.8: Box plots for the *PCE*, J_{sc}, V_{oc}, and *FF* of Sb_2Se_3 devices with respect to the temperature of the post-growth anneal.

Figure 7.9: Distribution of values for *PCE*, J_{sc}, V_{oc} and *FF* in a typical 25 cm^2 CdS/Sb_2Se_3 device.

Figure 7.10: Distribution of values for *PCE*, J_{sc}, V_{oc} and *FF* in a typical 5×5 cm^2 TiO_2/Sb_2Se_3 device.

Figure 7.11: XRD spectra from (a) a CdS-coated substrate, (b) a Se-rich Sb_2Se_3 device structure after the annealing step, (c) a standard Sb_2Se_3 device structure after the annealing step and (d) a Sb-rich Sb_2Se_3 device structure after a 350°C annealing step. Literature data for S_2Se_3, Sb and Se are shown underneath.

Figure 7.12: *PCE*, J_{sc}, V_{oc} and *FF* of Se-rich devices annealed at 300, 350, and 400°C.

Figure 7.13: *PCE*, J_{sc}, V_{oc} and *FF* of Sb-rich devices annealed at 300, 350, and 400°C.

Figure 7.14: *PCE*, J_{sc}, V_{oc} and *FF* of pure Sb_2Se_3 devices annealed at 300, 350, and 400°C.

Figure 7.15: J-V response in the dark and under AM1.5 of the champion TEC15/ZnS/CdS/Sb_2Se_3/P3HT/Au device made in this work.

Figure 7.16: EQE data for the champion devices having CdS and Zns/CdS window layers. Both responses have been normalised.

Figure 7.17: STEM dark field of the Sb_2Se_3 chains a) is the image as-acquired b) is the image after FFT filtering c) is the FFT of the image and d) is the VESTA model of Sb_2Se_3 viewed down the a-axis to match the beam direction in the TEM images.

Figure 7.18: STEM image of a grain boundary in the Sb_2Se_3 layer.

Figure 7.19: STEM image of the region for EDX analysis.

Figure 7.20: STEM/EDX data for the main elements in the SnO_2:F/ZnS/CdS/Sb_2Se_3/P3HT/Au structure. The scale bar represents 200 nm.

List of Tables

Table 2.1: Criteria for selection of layers in the photovoltaic device.

Table 4.1: Experimental techniques used in this thesis for the purpose of characterising films and devices.

Table 5.1: Texture analysis on the XRD spectrum taken from the 3:1 atomic Cu:Bi ratio film sulfurised at 375°C.

Table 5.2: Sizes of grains indicated in Figure 5.6 and average of these values used to estimate the average grain size in films sulfurised at 375 and 400°C.

Table 5.3: Best estimates of the energy for each of the potential optical transitions explored in the Tauc plots in Figure 5.9.

Table 5.4: Possible candidates for the XRD peak at 43.6° observed in Cu_3BiS_3 films on Mo sulfurised at 375°C from precursor stacks with Cu:Bi atomic ratio 9:4. The XRD data were from the American Mineralogist Crystal Structure Database.

Table 5.5: Selenisation conditions for the Cu-Bi-Se films grown. In all cases 100 mg of elemental Se and a background N_2 pressure of 300 Torr were used.

Table 5.6: Calculations for the Gibbs free energy for the formation of each of the binary compounds covered in Equations 5.1 and 5.2.

Table 6.1: XRD data for as-grown Sb2Se3 films grown on glass at 500 and 550°C (see also Fig. 6.1). The texture coefficients (TC) indicate that the 500°C film is highly oriented (020) while the 550°C is not.

Table 6.2: Texture coefficients for each of the indexed peaks in the films grown on room temperature substrates (24°C). The letters a, b and c correspond to the XRD spectra shown in Figure 6.6. Films b) and c) were post growth annealed simultaneously and show similar texture coefficients.

Table 6.3: Texture coefficients for each of the indexed peaks in the XRD patterns from films grown at 150°C and then post-growth annealed as shown in Figure 6.7.

Table 6.4: Texture coefficients for each of the indexed peaks in the XRD patterns from films grown at 250°C shown in Figure 6.8.

Table 6.5: Texture coefficients for each of the peaks analysed in the Sb_2Se_3 film grown on InP wafers shown in Figure 6.10. TC values are calculated from the spectra for the as grown films and for those anneal post deposition at temperature in the range 250-400°C.

Table 6.6: Texture coefficients for each of the indexed peaks in the films grown on room temperature substrates shown in Figure 6.11.

Table 6.7: Summary of substrates used for Sb_2Se_3 growth, preparation conditions for the substrates pre-Sb_2Se_3 deposition, and details on the crystallinity of the resulting Sb_2Se_3 films before and after the post-growth anneal.

Table 7.1: Values of PCE, J_{sc}, V_{oc}, and FF for the highest efficiency Sb_2Se_3 PV devices made using CdS and TiO_2 window layers.

Table 7.2: Values of PCE, J_{sc}, V_{oc}, and FF for the highest efficiency pixel in the TiO_2/Sb_2Se_3 devices.

Table 7.3: Maximum, average and standard deviation for PCE, J_{sc}, V_{oc} and FF for a 25 cm^2 CdS/Sb_2Se_3 device having an array of 48 contacts.

Table 7.4: Maximum, average and standard deviation for *PCE*, J_{sc}, V_{oc} and *FF* for a 5×5 cm^2 TiO_2/Sb_2Se_3 device having an array of 64 contacts.

Table 7.5: Working parameters for the most efficient TEC15/CdS/Sb_2Se_3/P3HT/Au and TEC15/ZnS/CdS/Sb_2Se_3/P3HT/Au devices produced in this work.

Table 7.6: Average working parameters for the cells on the device plate belonging to the champion 5.04% TEC15//ZnS/CdS/Sb_2Se_3/P3HT/Au device.

Table 7.7: A summary of the optimisation steps carried out for evaporated Sb_2Se_2 PV devices.

List of Abbreviations

BF STEM	Bright Field STEM
CBD	Chemical Bath Deposition
CCD	Charge Coupled Device
CD	Conduction Band
CIGS	Copper Indium Gallium Selenide
CSS	Close Space Sublimation
CVD	Chemical Vapour Deposition
CZTS	Copper Zinc Tin Sulfide
DF STEM	Dark Field STEM
DFT	Density Functional Theory
DI	Deionised
EDX	Energy Dispersive X-ray
EQE	External Quantum Efficiency
FF	Fill Factor
FFT	Fast Fourier Transform
FIB	Focused Ion Beam
FTO	Fluorine Tin Oxide
HTM	Hole Transport Material
IPA	Propan-2-ol
ITO	Indium Tin Oxide
LPCVD	Low Pressuse Chemical Vapour Deposition
OPV	Organic Photovoltaics
PCE	Power Conversion Efficiency
PV	Photovoltaics
PVD	Physical Vapour Deposition
QCM	Quartz Crystal Microbalance
RTE	Rapid Thermal Evaporation
SEM	Scanning Electron Microscopy
SILAR	Successive Ionic Layer Adsorption and Reaction
SLME	Spectral Limited Maximum Efficiency
STEM	Scanning Transmission Electron Microscopy
SZM	Structure Zone Model
TCO	Transparent Conducting Oxide
TEM	Transmission Electron Microscopy
ToF SIMS	Time of Flight Secondary Ion Mass Spectroscopy
UV-Vis-NIR	Ultraviolet-Visible-Near Infrared
VB	Valence Band
VTD	Vapour Transport Deposition
XPS	X-ray Photoemission Spectroscopy
XRD	X-ray Diffraction

1. Introduction

1.1 The global need for sustainable energy sources

The global population, as of 2018, exceeds 7.5 billion people[1] and is unlikely to stop increasing, leading to an ever increasing energy demand. The UN declares "the right to development is an inalienable human right and that equality of opportunity for development is a prerogative both of nations and of individuals who make up nations"[2] and several authors describe having adequate energy as a key requirement for societal development[3–5].

In the BP Statistical Review of World Energy for 2018[6] the R/P ratios (i.e. the ratio of known reserves to yearly production and hence a measure of years' supply remaining at current consumption rates) for oil, gas and coal were 50.2, 52.6 and 134 respectively. Furthermore, the Intergovernmental Panel on Climate Change has recently recommended the target of limiting global warming to 1.5°C[7] (rather than their previous recommendation of 2°C) to avoid irreversible changes to the environment, such as the irreparable damage to ecosystems. It is therefore imperative to seek alternative, renewable, low-carbon alternatives to fossil fuels.

Taking the Sun as a perfect black body emitter at 5800 K, 174×10^{15} W is incident on the Earth's outer atmosphere with an average energy flux of 1367 $W\cdot m^{-2}$ [8]. This diminishes to a global-average solar irradiance of approximately 183 $W\cdot m^{-2}$ when atmospheric interaction, oblique incidence, seasonal and diurnal variations, and weather conditions are accounted for (equivalent to an average total power of approximately 23×10^{15} W)[9]. The total global electricity generation estimated by the International Energy Agency for 2015 was 24,255

TWh – equivalent to an average power demand of 2.76×10^{12} W.[10] Therefore, the global electricity demand is outweighed by solar insolation by a factor of approximately 10^4 and thus harnessing it by means of photovoltaics is an extremely attractive prospect.

1.2 Photovoltaic technologies

1.2.1 Overview

In 2016 the share of electricity generated by renewable sources was a total of 23.7%. Figure 1.1a shows the complete breakdown of electricity generation from all sources and Figure 1.1b shows the share of the global electricity across all renewable sources, the majority of which coming from hydroelectric (4,170 TWh of the 5,939 TWh renewables total). Solar photovoltaic accounted for 328 TWh of the global electricity production and while this is a small contribution compared to those of hydro and wind, the annual rate of increase is remarkable. In 2005 the total global electricity contribution from solar photovoltaics (PV) was only 4 TWh total (for comparison, the 2005 and 2016 values for wind electricity production were 104 and 958 TWh respectively)[10].

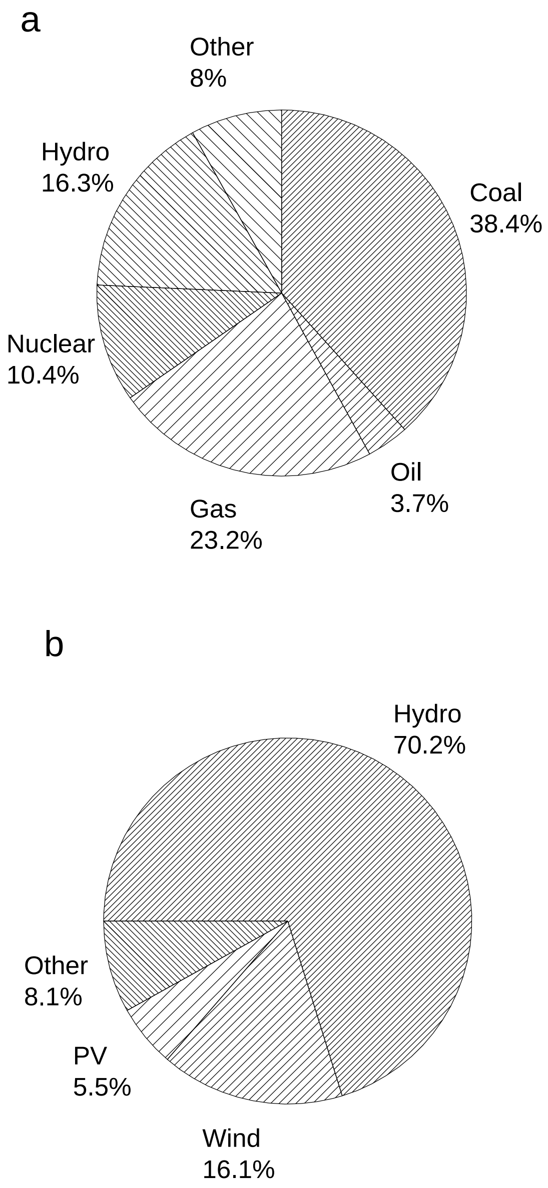

Figure 1.1: 2016 values for shares of electricity production from (a) all sources (b) renewable sources only. Data are taken from IEA. Key world energy statistics 2017[10].

As noble as the goal of providing clean, sustainable energy is, the main driver for change is likely to be cost. As such, solar PV must strive to outperform fossil fuel technologies sufficiently enough to provide ample financial incentive to replace the already established modes of energy generation.

Solar PV technologies are often separated into three generations. The first generation technologies are wafer based and are currently the most commercially viable technologies. Second generation materials are thin-film absorbers; polycrystalline materials with higher absorption coefficient which aim to reduce module cost with reduced processing energy and material requirement. Finally, the third generation umbrella covers those technologies which surpass the Shockley-Queisser limit of performance that applies to first and second generation devices. An alternative definition of third generation PV, and the one that will be used in this thesis is to include all technologies which do not belong to the first two categories.

1.2.2 First generation

The archetypal solar module is made from crystalline silicon (c-Si). A well-established technology, c-Si boasts high efficiencies (with verified records of 26.7% [11] and 21.9% [12] for mono- and multicrystalline devices respectively). In addition to high performance, Si has the benefit of being one of the most abundant elements on Earth. The major disadvantages of c-Si come in the forms of high purification energy requirements, poor light absorption (due to its indirect band gap) leading to high thickness requirements and large excess materials usage due to “kerf losses” from sawing ingots into wafers.

1.2.3 Second generation

Thin-film technologies aim to reduce the material requirement by using strong light absorbers. The most successful thin-film technologies are more tolerant to impurities and defects than c-Si. These two factors combined result in lower costs and energy payback times (EPBT, i.e. the number of years for the modules to generate the energy spent in their production) for these thin-film solar modules.

Both CdTe and CIGS now have record efficiencies exceeding 20%: 21.0%[13] and 22.9%[14] respectively. These two technologies, alongside the less efficient (having a record efficiency of 10.2%[15]) amorphous silicon (a-Si), represent the majority of the thin film market. While a-Si held the largest portion of the thin-film market for some years the advancement of commercial CdTe devices have reduced it to near-obsolescence outside of niche applications. As of 2007 CdTe has greater production than both a-Si and CIGS combined. Both the CdTe and CIGS technologies are limited with a view to scaling up to production quantities rivalling c-Si by the scarcity or high demand of some of their constituent elements (most notably Te, Ga and In).

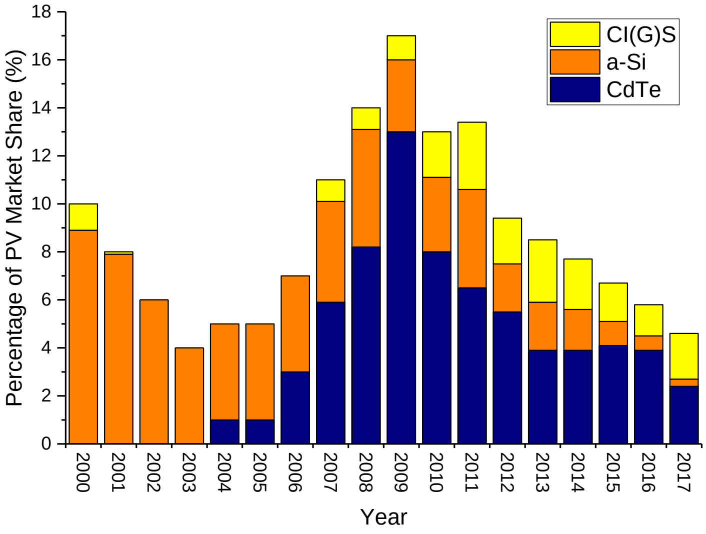

Figure 1.2: Photovoltaics market share in the years 2000-2017 for the three main thin-film technologies[16].

1.2.4 Third generation

The third generation technologies have less in common with the two previous generations. The two main candidates here for terrestrial applications are organic solar cells (OPV) and the perovskite family of solar cells. Both of these cases seek to reduce production energy and cost by the use of cheap precursors and solution processing and therefore the EPBT. While low EPBTs are attractive, the low stability of the polymers compromises the lifetime of the cells. Furthermore, the record efficiency of a single-junction OPV device is 11.2% [17]. Perovskites, however, boast an efficiency (20.9% reported in 2015[18]) which is especially impressive given the infancy of the field. Their stability issues, however, are even more extreme than those of OPV[19,20]. Resultantly, these technologies will require significant breakthroughs to begin to compete with c-Si, CdTe and CIGS.

1.3 The solar spectrum

The radiation output of the Sun may be approximated to that of a black body emitter at 5800 K. This spectrum is, in practice, altered by the variation in temperature across the surface of the Sun, as well as attenuation due to absorption in the Earth’s atmosphere. The extent of this attenuation is dependent on the distance travelled though the atmosphere and the spectrum arriving at the Earth’s surface, therefore, varies with latitude. The concept of “air mass” (AM) is a convenient notation for the spectrum arriving at a given latitude. AM0 is the spectrum arriving at the outer atmosphere and AM1 is the spectrum arriving at the equator. Conventionally AM1.5 is used for the evaluation of photovoltaic devices since it corresponds to a region of high population density.

The AM1.5 spectrum is shown in Figure 1.3. By convention the total intensity of the AM1.5 spectrum used for testing terrestrial solar cells is 100 mW·cm^2.

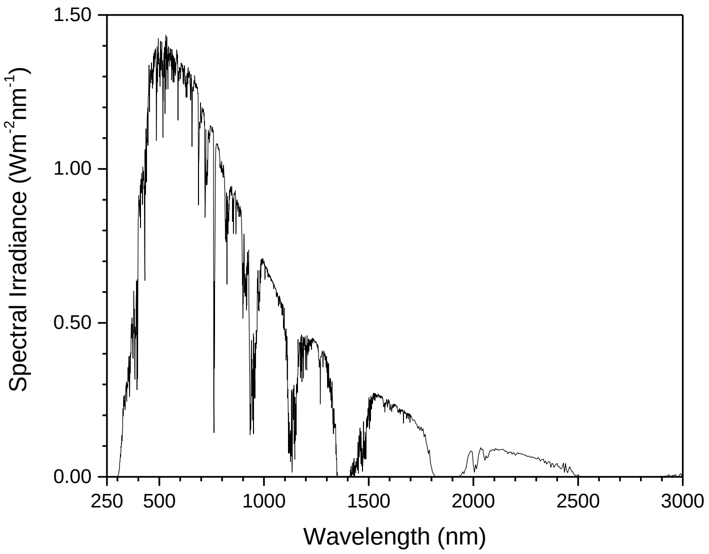

Figure 1.3: AM1.5 solar spectrum[21].

1.4 Motivations and considerations in seeking new absorber materials

When considering new materials for investigation as absorbers for solar PV the main concerns which need to be addressed are: production cost, abundance of the constituent elements, stability and material properties. The simplest way to ensure reasonable production costs is to target thin-film technologies for the reasons discussed in Section 1.2.3. Stability concerns can be somewhat reduced by investigating inorganic materials.

When choosing a new absorber material for solar PV the material properties must be considered. The primary consideration for assessing the potential of a new material is the band gap. The Shockley-Queisser (SQ) limit is the upper bound for efficiency of a solar cell given the band gap of the absorber[22]. If the band gap is too wide the number of photons in the solar spectrum which can be absorbed is low and the current from the device will be limited. If the band gap is too narrow, however, a large number of photons may be absorbed allowing for a high current but limiting instead the energy extracted from each absorbed photon and hence the voltage of the device. There is therefore an optimum band gap of for terrestrial applications. The Shockley-Queisser limit as a function of band gap is shown in in Figure 1.4. Taking 30% as a minimum limit value for desirable band gaps gives a range of 1.0-1.6 eV.

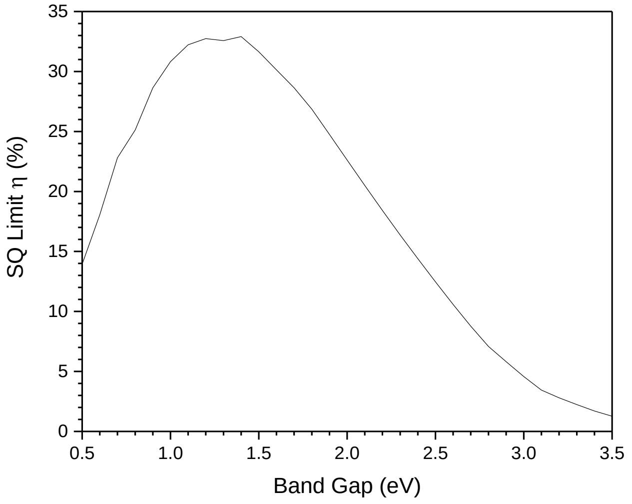

Figure 1.4: Shockley-Queisser limit as a function of band gap[23].

Further to this, for scale-up, more sustainable material options are desirable. The sustainability not only relies on the Earth-abundance of the constituent elements but also their price (usually dependent on market demand due to other applications, e.g. transparent conductors for In). A comparison of the prices and production rate of the elements in CIGS, CdTe and the materials investigated in this work is shown in Figure 1.5.

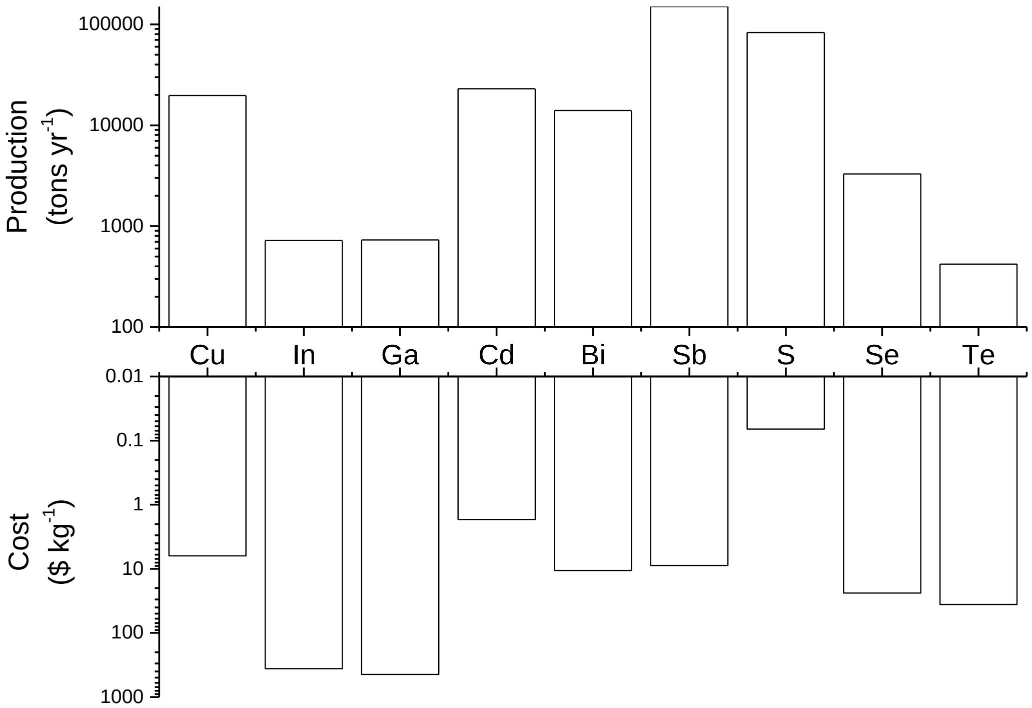

Figure 1.5: Production rate and price of each of the elements considered here in the year 2017 as reported in the U.S. Geological Survey[24].

1.5 Emerging PV absorber materials

Among the emerging PV absorber materials investigated are CZTS, FeS_2 and SnS:

CZTS is a quarternary material, already making phase control difficult, and the similar radii of Cu and Zn lead to cation disorder and therefore the presence of a mixture of the two $Cu_2ZnSn(S_xSe_{1-x})_4$ structures – kesterite being the desired structure and stannite being unwanted[25]. While this material is somewhat promising having reached 12.6% efficiencies[26], research has tailed off and interest has plateaued somewhat.

FeS_2 is a narrow band gap (0.95 eV), strongly absorbing ($\alpha > 10^5$ cm^{-1}) material made of cheap and abundant materials. A single crystal photoelectrochemical cell was reported in 1993 to be 2.8% efficient, however the V_{oc} was very low (187 mV)[27]. Interest in the material has recently picked up again with the investigation of colloidal quantum dot cells. These are yet to demonstrate any compelling results, Steinhagen stating in their report that the material easily forms sulfur vacancies at the surface of the nanoparticles resulting in electronic properties which are difficult to control [28].

SnS is another material with a favourable band gap (≈1.1 eV) and absorption ($\alpha > 10^4$ cm^{-1}). The record efficiency of SnS devices jumped from 2.04%[29] to 4.36%[30] by the authors' addressing of several issues in their 2.04% device. They target the grain size by annealing in H_2S, band structure at the interface by optimising the composition of the Zn(O,S) window layer, doping the window layer with nitrogen to reduce carrier concentration and improve diode quality and recombination at the interface by the addition of a few monolayers of SnO_2 between the absorber and window layer. These devices were deposited by atomic layer deposition, so are not particularly scalable, however a 3.88% device has been reported to have been produced by thermal evaporation [31].

1.6 Scope of this thesis

This thesis will commence with a summary of the basic principles of PV in Chapter 2, a review of the literature on each of the materials investigated in this thesis is presented in Chapter 3. Chapter 4 describes the thin film deposition methods, processing procedures, and the analytical techniques used for analysis of thin films and device performance. Chapters 5, 6 and 7 present the results and discussion of the work done for this thesis and Chapter 8 includes a brief summary of the work, general discussion, conclusions and suggestions for future work.

The results chapters cover the following topics:

Chapter 5 focuses on Cu_3BiS_3. Both the growth of films and their incorporation into full device structures are explored. Films were grown by a 2-step “sulfurisation” process whereby stacks of the metallic elements were annealed in a sulfur atmosphere. Devices were grown in the substrate orientation.

Chapter 6 details the growth of Sb_2Se_3 films by thermal evaporation. The crystallinity of the films was investigated after both the growth process and the post-growth annealing process. The crystallographic orientation of the films was investigated as a function of growth and annealing conditions.

Chapter 7 describes the incorporation of the thermally evaporated Sb_2Se_3 films into superstrate configuration devices and their characterisation. The effect of the following on device performance was investigated: the need for a pinhole blocking layer, the effect of the temperature of the post-growth annealing step, the variability across device plates, the effects of off-stoichiometric growth and the choice of window layer.

References for Chapter 1

1. UNFPA. World Population Report. (2018). Available at: https://www.unfpa.org/data/world-population-dashboard.

2. UN. Declaration on the right to development. (1986). Available at: http://www.un.org/documents/ga/res/41/a41r128.htm.

3. White, Leslie, A. Emergy and the evolution of culture. *Am. Anthropol.* **45**, 369–389 (1943).

4. Cottrell, F. *Energy and society: the relation between energy, social changes, and economic development*. (McGraw Book Company, 1955).

5. Lambert, J. G., Hall, C. A. S., Balogh, S., Gupta, A. & Arnold, M. Energy, EROI and quality of life. *Energy Policy* **64**, 153–167 (2014).

6. BP. Statistical review of world energy. (2018). Available at: https://www.bp.com/content/dam/bp/en/corporate/pdf/energy-economics/statistical-review/bp-stats-review-2018-full-report.pdf.

7. IPCC. IPCC press release 8 October 2018. 13–16 (2018). Available at: https://www.ipcc.ch/pdf/session48/pr_181008_P48_spm_en.pdf.

8. Markvart, T. *Solar Electricity*. (John Wiley & Sons, 2000).

9. Jean, J., Brown, P. R., Jaffe, R. L., Buonassisi, T. & Bulović, V. Pathways for solar photovoltaics. *Energy Environ. Sci.* **8**, 1200–1219 (2015).

10. IEA. Key world energy statistics 2017. (2017). Available at: https://www.iea.org/publications/freepublications/publication/KeyWorld2017.pdf.

11. Yoshikawa, K., Kawasaki, H., Yoshida, W., Irie, T., Konishi, K., Nakano, K., Uto, T., Adachi, D., Kanematsu, M., Uzu, H. & Yamamoto, K. Silicon heterojunction solar cell with interdigitated back contacts for a photoconversion efficiency over 26%. *Nat. Energy* **2**, (2017).

12. Benick, J., Richter, A., Müller, R., Hauser, H., Feldmann, F., Krenckel, P., Riepe, S., Schindler, F., Schubert, M. C., Hermle, M., Bett, A. W. & Glunz, S. W. High-Efficiency n-Type HP mc Silicon Solar Cells. *IEEE J. Photovoltaics* **7**, 1171–1175 (2017).

13. First Solar. First Solar builds the highest efficiency thinfilm PV cell on record. (2014). Available at: http://files.shareholder.com/downloads/FSLR/0x0x773989/5f8cc8fe-7d05-4c4d-b8e8-78206cede53d/FSLR_News_2014_8_5_English.pdf.

14. Solar Frontier. Solar Frontier Achieves World Record Thin-Film Solar Cell Efficiency of 22.9%. (2017).

15. Matsui, T., Bidiville, A., Maejima, K., Sai, H., Koida, T., Suezaki, T., Matsumoto, M., Saito, K., Yoshida, I. & Kondo, M. High-efficiency amorphous silicon solar cells: Impact of deposition rate on metastability. *Appl. Phys. Lett.* **106**, (2015).

16. Fraunhofer Institute for Solar Energy Systems. Photovoltaics Report. Available at: https://www.ise.fraunhofer.de/content/dam/ise/de/documents/publications/studies/Photovoltaics-Report.pdf.

17. Mori, S., Oh-oka, H., Nakao, H., Gotanda, T., Nakano, Y., Jung, H., Iida, A., Hayase, R., Shida, N., Saito, M., Todori, K., Asakura, T., Matsui, A. & Hosoya, M. Organic photovoltaic module development with inverted device structure. *MRS Proc.* **1737**, mrsf14-1737-u17-02 (2015).

18. Yang, W. S., Noh, J. H., Jeon, N. J., Kim, Y. C., Ryu, S., Seo, J. & Seok, S. I. High-Performance Photovoltaic Perovskite Layers Fabricated through Intramolecular Exchange. *Science (80-.).* **348**, 1234–1237 (2015).

19. Snaith, H. J. Perovskites: The emergence of a new era for low-cost, high-efficiency solar cells. *J. Phys. Chem. Lett.* **4**, 3623–3630 (2013).

20. Saliba, M., Matsui, T., Seo, J. Y., Domanski, K., Correa-Baena, J. P., Nazeeruddin, M. K., Zakeeruddin, S. M., Tress, W., Abate, A., Hagfeldt, A. & Grätzel, M. Cesium-containing triple cation perovskite solar cells: Improved stability, reproducibility and high efficiency. *Energy Environ. Sci.* **9**, 1989–1997 (2016).

21. NREL. Reference Air Mass 1.5 Spectra. Available at: https://www.nrel.gov/grid/solar-resource/spectra-am1.5.html.

22. Shockley, W. & Queisser, H. J. Detailed balance limit of efficiency of p-n junction solar cells. *J. Appl. Phys.* **32**, 510–519 (1961).

23. Rühle, S. Tabulated values of the Shockley – Queisser limit for single junction solar cells. **130**, 139–147 (2016).

24. U.S. Geological Survey. Mineral commodity summaries 2018. 200 (2018). doi:10.3133/70194932

25. Siebentritt, S. & Schorr, S. Kesterites - a challenging material for solar cells. *Prog. Photovoltaics Res. Appl.* **20**, 512–519 (2012).

26. Wang, W., Winkler, M. T., Gunawan, O., Gokmen, T., Todorov, T. K., Zhu, Y. & Mitzi, D. B. Device Characteristics of CZTSSe Thin-Film Solar Cells with 12.6% Efficiency. *Adv. Energy Mater.* **4**, 1301465 (2014).

27. Ennaoui, A., Fiechter, S., Pettenkofer, C., Alonso-Vante, N., Büker, K., Bronold, M., Höpfner, C. & Tributsch, H. Iron disulfide for solar energy conversion. *Sol. Energy Mater. Sol. Cells* **29**, 289–370 (1993).

28. Steinhagen, C., Harvey, T. B., Stolle, C. J., Harris, J. & Korgel, B. A. Pyrite nanocrystal solar cells: Promising, or fool's gold? *J. Phys. Chem. Lett.* **3**, 2352–2356 (2012).

29. Sinsermsuksakul, P., Hartman, K., Bok Kim, S., Heo, J., Sun, L., Hejin Park, H., Chakraborty, R., Buonassisi, T. & Gordon, R. G. Enhancing the efficiency of SnS solar cells via band-offset engineering with a zinc oxysulfide buffer layer. *Appl. Phys. Lett.* **102**, (2013).

30. Sinsermsuksakul, P., Sun, L., Lee, S. W., Park, H. H., Kim, S. B., Yang, C. & Gordon, R. G. Overcoming Efficiency Limitations of SnS-Based Solar Cells. *Adv. Energy Mater.* **4**, 1–7 (2014).

31. Steinmann, V., Jaramillo, R., Hartman, K., Chakraborty, R., Brandt, R. E., Poindexter, J. R., Lee, Y. S., Sun, L., Polizzotti, A., Park, H. H., Gordon, R. G. & Buonassisi, T. 3.88% Efficient Tin Sulfide Solar Cells Using Congruent Thermal Evaporation. *Adv. Mater.* **26**, 7488–7492 (2014).

2. Solar cell and junction concepts

2.1 The p-n junction

Photovoltaic devices rely on the junction between n-type and p-type semiconductors. When in contact a “depletion region” forms at the p-n junction where charge carriers from each side diffuse across the junction. This charge migration leaves behind a negatively charged area in the p-type semiconductor and a positively charged area in the n-type semiconductor (see Figure 2.1). This depletion region therefore effectively has no free charge carriers and the charged regions act as a potential barrier, impeding the flow of electrons and holes. The depletion width and hence the energetic barrier is lessened in forward bias (i.e. a positive voltage applied to the p-type side of the junction) allowing current to flow.

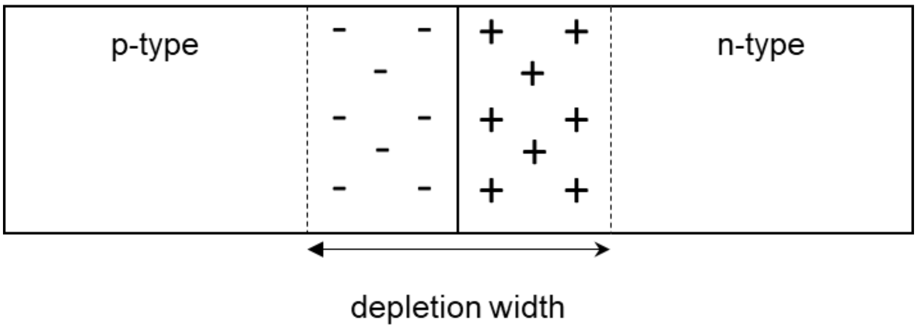

Figure 2.1: Diagram of a p-n junction.

If both the p- and n-types are made from the same material (with each side doped with acceptors and donors respectively) a homojunction is formed like the case shown in Figure 2.2. Since both sides of the junction have identical band gaps, the band structure across the junction is smooth and absorption takes place in both p- and n-type regions[1]. This is the case for c-Si devices.

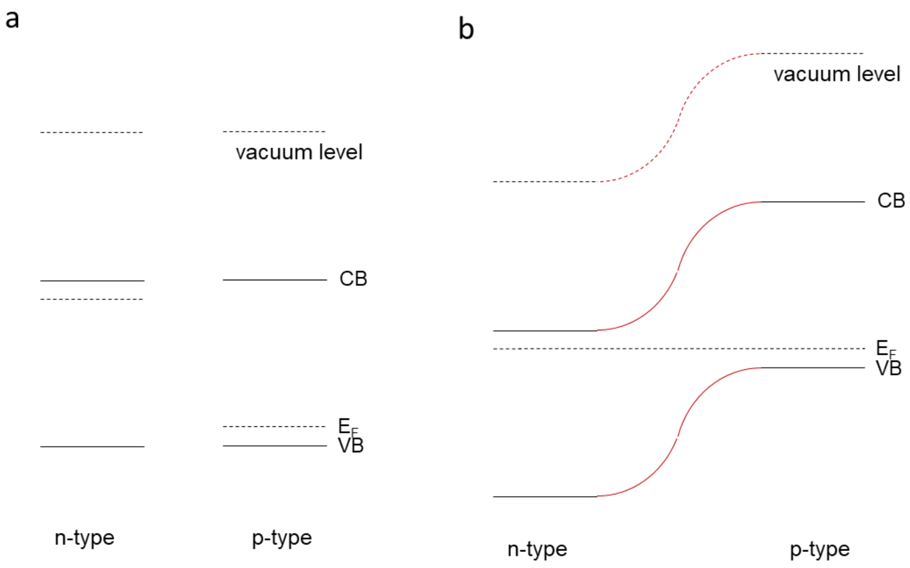

Figure 2.2: Diagram of the energy levels in a homojunction a) before and b) after junction formation.

If different materials are used for each side of the junction, a heterojunction is formed. Absorption typically occurs in the p-type material and the n-type partner layer is therefore chosen to have a larger band gap to allow transmission of light. These layers are referred to as absorber and window layers respectively. As a result of the difference in band gaps between the two semiconductors there are discontinuities in the band structure at the interface.

Figure 2.3 shows the band structure of example heterostructures before and after junction formation. The difference in the proximity of the conduction band to the vacuum level between the p- and n-type semiconductors (illustrated in green) is defined as the conduction band offset. By convention the conduction band offset is taken to be positive where the conduction band of the n-type is higher than that of the p-type material and negative in the reverse scenario. The conduction band offsets govern the type of discontinuity in the conduction band after junction formation. A negative conduction bad offset results in a “cliff-like” feature and a positive offset results in a “spike-like” feature, illustrated in Figure 2.3a and 2.3b respectively. Minemoto *et al.* report that a spike-like feature results in impeded charge transport and hence a reduced current in the device whereas the cliff-like case reduces the voltage produced[2].

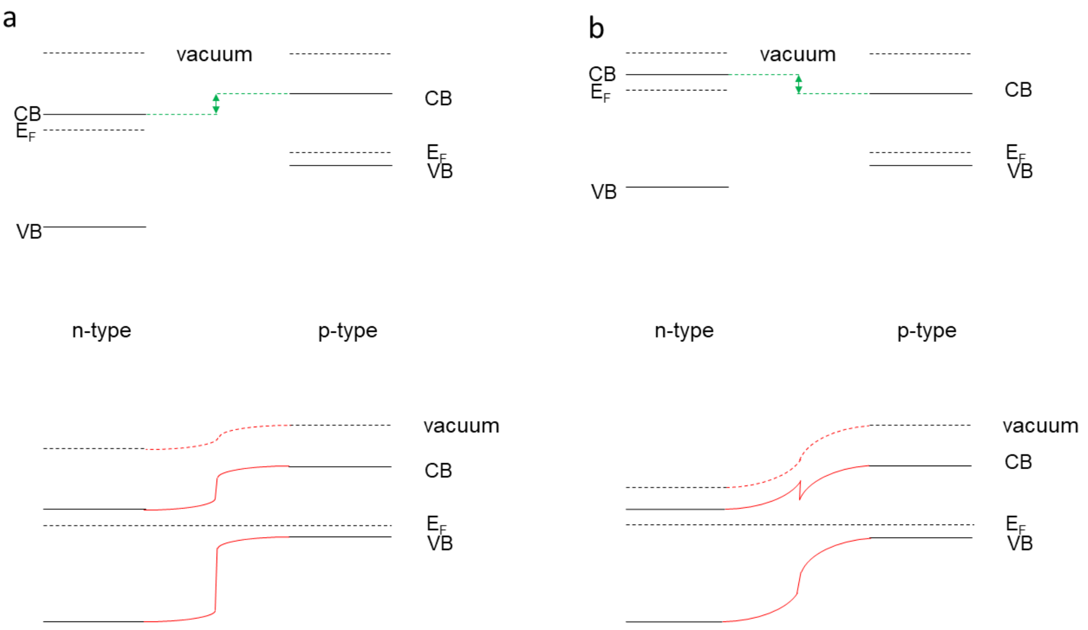

Figure 2.3: The energy levels before and after a heterojunction is between two materials with a) a negative conduction band offset and b) a positive conduction band offset. The offsets are denoted in green.

Absorption of a photon with energy greater than the band gap of the semiconductor generates an electron-hole pair and then, for the pair to be separated and the charge to be extracted, carriers must be swept apart by the field.

Figure 2.4 shows the energy levels in a p-n junction. A photon with energy hv is absorbed in the p-type semiconductor, electrons in the semiconductors seek to reduce their energy by moving from the p- to the n-side of the junction. In the case of the holes this behaviour manifests as movement from the n- to the p-type side of the junction in much the same way as an air bubble rises in water.

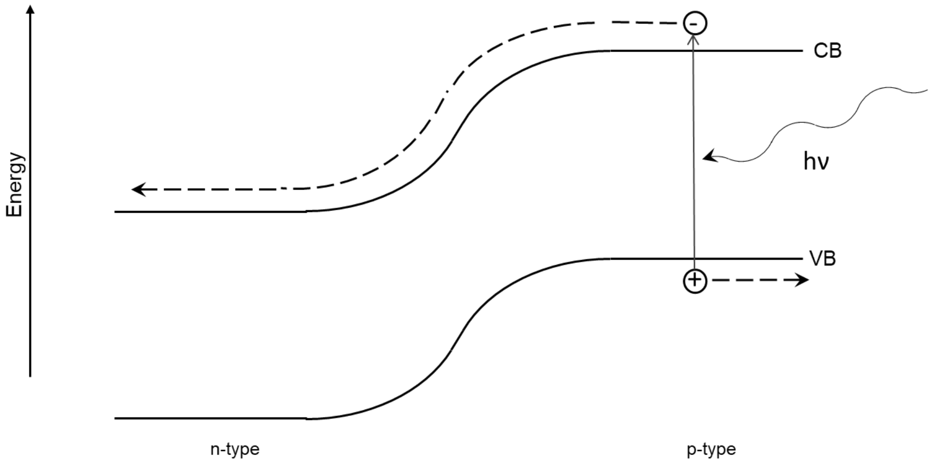

Figure 2.4: Generation and separation of an electron-hole pair in a p-n junction.

2.2 The Shockley equation

The basic function of a solar photovoltaic cell comes from the operation of the p-n junction. This junction, in the ideal case, can be modelled as a diode and can be described using the Shockley diode equation:

$$J(V) = J_0\left(\exp\left(\frac{qV}{nkT}\right)-1\right) \qquad \text{Equation 2.1}$$

where J is current density, J_0 is reverse saturation current density, q is the electronic charge, V is the applied voltage, n is the ideality factor, k is the Boltzmann constant and T is the temperature. The ideality factor describes the extent to which the device behaves like an ideal diode, its value is increased by recombination, typical recombination routes are trap-assisted (Shockley-Read-Hall) and tunnelling currents.

When a light source is added a photocurrent term, J_L, is added:

$$J(V) = J_0\left(\exp\left(\frac{qV}{nkT}\right) - 1\right) - J_L \qquad \text{Equation 2.2}$$

and the equivalent circuit is shown in Figure 2.5.[3]

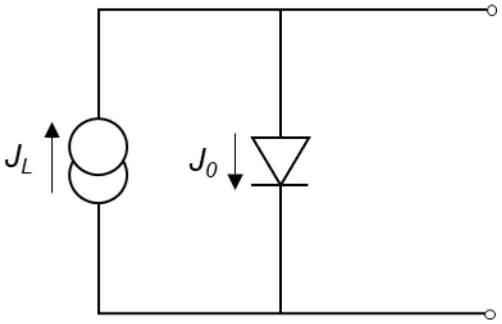

Figure 2.5: Equivalent circuit of an ideal solar cell.

In order to properly describe the system, parasitic resistances must be taken account of. The resistance of the contacts and layers can be represented as a single series resistance, R_s, and the leakage currents, typically arising due to pinholes or at grain boundaries, can be described as the shunt resistance, R_{sh}. These two additions alter the equivalent circuit from the one shown in Figure 2.5 to that shown in Figure 2.6. The Shockley diode equation with these resistances included is shown in Equation 2.3.

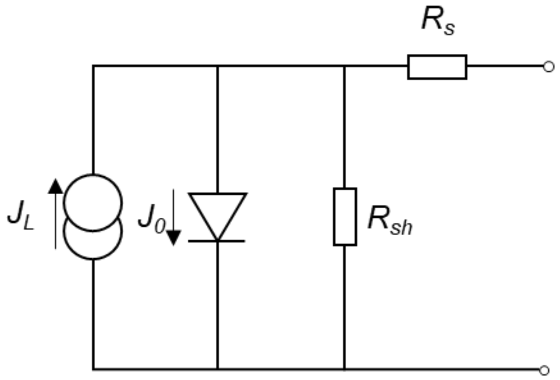

Figure 2.6: Equivalent circuit of a solar cell with parasitic resistances.

$$J(V)=J_0\left(\exp\left(\frac{q(V-JR_s)}{nkT}\right)-1\right)-\frac{V-JR_s}{R_{sh}}-J_L \qquad \text{Equation 2.3}$$

2.3 Current-voltage behaviour

A large number of the important parameters of a solar PV device can be extracted from a current-voltage trace. The simplest parameters to extract are the open circuit voltage (V_{oc}) and short circuit current density (J_{sc}). The V_{oc} is defined as the voltage across the contacts when they are isolated that is to say:

$$J(V_{oc})=0 \qquad \text{Equation 2.4}$$

The J_{sc} is the current density present when the two terminals of the solar cell are connected to no external load but can practically be approximated to be the photocurrent:

$$J(0)=J_{sc}\approx J_L \qquad \text{Equation 2.5}$$

The fill factor (*FF*) is a measure of how square the *J*-*V* curve is (see Figure 2.7) and is calculated from the ratio between the maximum power density achieved by the cell and the power density value obtained from the product of V_{oc} and J_{sc}.

$$FF=\frac{V_{max}\cdot J_{max}}{V_{oc}\cdot J_{sc}} \qquad \text{Equation 2.6}$$

The power conversion efficiency (*PCE*), η, of the device is the ratio of the power density output by the solar cell at its maximum power point to the power density of the incident light. By convention for terrestrial PV this is undertaken with an AM1.5 spectrum having an intensity of 100 mW·cm^{-2}.

$$\eta=\frac{V_{max}\cdot J_{max}}{100\ \text{mW}\cdot\text{cm}^{-2}}=\frac{V_{oc}\cdot J_{sc}\cdot FF}{100\ \text{mW}\cdot\text{cm}^{-2}} \qquad \text{Equation 2.7}$$

The series and shunt resistances can be approximated as the inverse of the gradients at the points where the *J*-*V* curve crosses the voltage and current density axes respectively.

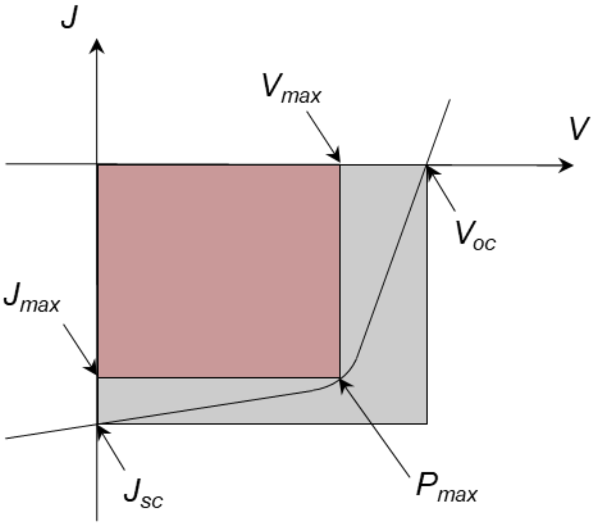

Figure 2.7: Light J-V curve showing the location of each of the solar cell working parameters. The fill factor is the ratio of the areas of the red and grey boxes.

2.4 Power losses in photovoltaic cells

2.4.1 Fundamental losses

As discussed in Section 1.2.6 a solar cell's ability to generate energy is limited by the trade-off between the current and voltage. Transmission losses occur when the incident photon has insufficient energy to excite an electron from the valence band to the conduction band, limiting the current. Conversely, photons having energy greater than the band gap have their excess energy lost to thermalisation of the carrier, limiting the voltage.

2.4.2 Recombination losses

Recombination, where the electron-hole pairs generated by the absorption of photons annihilate, acts to reduce both current and voltage. Trap states, caused by defects and impurities in the cell, aid the process of recombination by providing a route for the electron to drop back to the valence band. For thin film PV devices the most significant recombination mechanism is the two-stage Shockley-Read-Hall mechanism in which an unoccupied trap state first captures a hole from the valence band and then an electron from the conduction band[4].

2.4.3 Series and shunt resistances

Non-ideal series resistance (i.e. $R_s > 0$) originates from poor electrical contacts and resistive layers in the device which act to impede charge flow. Non-ideal shunt resistances ($R_{sh} < \infty$) originate from current leakage through the device. Both the series and shunt resistance work to reduce the performance of the cell by the reduction of the fill factor. High series resistances result in a shallower gradient in the forward bias region, whereas Low shunt resistances cause an increase in the gradient in the reverse bias region as shown in Figure 2.8.

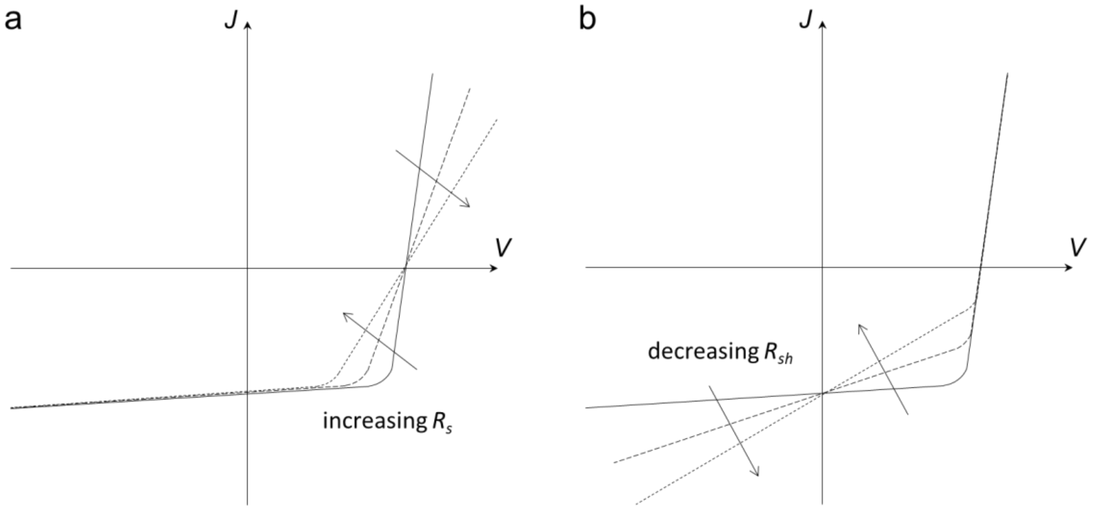

Figure 2.8: The effects of a) increasing series resistance and b) decreasing shunt resistance on the *J-V* response of a photovoltaic cell.

2.4.5 Other losses

Other forms of loss in the device include reflection losses, decreasing the number of available photons for absorption. These reflection losses can be mitigated somewhat by the addition of an antireflective coating of the front surface of the device.

Additionally, absorption in layers besides the absorber layer typically do not contribute to the power output of the cell. This is especially concerning for those semiconductor absorbers which use CdS as a partner layer; absorption in CdS does not contribute to the photocurrent, leading to a characteristic shoulder in the external quantum efficiency (EQE) curve (shown in Figure 2.8).

If the position of the junction is too far from the charge carrier generation, a buried junction is formed, severely limiting the extraction of charge carriers. A typical buried junction response is shown by the red trace in Figure 2.9.

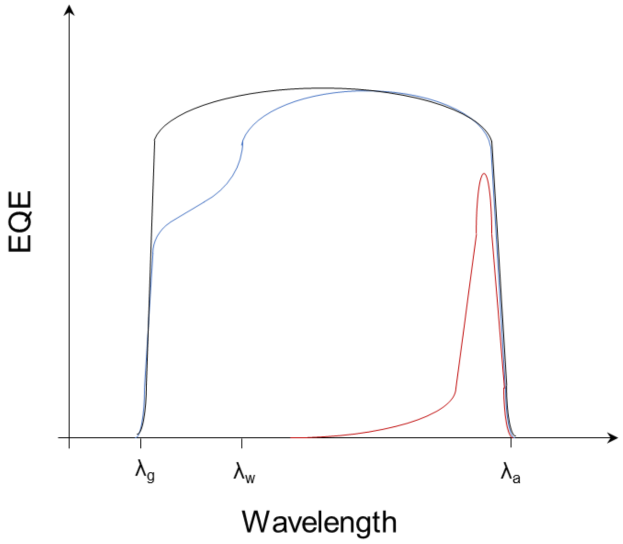

Figure 2.9: Example EQE responses from a device whose absorber and window layer materials have band gaps corresponding to wavelengths of λ_a and λ_w respectively and where λ_g is the wavelength corresponding to the band gap of the transparent conducting oxide. The black trace shows an ideal EQE response, the blue trace shows one with some parasitic absorption from the window layer, and the red trace shows a cell with a buried junction.

2.5 Photovoltaic device design

Devices can either be made in substrate or superstrate geometry, both illustrated in Figure 2.10. In the superstrate configuration light enters through the substrate (i.e. from the bottom of the diagram) whereas the substrate in the substrate configuration is structural only. In this work both geometries are employed, the substrate configuration for the Cu_3BiS_3 devices and the superstrate for the Sb_2Se_3.

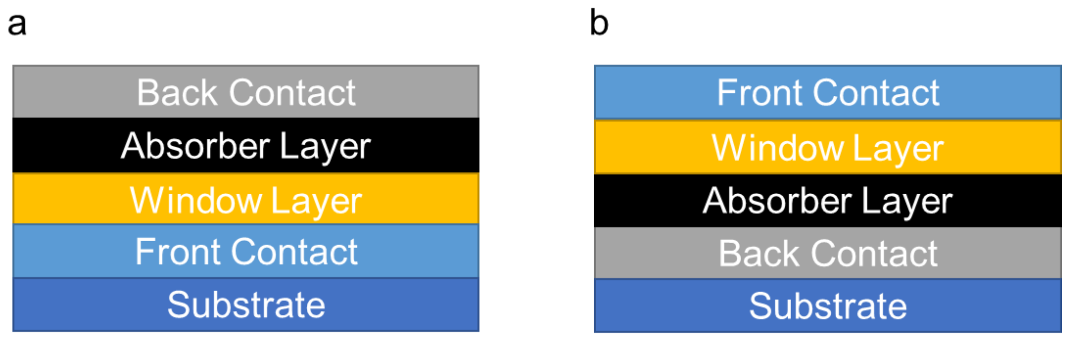

Figure 2.10: Schematic diagrams of a) superstrate device configuration and b) substrate device configuration.

Table 2.1 lists the primary considerations for the selection of materials for each layer. The absence of p-type TCOs necessitates the use of n-type window layers and hence p-type absorber layers. Beyond these, the energy levels ought to be considered. In a semiconductor heterojunction the conduction band offset is determined by the relative positions (i.e. distance from the vacuum level) of the conduction bands of each material, a positive conduction band offset occurs when the conduction band in the n-type material is higher than that of the p-type. These band offsets manifest as the cliff- and spike-like features described in Section 2.1 and shown in Figure 2.3.

Table 2.1: Criteria for selection of layers in the photovoltaic device.

Layer	**Materials Investigated**	**Considerations**
Substrate	Glass	Transparent (for superstrate only)
Front contact	FTO, ITO	Transparent, conducting
Window layer	CdS, ZnS, TiO_2	Wide band gap (e.g. > 2.4 eV), n-type
Absorber layer	Cu_3BiS_3, Sb_2Se_3	Suitable band gap (e.g. ~ 1.4 eV), p-type
Back contact	Au	Conducting

References for Chapter 2

1. Markvart, T. *Solar Electricity*. (John Wiley & Sons, 2000).

2. Minemoto, T., Matsui, T., Takakura, H., Hamakawa, Y., Negami, T., Hashimoto, Y., Uenoyama, T. & Kitagawa, M. Theoretical analysis of the effect of conduction band offset of window/CIS layers on performance of CIS solar cells using device simulation. *Sol. Energy Mater. Sol. Cells* **67**, 83–88 (2001).

3. Sze, S. M. *Physics of semiconductor devices*. (Wiley-Interscience, 1936).

4. Nelson, J. *The Physics of Solar Cells*. (Imperial College Press, 2003).

3. Literature on Cu_3BiS_3 and Sb_2Se_3

The two solar PV absorber materials to be discussed in this work are Cu_3BiS_3 and Sb_2Se_3. A short review of the state of the literature, particularly concerning their use as photovoltaic absorber materials follows.

3.1 Cu_3BiS_3

As a naturally occurring mineral, Cu_3BiS_3 was first discovered in 1805 by Selb[1] in the Wittichen mine, hence its mineral name wittichenite. Initially synthesised artificially for mineralogical research purposes in 1947 by Nuffield[2], Cu_3BiS_3 was noted to have material properties suitable for photovoltaic applications in 1997 by Nair[3]. These properties, combined with its lower reliance on elements with low Earth-abundance have gained the compound attention in the photovoltaics research community. Often the exploration of new potential absorber materials, such as $CuSbS_2$ and CZTS is justified in terms of seeking to replace expensive elements in pre-existing technologies with similar, more abundant elements (i.e. In and Se from $CuInSe_2$ with Sb and S; and In and Ga from CIGS with Zn and Sn). Nair, however, recognised Cu_3BiS_3 as a solar absorber worthy of investigation in its own right. Furthermore, if only replacement of problem elements were the goal, the $CuBiS_2$ phase would be selected here rather than Cu_3BiS_3. Indeed, the Spectral Limited Maximum Efficiency (SLME) calculations performed by Yu have the $CuBiS_2$ phase outperforming the Cu_3BiS_3 phase with values of ~21.0% and ~18.5% respectively[4]. In this work the Cu_3BiS_3 phase is considered due to its lower reliance on Bi, the least abundant of the three elements and the possibility to demonstrate PV devices from it.

While materials like CIGS and CZTS have regular tertragonal crystal structure (chalcopyrite[5,6] and kesterite or stannite[7,8] respectively), Cu_3BiS_3 has an orthorhombic crystal structure (belonging to space group $P2_12_12_12_1$) with low symmetry. As shown in Figure 3.1 the unit cell (a = 7.723 Å, b = 10.395 Å, c = 6.716 Å) comprises copper atoms in nearly trigonal planar coordination with the sulfur atoms – the Cu-S bond lengths and S-Cu-S angles varying only slightly[9] – and the Bi atoms in each cell can either be described as having a trigonal pyramidal arrangement with the nearest three sulfur atoms[9] or a distorted square pyramidal arrangement with the nearest five[10].

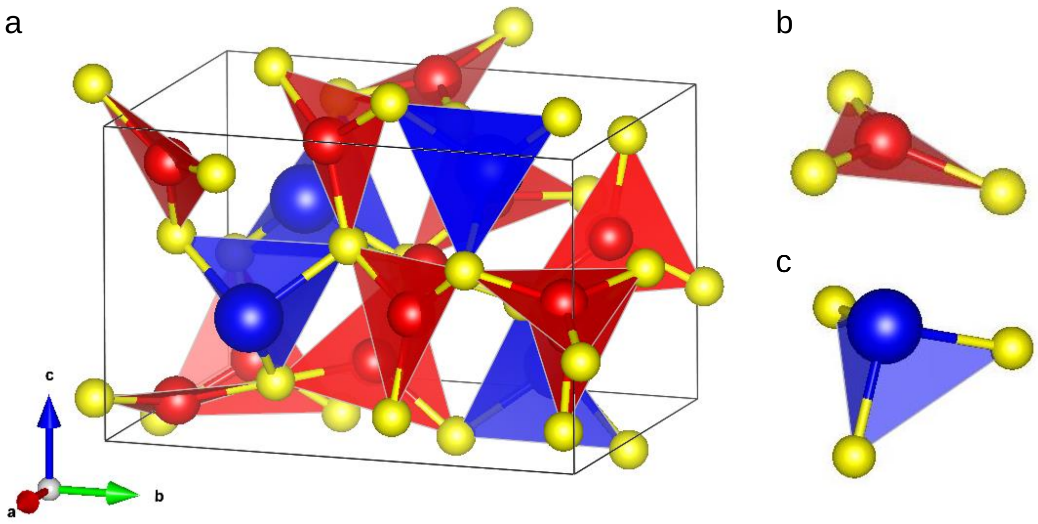

Figure 3.1: The crystal structure of Cu_3BiS_3. a) the unit cell of wittichenite b) a CuS_3 structural unit c) the BiS_3 structural unit. Here the Cu atoms are represented in red, the Bi in blue and the S in yellow. These structures were produced using the VESTA software[11].

Figure 3.2 shows the ternary phase diagrams for the Cu-Bi-S system at 200 and 300°C. The Cu_3BiS_3 phase lies on both the Bi-CuS and Bi_2S_3-Cu_2S tie lines. The surrounding phases which must be monitored for when growing phase pure Cu_3BiS_3 are Bi, Cu_xS, $CuBiS_2$ and $Cu_4Bi_4S_9$. Indeed, the Cu_3BiS_3 ternary has been shown by Wang to react with S_2 to form the sulfur-rich $Cu_4Bi_4S_9$ phase at temperatures as low as 138°C[12].

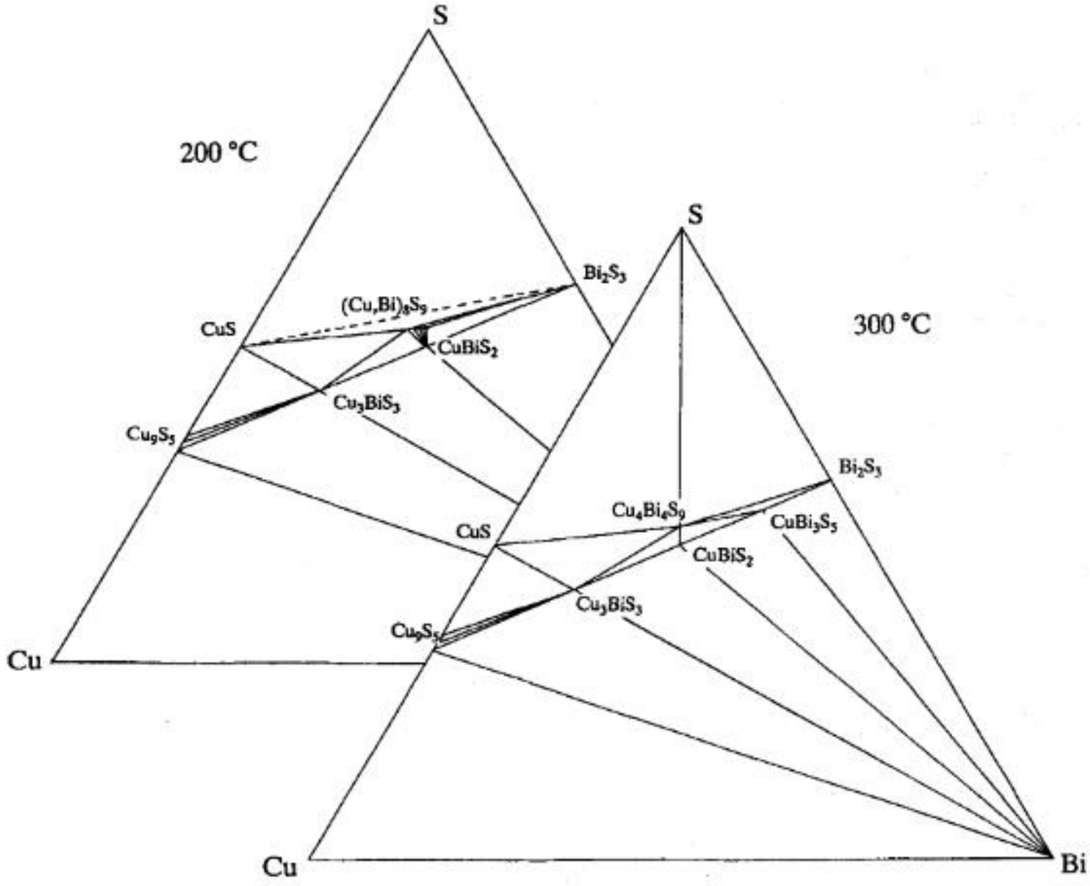

Figure 3.2: Ternary phase diagrams of the Cu-Bi-S system at 200 and 300°C, figure from Wang, 1994[12].

Growth techniques for the Cu_3BiS_3 phase can be inferred from the ternary phase diagram (Figure 3.2). Considering the tie line which the Cu_3BiS_3 phase lies on leads to the combination of the Cu_2S and Bi_2S_3 in a 3:1 molecular ratio as the simplest method of production of the compound. Growth of the phase from elemental sources is also considered and may be performed by either a one-step process (e.g. co-evaporation of Cu, Bi and S in a 3:1:3 atomic ratio) or two-step such as the sulfurisation of metallic precursor stacks (e.g. evaporated Cu/Bi bilayers).

Thin films of Cu_3BiS_3 have been grown by reactive co-sputtering[13], sulfurisation of a metal stack[14,15], evaporation of Cu and Bi in the presence of elemental sulfur[16], annealing of binary sulfides[3,17] and electrochemical deposition. The synthesis of colloidal Cu_3BiS_3 nanoparticles has also been demonstrated[18], enabling the possibility of the creation of films using nanoparticle inks. In this work the growth of Cu_3BiS_3 had been pursued by means of sulfurisation.

Using H_2S as the sulfurizing gas has been reported to produce good film morphology from metallic Cu-Bi stacks on silica – adhesion was poor on soda-lime glass – but films produced from the sulfurisation of metal sulfides buckled due to thermal expansion, furthermore the annealing of these Cu_3BiS_3 films in H_2S increases grain size and reduces resistivity of films[19]. When grown by the sulfurisation of Bi-Cu precursor layers using elemental sulfur there was no compositional variation shown in the sample parallel to the substrate[14]. These films showed poor electrochemical properties in aqueous $Eu(NO_3)_3$ and though some improvement was observed after short a KCN etch, longer etching times (greater than 60 seconds) completely supressed all photoactivity.

Simulations using DFT arrive at a band gap of 1.5-1.7 eV with a high absorption coefficient of greater than 10^5 cm^{-1} [20], these being greater than the optically determined values of E_g = 1.2-1.4 eV (direct transition) and $\alpha > 10^4$ cm^{-1} respectively[13,16,17]. Photoreflectance studies have demonstrated the dependence of this band gap on temperature[21]. The material has been demonstrated as p-type by multiple different research groups[14,17,22]. The overwhelming majority of literature on this material citing photovoltaic applications concerns itself with the growth and characterisation of the material.

Despite the propensity towards Cu_3BiS_3 journal articles' citing of photovoltaic applications as motivation for pursuing its investigation, there are very few examples of reports of devices. Mesa *et al.* have reported full device structures of Al/Cu_3BiS_3/window/ZnO where the buffer layers used were In_2S_3 and ZnS[23]. These device structures were investigated by TEM and XRD only, no mention was given regarding their performance as photovoltaic devices. Hernádez-Mota *et al.* report a similarly configured device (Al/Cu_3BiS_3/CdS/i-ZnO/ITO) for which they do present current-voltage response, however the performance is poor: $\eta = 0.09\%$, $J_{sc} = 2.9\ \mathrm{mA{\cdot}cm^2}$, $V_{oc} = 97\ \mathrm{mV}$, $FF = 31.3\%$[24]. Yin also reports devices using Cu_3BiS_3 with an efficiency of 1.28%[25], despite being the highest efficiency reported to date for Cu_3BiS_3 devices, this dye structure is not the planar heterojunction more conventionally used in photovoltaics but is instead a dye-sensitised type device and does not show any sign of being more effective than standard dyes.

3.2 Sb_2Se_3

Sb_2Se_3 has a peculiar ribbon-like structure shared by only a few other compounds including Sb_2S_3, Bi_2S_3 and Bi_2Se_3 [26]. This structure is orthorhombic and can either be classified as Pbmn[27,28] or Pnma[29,30] depending on how the axes of the unit cell are labelled. The unit cell has dimensions $a = 11.6200$ Å, $b = 11.7700$ Å, $c = 3.9620$ Å as defined in the Pbnm classification or $a = 11.7700$ Å, $b = 3.9620$ Å, $c = 11.6200$ Å for the Pnma. While both space groups are functionally identical and see use in the literature here the Pbmn is used in this work since it is more common in contemporary reports.

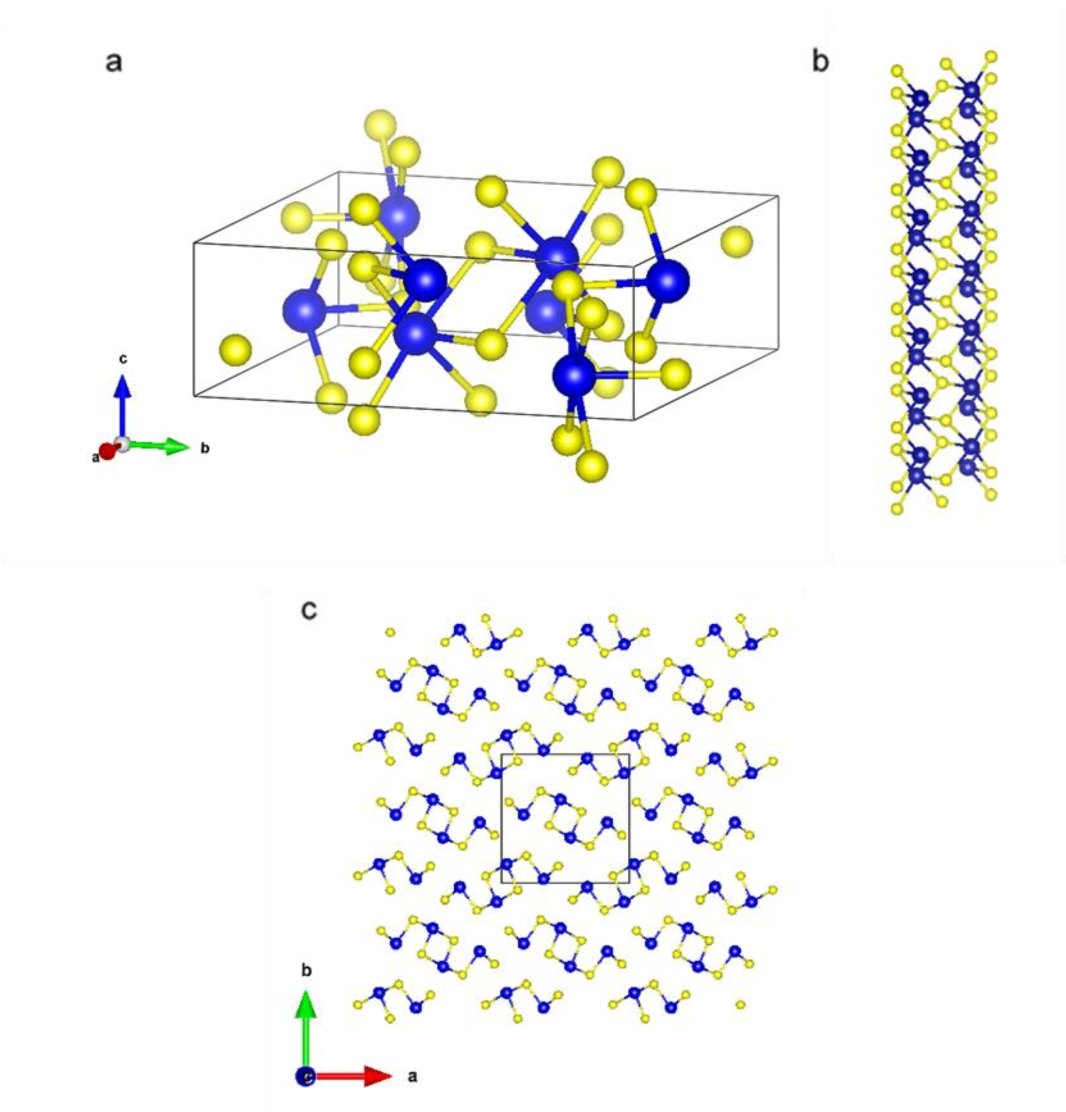

Figure 3.3: The crystal structure of Sb_2Se_3 a) the unit cell of Sb_2Se_3 b) a single chain of Sb_2Se_3 c) view down the covalently bonded c-axis. Here the Sb atoms are represented in blue and the Se in yellow. Recreated using the VESTA software[11].

Figure 3.3 shows the crystal structure of Sb_2Se_3, the unit cell comprises Sb_4Se_6 bonded covalently together in the c-direction to form 1-dimensional ribbons which are van der Waals bonded to adjacent ribbons in the a- and b-directions. This material is attractive from a structure point of view for thin film photovoltaic devices since if grain boundaries are parallel to the ribbons there will be no dangling bonds at the boundary and it will be electrically benign, eliminating a major pathway to recombination losses in devices. Furthermore, being a binary compound having no other stoichiometries (see Figure 3.4), phase control in the system is trivial.

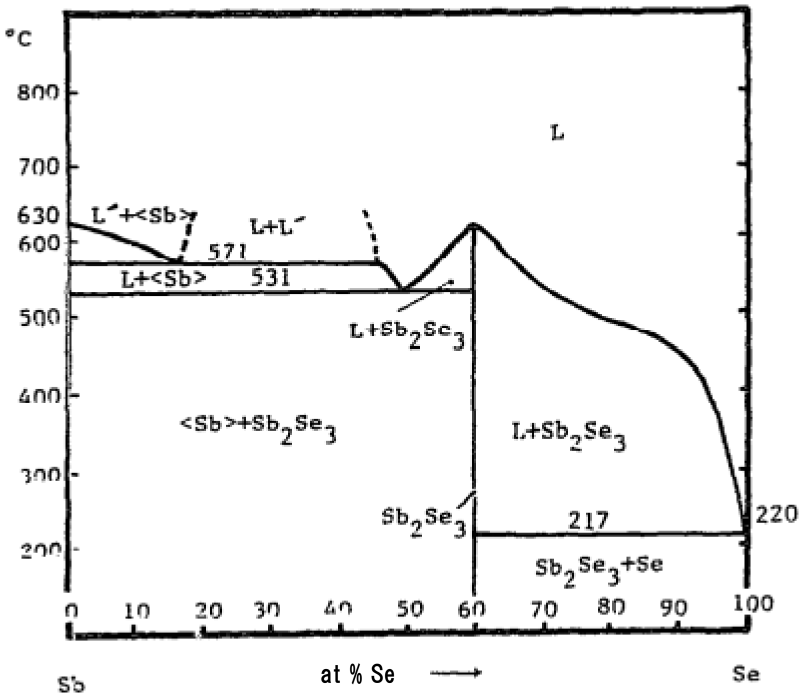

Figure 3.4: The binary phase diagram for Sb and Se showing Sb_2Se_3 as the only binary phase. Reproduced from from Bordas *et al.* [31].

The band gap of Sb_2Se_3 has been measured optically, being reported as having an indirect band gap of 1.0-1.5 eV [32–35] and a direct band gap of 1.2-1.9 eV [32,34]. The discrepancy in these findings is likely to be due to the difficulty of execution of the Tauc method and the crystallinity of the films. Films deposited at low temperatures are often amorphous with the amorphous phase having a wider band gap than the crystalline material [36–38]. Annealing steps have been shown to transform the films from amorphous to polycrystalline, reducing the band gap [36]. Despite its indirect fundamental band gap – and perhaps owing to its only ~0.15 eV wider direct band gap[32] – Sb_2Se_3 also has strong optical absorption, approaching 10^5 cm^{-1}, for above band gap energies[39].

Thin films have been observed to be p-type[39–41] due to Se_{Sb} defects[42] with doping densities of 1.49×10^{15} cm^{-3} being reported in untreated devices[43]. The electron and hole mobilities are 15 and 42 $cm^2\cdot V^{-1}\cdot s^{-1}$ respectively[44]. The conductivity of the material has been reported to be anisotropic: parallel to the ribbon direction conductivity at room temperature was measured to be 9×10^{-8} $\Omega^{-1}\cdot cm^{-1}$, 2.2 times greater than the perpendicular value of 4×10^{-8} $\Omega^{-1}\cdot cm^{-1}$ [37].

The material has been grown by CBD[36], CVD[45], the SILAR method[46], solution processing[47], sputtering[41] and thermal evaporation[43,48,49]. The most successful devices have come from specialised forms of PVD: CSS[50–52], rapid thermal evaporation (RTE)[53–56] and vapour transport deposition (VTD)[57]. Notably, Benjamin reports some degree of controllable orientations in Sb_2Te_3 grown by LPCVD on fused SiO_2 substrates however the data presented for Sb_2Se_3 are not sufficient to understand if this material behaves similarly[45].

Devices typically have the structure glass/TCO/n-type window/Sb_2Se_3/hole transport layer/metal contact. Typical window layers used are CdS[36,48,55,57], ZnS[41], TiO_2[46,52,58], ZnO[54], and SnO_2[59]. The hole transport layers used in these devices include: P3HT[60], PCDTBT[52], colloidal PbS quantum dots[55] with highest efficiencies of 5.5%, 6.6% and 6.5% reported for each respectively and all improvements over equivalent devices without the HTM. The current record device (η = 7.6%), however, was not reported to use a HTM[57].

In his 2017 review[61] Zakutayev identifies Sb_2Se_3 as a promising candidate for a new, competitive PV absorber material not only due to its structure, but also due to the short time over which its device efficiencies have increased, using percent increase per publication as a metric for measuring potential.

The Tang group, the holders of multiple recent record efficiencies in Sb_2Se_3 devices comment in their 2018 paper[57] that their former RTE deposition technique, which is extremely similar to CSS in its function, is limited by the inability to vary substrate temperatures significantly and hence use their VTD process to increase control over this variable.

References for Chapter 3

1. Hintze, C. A. F. *Handbuch der Mineralogie*. (Cambridge, 1904).

2. Nuffield, E. W. Studies of mineral sulpho-salts: xi-wittichenite (klaprothite). *Econ. Geol.* **42**, 147–160 (1947).

3. Nair, P. K., Huang, L., Nair, M. T. S., Hu, H., Meyers, E. A. & Zingaro, R. A. Formation of p-type Cu_3BiS_3 absorber thin films by annealing chemically deposited Bi_2S_3–CuS thin film. *J. Mater. Res.* **12**, 651–656 (1997).

4. Yu, L., Kokenyesi, R. S., Keszler, D. A. & Zunger, A. Inverse design of high absorption thin-film photovoltaic materials. *Adv. Energy Mater.* **3**, 43–48 (2013).

5. Repins, I., Mansfield, L., Kanevce, A., Jensen, S. A., Kuciauskas, D., Glynn, S., Barnes, T., Metzger, W., Burst, J., Jiang, C. S., Dippo, P., Harvey, S., Teeter, G., Perkins, C., Egaas, B., Zakutayev, A., Alsmeier, J. H., Lusky, T., Korte, L. *et al.* Wild band edges: The role of bandgap grading and band-edge fluctuations in high-efficiency chalcogenide devices. *Conf. Rec. IEEE Photovolt. Spec. Conf.* **16**, 235–239 (2016).

6. Panthani, M. G., Akhavan, V., Goodfellow, B., Schmidtke, J. P., Dodabalapur, A., Barbara, P. F. & Korgel, B. A. Synthesis of $CuInS_2$, $CuInSe_2$, and Cu(InxGa1-x)Se2 (CIGS) Nanocrystal “Inks” for Printable Photovoltaics. *Nano* **130**, 16770–16777 (2008).

7. Siebentritt, S. & Schorr, S. Kesterites - a challenging material for solar cells. *Prog. Photovoltaics Res. Appl.* **20**, 512–519 (2012).

8. Walsh, A., Chen, S., Wei, S. H. & Gong, X. G. Kesterite thin-film solar cells: Advances in materials modelling of Cu_2ZnSnS_4. *Adv. Energy Mater.* **2**, 400–409 (2012).

9. Kocman, V. & Nuffield, E. W. The crystal structure of wittichenite, Cu_3BiS_3. *Acta Crystallogr. Sect. B Struct. Crystallogr. Cryst. Chem.* **29**, 2528–2535 (1973).

10. Kumar, M. & Persson, C. Cu_3BiS_3 as a potential photovoltaic absorber with high optical efficiency. *Appl. Phys. Lett.* **102**, 1–5 (2013).

11. Momma, K. & Izumi, F. VESTA 3 for three-dimensional visualization of crystal, volumetric and morphology data. *J. Appl. Crystallogr.* **44**, 1272–1276 (2011).

12. Wang, N. The Cu-Bi-S System: Results from Low-Temperature Experiments. *Mineral. Mag.* **58**, 201–204 (1994).

13. Gerein, N. J. & Haber, J. A. One-step synthesis and optical and electrical properties of thin film Cu_3BiS_3 for use as a solar absorber in photovoltaic devices. *Chem. Mater.* **18**, 6297–6302 (2006).

14. Colombara, D., Peter, L. M., Hutchings, K., Rogers, K. D., Schäfer, S., Dufton, J. T. R. & Islam, M. S. Formation of Cu_3BiS_3 thin films via sulfurization of Bi–Cu metal precursors. *Thin Solid Films* **520**, 5165–5171 (2012).

15. Gerein, N. J. & Haber, J. A. Synthesis of Cu3BiS_3 Thin Films by Heating Metal and Metal Sulfide Precursor Films under Hydrogen Sulfide. *Chem. Mater.* **18**, 6289–6296 (2006).

16. Mesa, F., Dussan, A. & Gordillo, G. Study of the growth process and optoelectrical properties of nanocrystalline Cu_3BiS_3 thin films. *Phys. Status Solidi* **920**, 917–920 (2010).

17. Estrella, V., Nair, M. T. S. & Nair, P. K. Semiconducting Cu_3BiS_3 thin films formed by the solid-state reaction of CuS and bismuth thin films. *Semicond. Sci. Technol.* **18**, 190–194

(2003).

18. Yan, C., Gu, E., Liu, F., Lai, Y., Li, J. & Liu, Y. Colloidal synthesis and characterizations of wittichenite copper bismuth sulphide nanocrystals. *Nanoscale* **5**, 1789–92 (2013).

19. Gerein, N. J. & Haber, J. A. Synthesis of Cu_3BiS_3 Thin Films by Heating Metal and Metal Sulfide Precursor Films under Hydrogen Sulfide. *Chem. Mater.* **18**, 6289–6296 (2006).

20. Kumar, M. & Persson, C. Cu_3BiS_3 as a potential photovoltaic absorber with high optical efficiency. *Appl. Phys. Lett.* **102**, 1–5 (2013).

21. Yakushev, M. V., Maiello, P., Raadik, T., Shaw, M. J., Edwards, P. R., Krustok, J., Mudryi, A. V., Forbes, I. & Martin, R. W. Investigation of the structural, optical and electrical properties of Cu_3BiS_3 semiconducting thin films. *Energy Procedia* **60**, 166–172 (2014).

22. Mesa, F., Dussan, A. & Gordillo, G. Evidence of trapping levels and photoelectric properties of Cu_3BiS_3 thin films. *Phys. B Condens. Matter* **404**, 5227–5230 (2009).

23. Mesa, F., Dussan, A., Sandino, J. & Lichte, H. Characterization of Al/Cu_3BiS_3/buffer/ZnO solar cells structure by TEM. *J. Nanoparticle Res.* **14**, (2012).

24. Hernádez-Mota, J., Espíndola-Rodríguez, M., Sánchez, Y., López, I., Peña, Y. & Saucedo, E. Thin film photovoltaic devices prepared with Cu_3BiS_3 ternary compound. *Mater. Sci. Semicond. Process.* **87**, 37–43 (2018).

25. Yin, J. & Jia, J. Synthesis of Cu_3BiS_3 nanosheet films on TiO_2 nanorod arrays by a solvothermal route and their photoelectrochemical characteristics. *CrystEngComm* **16**, 2795 (2014).

26. Filip, M. R., Patrick, C. E. & Giustino, F. GW quasiparticle band structures of stibnite, antimonselite, bismuthinite, and guanajuatite. *Phys. Rev. B - Condens. Matter Mater. Phys.* **87**, 205125 (2013).

27. Tideswell, N. W., Kruse, F. H. & McCullough, J. D. The crystal structure of antimony selenide, Sb_2Se_3. *Acta Crystallogr.* **10**, 99–102 (1957).

28. Voutsas, G. P., Papazoglou, A. G., Rentzeperis, P. J. & Siapkas, D. The crystal structure of antimony selenide, Sb_2Se_3. *Zeitschrift fur Krist. - New Cryst. Struct.* **171**, 261–268 (1985).

29. Koc, H., Mamedov, A. M., Deligoz, E. & Ozisik, H. First principles prediction of the elastic, electronic, and optical properties of Sb_2S_3 and Sb_2Se_3 compounds. *Solid State Sci.* **14**, 1211–1220 (2012).

30. Caracas, R. & Gonze, X. First-principles study of the electronic properties of A_2B_3 minerals, with A=Bi,Sb and B=S,Se. *Phys. Chem. Miner.* **32**, 295–300 (2005).

31. Bordas, S. & Clavaguera-Mora, M. T. Phase diagram of the ternary system Ge-Sb-Se. *Thermochim. Acta* **56**, 23–45 (1982).

32. Chen, C., Li, W., Zhou, Y., Chen, C., Luo, M., Liu, X., Zeng, K., Yang, B., Zhang, C., Han, J. & Tang, J. Optical properties of amorphous and polycrystalline Sb_2Se_3 thin films prepared by thermal evaporation. *Appl. Phys. Lett.* (2015). doi:10.1063/1.4927741

33. Mueller, R. & Wood, C. The preparation of amorphous thin films. *J. Non. Cryst. Solids* **7**, 301–308 (1972).

34. El-Shair, H., Ibrahim, A., Abd El-Wahabb, E., Afify, M. & Abd El-Salam, F. Optical properties of Sb_2Se_3 thin films. *Vacuum* **42**, 911–914 (1991).

35. Černošková, E., Todorov, R., Černošek, Z., Holubová, J. & Beneš, L. Thermal properties and the structure of amorphous Sb_2Se_3 thin film. *J. Therm. Anal. Calorim.* **118**, 105–110 (2014).

36. Messina, S., Nair, M. T. S. & Nair, P. K. Antimony Selenide Absorber Thin Films in All-Chemically Deposited Solar Cells. *J. Electrochem. Soc.* **156**, H327 (2009).

37. Kosek, F., Tulka, J. & Štourač, L. Optical, photoelectric and electric properties of single-crystalline Sb_2Se_3. *Czechoslov. J. Phys.* **28**, 325–330 (1978).

38. Arun, P. & Vedeshwar, A. G. Potential of Sb_2Se_3 films for photo-thermal phase change optical storage. *Thin Solid Films* **335**, 270–278 (1998).

39. Chen, C., Bobela, D. C., Yang, Y., Lu, S., Zeng, K., Ge, C., Yang, B., Gao, L., Zhao, Y., Beard, M. C. & Tang, J. Characterization of basic physical properties of Sb_2Se_3 and its relevance for photovoltaics. *Front. Optoelectron.* **10**, 18–30 (2017).

40. Zeng, K., Xue, D. J. & Tang, J. Antimony selenide thin-film solar cells. *Semicond. Sci. Technol.* **31**, 1–13 (2016).

41. Siol, S., Schulz, P., Young, M., Borup, K. A. & Teeter, G. Combinatorial In Situ Photoelectron Spectroscopy Investigation of Sb_2Se_3/ZnS Heterointerfaces. *Adv. Mater. Interfaces* 1600755 (2016). doi:10.1002/admi.201600755

42. Liu, X., Xiao, X., Yang, Y., Xue, D. J., Li, D. B., Chen, C., Lu, S., Gao, L., He, Y., Beard, M. C., Wang, G., Chen, S. & Tang, J. Enhanced Sb_2Se_3 solar cell performance through theory-guided defect control. *Prog. Photovoltaics Res. Appl.* **25**, 861–870 (2017).

43. Li, Z., Zhu, H., Guo, Y., Niu, X., Chen, X., Zhang, C., Zhang, W., Liang, X., Zhou, D., Chen, J. & Mai, Y. Efficiency enhancement of Sb_2Se_3 thin-film solar cells by the co-evaporation of Se and Sb_2Se_3. *Appl. Phys. Express* **9**, (2016).

44. Madelung, O. *Semiconductors: Data Handbook*. (2004).

45. Benjamin, S. L., Groot, C. H. De, Hector, A. L., Huang, R., Koukharenko, E., Levason, W. & Reid, G. Chemical vapour deposition of antimony chalcogenides with positional and orientational control: precursor design and substrate selectivity. *J. Mater. Chem. C Mater. Opt. Electron. devices* **3**, 423–430 (2014).

46. Guijarro, N., Lutz, T., Lana-Villarreal, T., O'Mahony, F., Gomez, R. & Haque, S. A. Toward Antimony Selenide Sensitized Solar Cells: Efficient Charge Photogeneration at spiro-OMeTAD/Sb_2Se_3/Metal Oxide Heterojunctions. *J. Phys. Chem. Lett.* **3**, 1351–1356 (2012).

47. Zhou, Y., Leng, M., Xia, Z., Zhong, J., Song, H., Liu, X., Yang, B., Zhang, J., Chen, J., Zhou, K., Han, J., Cheng, Y. & Tang, J. Solution-processed antimony selenide heterojunction solar cells. *Adv. Energy Mater.* **4**, 1301846 (2014).

48. Liu, X., Chen, J., Luo, M., Leng, M., Xia, Z., Zhou, Y., Qin, S., Xue, D., Lv, L., Huang, H., Niu, D. & Tang, J. Thermal Evaporation and Characterization of Sb_2Se_3 Thin Film for Substrate Sb_2Se_3/CdS Solar Cells. *Appl. Mater. Interfaces* **6**, 10687–10695 (2014).

49. Luo, M., Leng, M., Liu, X., Chen, J., Chen, C., Qin, S. & Tang, J. Thermal evaporation and characterization of superstrate CdS/Sb2Se3 solar cells. *Appl. Phys. Lett.* **104**, 173904 (2014).

50. Li, G., Li, Z., Chen, J., Chen, X., Qiao, S., Wang, S., Xu, Y. & Mai, Y. Self-powered, high-speed Se_2Se_3/Si heterojunction photodetector with close spaced sublimation processed

Se_2Se_3 layer. *J. Alloys Compd.* **737**, 67–73 (2018).

51. Birkett, M., Linhart, W. M., Stoner, J., Phillips, L. J., Durose, K., Alaria, J., Major, J. D., Kudrawiec, R. & Veal, T. D. Band gap temperature-dependence of close-space sublimation grown Sb_2Se_3 by photo-reflectance. *APL Mater.* **6**, (2018).

52. Hutter, O. S., Phillips, L. J., Durose, K. & Major, J. D. 6.6% Efficient Antimony Selenide Solar Cells Using Grain Structure Control and an Organic Contact Layer. *Sol. Energy Mater. Sol. Cells* **188**, 177–181 (2018).

53. Zhou, Y., Wang, L., Chen, S., Qin, S., Liu, X., Chen, J., Xue, D. J., Luo, M., Cao, Y., Cheng, Y., Sargent, E. H. & Tang, J. Thin-film Sb_2Se_3 photovoltaics with oriented one-dimensional ribbons and benign grain boundaries. *Nat. Photonics* **9**, 409–415 (2015).

54. Wang, L., Li, D., Li, K., Chen, C., Deng, H., Gao, L. & Zhao, Y. Stable 6%-effcient Sb_2Se_3 solar cells with a ZnO buffer layer. *Nat. Energy* **2**, 17046 (2017).

55. Chen, C., Wang, L., Gao, L., Nam, D., Li, D., Li, K., Zhao, Y., Ge, C., Cheong, H., Liu, H., Song, H. & Tang, J. 6.5% Certified Efficiency Sb_2Se_3 Solar Cells Using PbS Colloidal Quantum Dot Film as Hole-Transporting Layer. *ACS Energy Lett.* **2**, 2125–2132 (2017).

56. Chen, C., Li, K., Chen, S., Wang, L., Lu, S., Liu, Y., Li, D., Song, H. & Tang, J. Efficiency Improvement of Sb_2Se_3 Solar Cells via Grain Boundary Inversion. *ACS Energy Lett.* **3**, 2335–2341 (2018).

57. Wen, X., Chen, C., Lu, S., Li, K., Kondrotas, R., Zhao, Y., Chen, W., Gao, L., Wang, C., Zhang, J., Niu, G. & Tang, J. Vapor transport deposition of antimony selenide thin film solar cells with 7.6% efficiency. *Nat. Commun.* **9**, (2018).

58. Choi, Y. C., Mandal, T. N., Yang, W. S., Lee, Y. H., Im, S. H., Noh, J. H. & Seok, S. I. Sb_2Se_3-Sensitized Inorganic-Organic Heterojunction Solar Cells Fabricated Using a Single-Source Precursor. *Angew. Chemie, Int. Ed.* **53**, 1329–1333 (2014).

59. Lu, S., Zhao, Y., Chen, C., Zhou, Y., Li, D., Li, K., Chen, W., Wen, X., Wang, C., Kondrotas, R., Lowe, N. & Tang, J. Sb_2Se_3 thin-film photovoltaics using aqueous solution sprayed SnO_2 as the buffer ayer. *Adv. Electron. Mater.* **4**, 1–8 (2018).

60. Phillips, L. J., Savory, C. N., Hutter, O. S., Yates, P. J., Shiel, H., Mariotti, S., Bowen, L., Birkett, M., Durose, K., Scanlon, D. O. & Major, J. D. Current enhancement via a TiO_2 window layer for CSS Sb_2Se_3 solar cells: performance limits and high Voc. *Ieee J. Photovoltaics* **Submitted**,

61. Zakutayev, A. Brief review of emerging photovoltaic absorbers. *Curr. Opin. Green Sustain. Chem.* **4**, 8–15 (2017).

4. Experimental methods

In this chapter the experimental methods used in this thesis are described, including those for growth and processing of materials (Section 4.1), materials characterisation (Section 4.2) and device characterisation (Section 4.3). A description of the exact experimental conditions used are deferred until the appropriate results chapters.

4.1 Growth techniques

4.1.1 Thermal evaporation

Thermal evaporation is a physical vapour deposition technique (PVD). The source material is placed in a boat or crucible, the evaporation chamber is evacuated and the vessel heated until the source material melts and the material begins to evaporate and condense on the substrate. During the evaporation process the temperature is carefully controlled to maintain a steady deposition rate, monitored in-situ. The materials deposited by thermal evaporation in this work are: Cu, Bi, Sb_2Se_3, Se, Sb and Au.

The Cu, Bi, Se and Sb were evaporated from a 0.005" dimple Mo boat. The Sb_2Se_3 was evaporated from a carbon crucible in a W basket heater. The Au was evaporated from a Mo thin trough boat. Boats and baskets were all obtained from Kurt J. Lesker Ltd.

Thicknesses were measured in situ using a quartz crystal microbalance (QCM). The QCM is situated in the deposition chamber such that it is subjected to vapour flux during the deposition process. The quartz crystal is oscillated during the deposition, its resonant frequency is sensitive to change in density, lowering as material is deposited onto the surface of the crystal. The change in oscillation frequency of crystal is used to calculate the deposition rate and total thickness of the film.

Two thermal evaporation systems were used, a Leybold Vacuum Œrlikon Univex 300 for Au and a Moorfield MiniLab 080 for the other materials.

4.1.2 RF sputtering

Sputtering is another PVD process performed under vacuum. Material from the sputtering target is dislodged by impact from charged ions and coats the surfaces inside the sputtering chamber. The sputtering process typically makes use of inert gasses (Ar in all cases in this work) to form the charged ions used. An electric field is applied between the target and substrate, ionizing the Ar gas which is confined by the magnetic field at the target. The materials deposited by sputtering in this work were CdS and ZnS, both of which require an AC (or radio frequency, RF) electric field since a DC field would cause charge accumulation and heating of the target. The magnetic field is from a “balanced” configuration with the magnets in the sputtering gun (see Figure 4.1) so as to confine the Ar plasma in a toroidal region at the surface of the target.

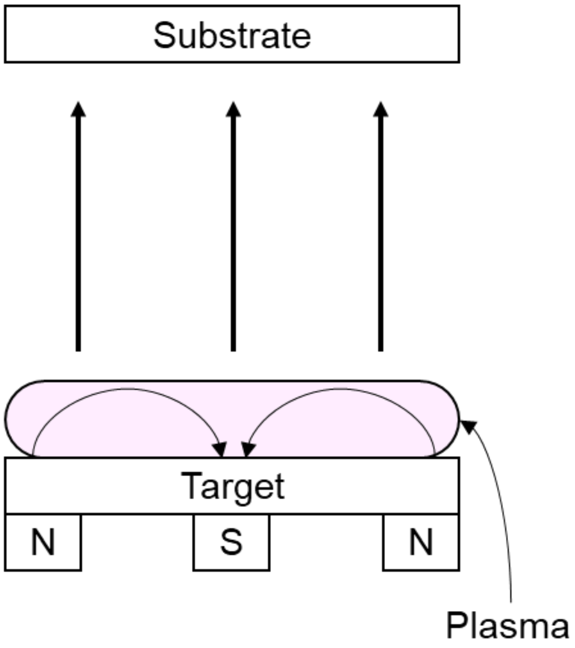

Figure 4.1: Schematic of the sputtering gun and the plasma confinement in a balanced magnetron.

4.1.3 Spin coating

The solution-processed steps in the PV devices made here were carried out be spin coating. This deposition process involves the application of the solution to be deposited onto the desired substrate. The substrate can either be stationary (i.e. static) or rotating (i.e. dynamically) as the solution is applied. Rotation causes the deposited solution to rapidly spread across the substrate by centrifugal force, resulting in smooth films.

Here spin coating was carried out dynamically using an Ossila Ltd. spinner for films deposited in a nitrogen atmosphere and a Laurell WS-650MZ-23 for those deposited in air.

4.1.4 Chalcogenisation

The chalcogenisation steps in this work were performed in the quartz envelope of a sublimation deposition reactor. Samples were placed in a graphite box with the chalcogen of choice (S, Se) placed in a trench around its outside. The quartz vessel was then evacuated and purged through with dry nitrogen. During the chalcogenisation process the background pressure in the vessel was maintained at a desired pressure by balancing a constant inflow of dry nitrogen with the pumping output (scroll pump) using a Baratron pressure controller. The sample may be heated from both above and below and its temperature was measured by a K-type thermocouple in contact with the graphite box.

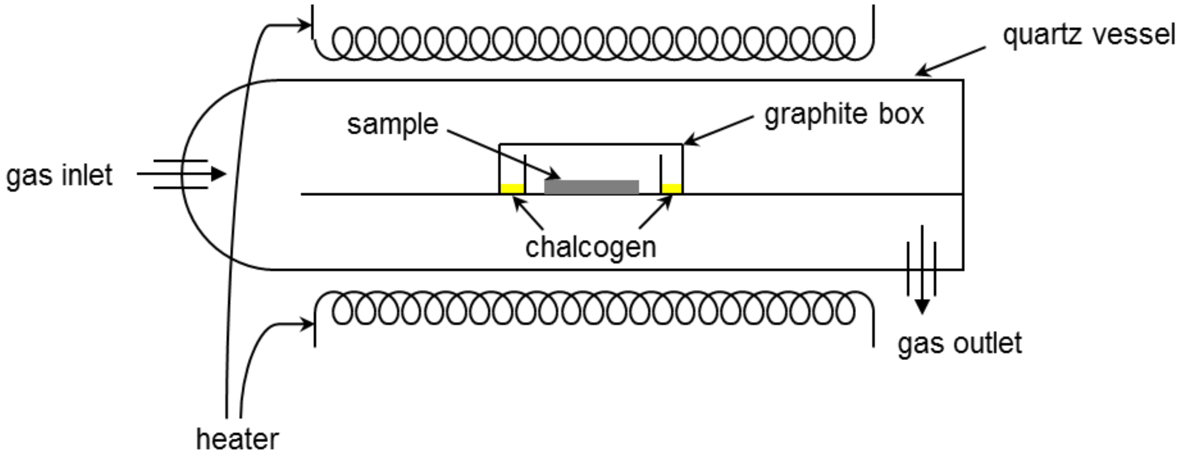

Figure 4.2: A schematic diagram of the apparatus used for the chalcogenisation reactions.

In order to ensure the vapour pressure from the chalcogen gas did not cause the graphite box lid to dislodge thus allowing the gas to escape through the pump, the background gas pressure was chosen to be greater than the chalcogen pressure. The data in Figure 4.3 were consulted for this purpose.

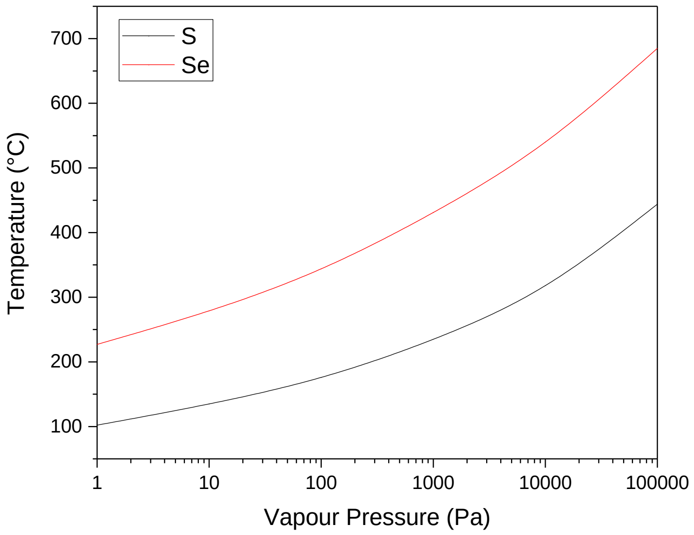

Figure 4.3: The relationship between vapour pressure and temperature for S and Se[1].

4.2 Material characterisation

4.2.1 UV-Vis-NIR

For the UV-Vis-NIR spectroscopy of thin-films of materials an integrating sphere is usually used to collect photons transmitted through or reflected by the film being probed. Monochromated light is shone onto the sample and collected in an integrating sphere immediately behind for transmission data. For reflection the light is once again shone onto the sample and the specular reflected light is collected in the integrating sphere. The non-specular portion of the reflection (i.e. scattered) is, therefore, unaccounted for in the data.

The absorption coefficients, α, as a function of photon energy, $h\nu$, were calculated using the simplified formula:

$$\alpha(h\nu) = \frac{1}{t}\ln\left(\frac{(1-R(h\nu))^2}{T(h\nu)}\right) \qquad \text{Equation 4.1}$$

where *t* is the thickness, *R* the reflectance and *T* the transmittance of the film.

It is common in the field of photovoltaics, particularly for new materials where the parameters are not already well-defined, to determine band gaps and the nature of the transition (i.e. direct or indirect, forbidden or allowed) by method of Tauc plots.

These absorption coefficients may be used to this end in accordance with the relationship in Equation 4.2:

$$\alpha(h\nu) = \frac{A}{h\nu}\left(h\nu - E_g\right)^{\frac{1}{r}} \qquad \text{Equation 4.2}$$

where *A* is a constant, E_g is the band gap of the material and *r* is an index, each dependent on the transition type[2].

The Tauc plots are created by plotting the curve of hv versus $(\alpha hv)^r$ where r is 2, ½, ⅔ and ⅓ for direct allowed, indirect allowed, direct forbidden and indirect forbidden respectively. The instance with the most linear portion is then selected, the transition assumed to be of the type associated with the index to which the (αhv) was raised and the band gap determined by extrapolation of this linear portion down to the horizontal axis i.e. when $hv = E_g$.

4.2.2 X-ray diffraction (XRD)

X-ray diffraction is an analytical technique for the identification of crystalline phases in a sample. The Bragg condition for constructive interference is achieved when Equation 4.3 is satisfied:

$$n\lambda = 2d_{hkl}\sin(\theta) \qquad \text{Equation 4.3}$$

where n is an integer, λ is the wavelength of the beam (1.5406 Å when using the Cu K-α energy X-rays used here), d is the lattice spacing for the planes having Miller indices h, k and l, and θ is the angle of incidence of the beam. These variables are visualised in Figure 4.4.

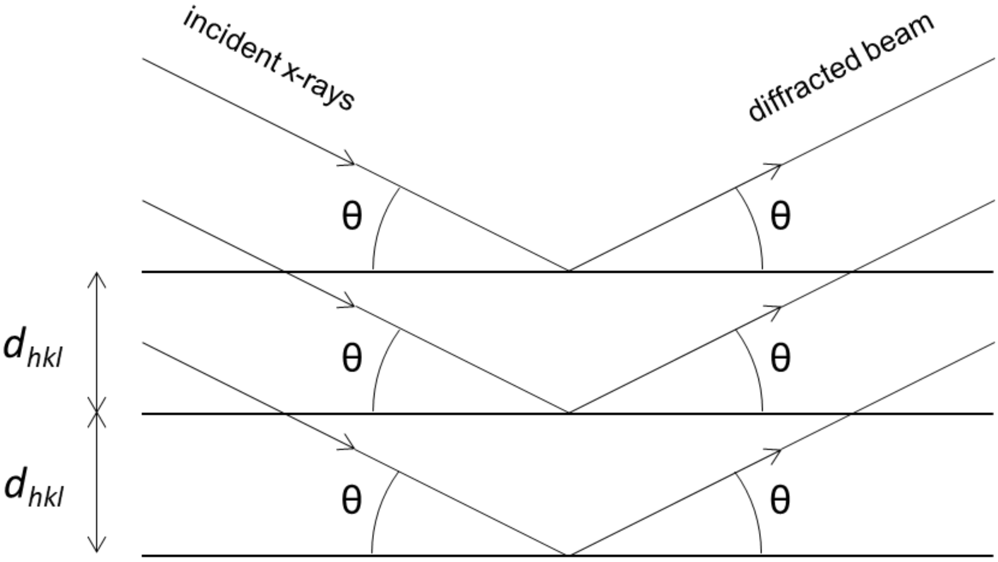

Figure 4.4: A perfect crystal with spacing between planes, d_{hkl}, with the angle θ between the surface and the incident or diffracted beams.

The crystallographic texture of a film may be quantified from XRD data using the Harris texture coefficient method[3]. The peak intensity for the d-spacing of each (hkl) plane may be compared to the intensity expected in a completely randomly oriented sample (such as a powder). The texture coefficient (TC) of an (hkl) plane is given by:

$$TC(hkl) = \frac{\frac{I(hkl)}{I_0(hkl)}}{\frac{1}{N}\Sigma_N \frac{I(hkl)}{I_0(hkl)}} \qquad \text{Equation 4.4}$$

where $I(hkl)$ is the measured intensity of the (hkl) plane, $I_0(hkl)$ is the corresponding powder intensity and N is the number of planes being considered. The relative degrees to which two films have a preferred orientation may then be compared by taking the standard deviation of the TCs for each film.

XRD in this work was performed on a Phillips X.Pert system (Chapter 5) and a Rigaku SmartLab X-ray diffractometer (Chapters 6 & 7).

4.2.3 Scanning electron microscopy (SEM)

Imaging of materials is possible using a scanning electron beam, with a higher resolution than optical microscopy. An electron beam is generated from either a filament or a field emission gun and accelerated towards the sample being interrogated. Images can be formed pixel-by-pixel using the backscattered beam or secondary electrons. The backscattered beam arises from the portion of the incident beam which elastically scatters from the sample. The secondary electron signal is generated by the primary electron beam ionising electrons from the sample. Backscattered electrons are more sensitive to atomic mass variation across the sample whereas the secondary electron signal contains more topographical information.

SEM in this work was conducted using a JEOL 7001F Field Emission SEM.

4.2.4 Transmission electron microscopy (TEM)

Compared to SEM, the electron beam in TEM employs higher energy electrons. Typical acceleration voltages used are 200-300 kV compared to the 5-20 kV of SEM. The electron beam passes through the specimen, is magnified and the image displayed on a phosphorescent screen or captured using photographic plates or a CCD. Specimens for TEM are required to be electron-transparent, having thickness of order 100 nm (dependent on average atomic number of the material). For imaging of PV device cross sections, a cross-section lamellar of the device must be prepared and mounted to a grid.

TEM can be run in two modes: conventional TEM, where an area of the specimen is illuminated, and the image formed simultaneously across the area; and STEM mode (scanning TEM) where a narrow probe is raster scanned across the sample.

The TEM and STEM/EDX data in this thesis were collected courtesy of Karl Dawson at the University of Liverpool

4.2.5 Energy dispersive X-ray (EDX) spectroscopy

The electron beam in both SEM and TEM ionises the atoms in the materials being probed. Higher energy electrons drop down into these newly empty states, emitting a photon with energy equal to the difference in energy of the two states. The photon energy is characteristic of the element and the intensity of the signal is proportional to the number of atoms of the element in the excitation area.

EDX may be performed in both SEM and STEM environments to give elemental maps of the area being investigated.

4.2.6 Four-point probe

A four-point probe was used to measure the sheet resistivities of the films in this work. A line of four probes are placed in contact with the sample. The outer two probes (force probes) are used to supply current while the inner two probes (sense probes) detect the voltage drop. The sheet resistivity, ρ_S, of the films is then calculated in accordance with Equation 4.5.

$$\rho_s(\Omega \cdot sq^{-1}) = \frac{\pi}{\ln(2)} \cdot \frac{V}{I} \qquad \text{Equation 4.5}$$

where I is the supply current and V is the voltage drop[4].

4.3 Device characterisation

4.3.1 Current-voltage (*J-V*) response

The performance of devices was primarily investigated by the measurement of current-voltage response to determine their V_{oc}, J_{sc}, FF and PCE. For these measurements devices are placed under a solar simulator and the current produced is measured as a function of the applied voltage.

A TS Space Systems solar simulator was used for all J-V measurements, the power density being calibrated to 100 mW·cm^2 at the sample height using a PVMeasurements GaAs reference cell. Applied voltage was supplied and current measured by a Kiethley 2400 source meter.

4.3.2 External quantum efficiency (EQE)

The external quantum efficiency of a device is, in its simplest form, the ratio of the number of photons in to electrons out as a function of photon energy. The current generated by the cell is measured as the cell is illuminated with an incident beam of monochromated light, the quantum efficiency being measured by comparison with a reference with a Si photodiode. A Bentham PVE 300 system was used for this work.

4.3.3 X-ray photoelectron spectroscopy (XPS)

X-ray photoelectron spectroscopy is a surface sensitive technique where the electrons in the sample are excited using a monochromatic x-ray beam.

Electrons with sufficient energy to overcome their binding energy can be detected and their kinetic energy may be interpreted to determine the electron binding energies at the surface of the sample.

XPS data used in this thesis were collected courtesy of Thomas J. Whittles at the University of Liverpool from samples grown by the author.

4.3.4 Time of flight secondary ion mass spectroscopy (ToF SIMS)

Secondary ion mass spectroscopy involves a beam of heavy ions (typically gallium or caesium) incident on the sample being interrogated. This ion beam dislodges secondary ions belonging to the materials in the sample for analysis by mass spectroscopy. The ions are accelerated by an electric field and their mass-to-charge ratio is determined based from either their time of flight or deflection in a magnetic field. SIMS is capable of measuring the vertical distribution of both the major and minor components of a solid.

ToF SIMS data were obtained by Mark A. Farnworth at Pilkington Ltd. from samples grown by the author.

4.3.5 Summary of characterisation techniques

Table 4.1 lists the characterisation techniques used in this thesis, their physical principle where applicable and the information to be gained from each.

Table 4.1: Experimental techniques used in this thesis for the purpose of characterising films and devices.

Technique	**Probe**	**Detected**	**Physical Principle**	**Information Gained**
UV-Vis-NIR	Photons	Photons		Optical properties
XRD	X-rays	X-rays	Bragg's law	Chemical composition
SEM	Electrons	Electrons		Surface morphology
TEM	Electrons	Electrons		Cross-section morphology
EDX	Electrons	X-rays	Auger effect	Elemental composition
J-V	Photons	Electrons	Photovoltaic effect	Device working parameters
EQE	Photons	Electrons	Photovoltaic effect	Device spectral response
XPS	Photons	Electrons	Photoelectric effect	Electronic band structure
ToF SIMS	Ions	Ions		Chemical composition

References for Chapter 4

1. Lide, D. R. *CRC Handbook of Chemistry and Physics*. *78th Edition* (Taylor & Francis Inc, 2004).
2. Neumann, H., Reccius, E., Sobotta, H., Physik, S., Schumann, B. & Kuhn, G. Growth and Optical Properties of $CuGaTe_2$ Thin Films. **61**, 13–22 (2000).
3. Kim, K. H. & Chun, J. S. X-ray studies of SnO_2 prepared by chemical vapour deposition. *Thin Solid Films* 287–295 (1986).
4. Smits, F. M. Measurement of Sheet Resistivities with the Four-Point Probe. 711–718

5. Fabrication of Cu-Bi-S,Se films and device structures

5.1 Introduction

Chapter 2 presented an overview of compounds in the family Cu-Sb,Bi-S,Se. These materials are of interest since some of them have properties appropriate for PV applications while the constituent elements are both cheap and Earth-abundant. Of them Cu_3BiS_3 is of particular interest since it has a near-optimum band gap (1.40 eV[1]), high optical absorption ($\geq 10^4$ cm^{-1}) and p-type conductivity but this has not yet been exploited in devices. Moreover, with there being some 80 papers on Cu_3BiS_3, 60 of which mention PV it is surprising that there are so few device results reported. The literature at the time of writing contains just three reports. That from Yin (2014) describes a TiO_2/dye cell having an I_2-KI electrolyte and sensitised with Cu_3BiS_3. [2] As for dye cells sensitised with any of a wide range of absorbers, Yin's device achieved a conversion efficiency of just 1.28%. Such structures are not expected to mature to become highly efficient, stable technologies. Mesa reports two conventional planar structures having ZnS and In_2S_3 window layers, but neither was photoactive[3].

Hence an opportunity remains to investigate the use of Cu_3BiS_3 in planar PV structures and this is the subject of this chapter. The approach here was to use the post-growth chalcogenisation of Cu-Bi metal "precursor films" to create the compound. Both sulfurisation and selenisation were utilised. Characterisation was by XRD, SEM and UV-vis-NIR. Device structures comprising glass/Mo/Cu_3BiS_3/CdS/ITO and glass/Mo/Cu_3BiS_3/ZnS/ITO were fabricated and the current-voltage response was evaluated in the dark and under AM1.5 illumination conditions.

5.2 Experimental

5.2.1 Growth trials and formation of Cu_3BiS_3

a) <u>Substrates</u>

Two substrate types were used in this work:

i) <u>Plain soda-lime glass</u>

Glass substrates (Optiwhite, NSG Ltd.) were rinsed and scrubbed with deionised water followed by isopropanol and dried with compressed nitrogen.

ii) <u>Mo-coated soda-lime glass</u>

Glass substrates cleaned as above were coated with Mo by DC magnetron sputtering. The 2” target was 99.99% pure (Pi-KEM) and sputtering was conducted in an AJA Orion chamber under Ar at 3 mTorr for 1 hour at a power of 100 W with the substrate temperature being 400°C. These conditions yielded films typical sheet resistances of 1.9 Ω/sq as measured using a four-point probe. Semiconductors made on these Mo/glass substrates were incorporated into devices as represented in Section 5.4)

b) <u>Cu-Bi precursor films</u>

Cu-Bi films for subsequent chalcogenisation were deposited using a range of different thickness ratios. From the density and atomic masses of the elements a thickness ratio of 1:1 Cu:Bi corresponds accurately to a 3:1 atomic ratio. Hence it was possible to control the atomic ratio of Cu:Bi in the range 18:1 to 3:2. Both the Cu and the Bi films were deposited by evaporation (Moorfield MiniLab 080) using 99.999% Cu shot (Alfa Aesar) and 99.99% Bi pellets (Advent Research Materials). Cu was deposited first with the Bi being the uppermost. The thicknesses of the films were monitored using an in-situ quartz crystal monitor. This was calibrated by measuring the thicknesses of the metal films by stylus profilometry (Ambios XP-200), the films having been scored through to the substrate using a scalpel blade.

c) Sulfurisation of Cu-Bi precursor films

The general method used for sulfurisation is explained in Section 4.1.4 and the details of the conditions used here follow. Sulfurisation was undertaken by enclosing the Cu-Bi precursor films on their substrates in a graphite box with 500 mg of elemental S. This was then placed in a quartz tube, purged with dry nitrogen and heated for 30 minutes at the chosen temperature under a background pressure of 300 Torr of N_2.

Sulfurisation was trialled for temperatures between 375 and 450°C. Figure 4.3 shows the vapour pressure-temperature relationship for S. The background pressure of 300 Torr (= 40 kPa) was chosen to correspond to the vapour pressure of elemental sulfur at 375°C i.e. so as to keep the graphite box lid in place so as to maintain the sulfurisation environment.

i) Optimisation on glass

This was explored using the full range of Cu:Bi atomic ratios (18:1 – 3:2) and temperatures as above with a total of 48 samples being prepared. Cu_3BiS_3 films prepared on glass by the author using the conditions established during these trials were subjected to photoelectron emission studies in order to determine the ionisation potential and work function of the material. Results of this are included in Tom Whittles' PhD thesis[4] and a paper[5] and hence only a summary will be presented here in Section 5.4

ii) Optimisation on Mo/glass

Trials on Mo coated soda-lime glass substrates were commenced using the optimum conditions determined for glass as the starting point and refined thereafter to compensate for difference in the process caused by the surface. The success of the sulfurisation trials in creating the desired phase was monitored by XRD using a Phillips X.Pert system.

5.2.2 Growth trials and formation of Cu-Bi-Se

The selenisation process for metallic precursor films is explained in Section 4.1.4 and is similar to the sulfurisation process. These trials were performed on glass substrates (see 5.2.1.a.i.). In these experiments the selenisation process was performed on Cu films, Bi films, and Cu-Bi stacks by enclosing each of these precursor films on their substrates in a fresh graphite box with 100 mg of elemental Se. The Cu-Bi films used had a 3:1 Cu:Bi ratio. Samples were then heated after purging with dry nitrogen in a quartz tube under a background pressure of 300 Torr of N_2.

Selenisation was undertaken at temperatures of 350, 400 and 450°C and sets of 6 for each of the Cu, Bi, and Cu-Bi precursor films were used. Figure 4.3 shows the vapour pressure-temperature relationship for Se. The background pressure of 300 Torr was chosen since vapour pressure of Se is lower than that of S at equal temperatures thus the lid of the graphite box would remain in place.

Success of growth of Cu-Se, Bi-Se, and Cu-Bi-Se films were again evaluated by XRD of the selenised films and the spectra of the Cu-Se and Bi-Se films used for comparison with the ternary system films.

5.2.3 Formation of devices

Devices were made with the structures glass/Mo/Cu_3BiS_3/CdS/ITO and glass/Mo/Cu_3BiS_3/ZnS/ITO. The Cu_3BiS_3 layers were grown on sputtered Mo substrates as described in Section 5.2.1; the CdS, ZnS, and ITO layers were grown by RF sputtering from 2-inch targets of 99.99% purity and with 10% Sn-doping in the ITO. The CdS was deposited onto the device structure at 200°C with a power of 50 W, Ar pressure of 5 mTorr for 30 minutes to give a layer thickness of 50 nm. The ZnS was deposited onto the device structure at room temperature with a power of 50 W, Ar pressure of 5 mTorr for 50 minutes again to give a layer thickness of 50 nm. ITO was deposited at either 100°C (4.6 Ω·cm) or at room temperature (37.9 Ω·cm). However since it is known that Cu is a hole trap in CdS [6] and can cause device failure, the lower growth temperature was selected for use in devices to prevent out-diffusion of the Cu from the Cu_3BiS_3. Room temperature deposition of ITO was carried out at a power of 50 W under 3 mTorr of Ar for 2 hours.

5.2.4 Characterisation

Films and devices were inspected using the techniques outlined in Chapter 4. Before any other form of characterisation, the films of Cu_3BiS_3 were visually inspected for film adhesion and coherence in addition to colour and finish. Films were interrogated with UV-Vis-NIR, SEM, and XRD. *J-V* and EQE were attempted on the completed device structures.

5.3 Results

5.3.1 Results of sulfurisation of metal stacks on glass

Photographs of the films produced at 375, 400 and 425°C, each using the twelve Cu:Bi atomic ratios in the range 18:1-3:2 are shown in Figure 5.1

Films sulfurised at 375°C were generally continuous and uniform across the whole area of the glass substrates used. Those with higher Bi contents (Cu:Bi 18:5-3:2) were generally brown in colour, while those with increasing Cu contents (18:5-18:1) tended to become blue/brown in colour. Those grown with highest Cu contents (9:1 and 18:1) were discontinuous and suffered loss of material from the centre of the substrates. That grown with the very highest Cu content (18:1) had a large area of complete film loss.

The visual appearance of the films grown at 400°C was generally similar, although the colours of the film tended to be slightly silvery and reflective. Again, those having the highest Cu contents had suffered significant material loss. Films grown at 425°C showed strong evidence of visible film break up, particularly as the Cu:Bi ratio exceeded 18:7 when the films became increasingly flakey. Material loss for the highly Cu-rich films was very significant.

Processing films at 450°C (not shown) caused very severe material loss, there being large areas of bare glass substrate visible on all the samples for all composition ratios. These films were not suitable for further characterisation by optical and XRD methods nor for any device making, hence sulfurisation at this temperature was discontinued.

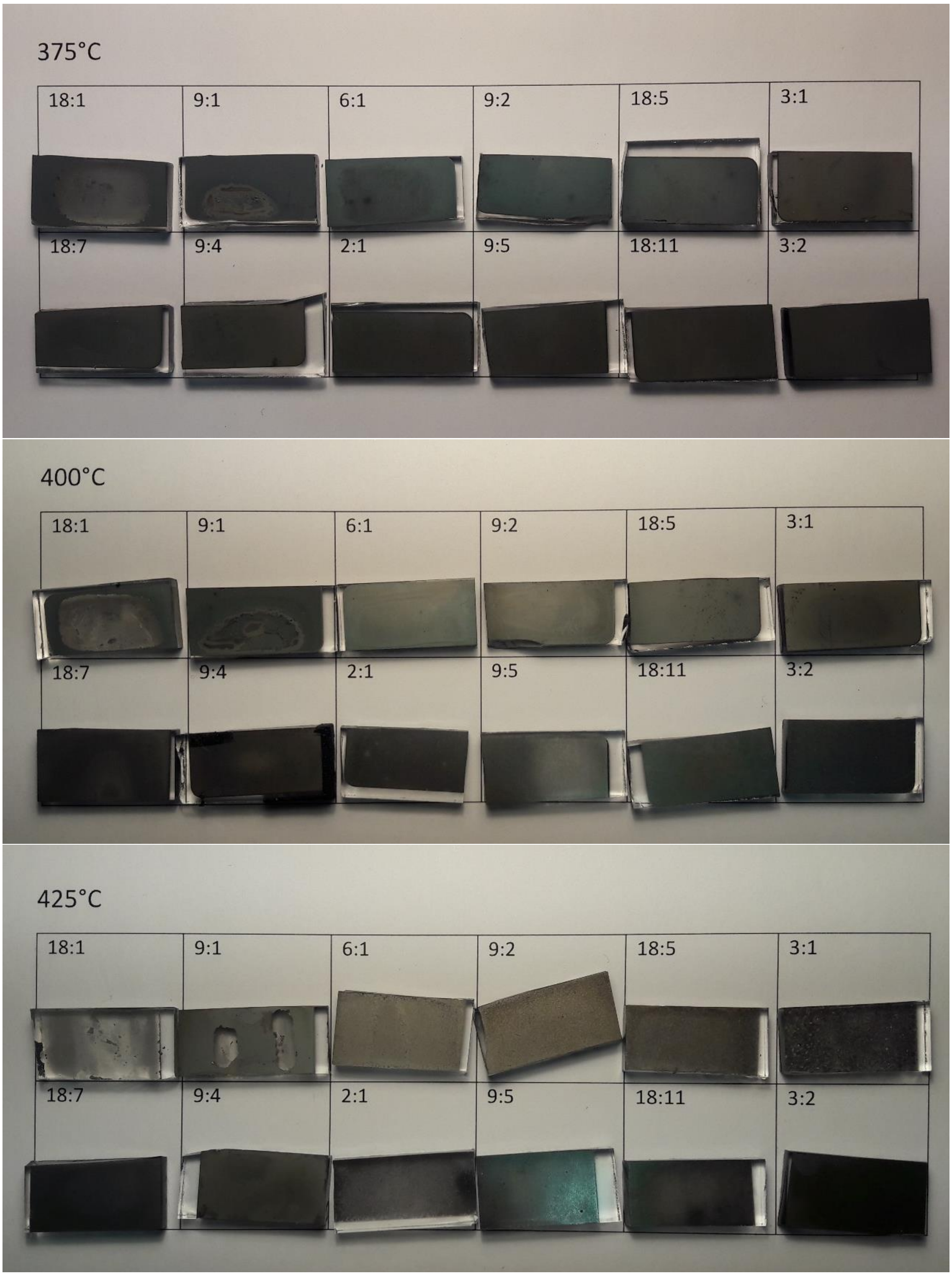

Figure 5.1: Photograph of Cu-Bi-S samples on glass with Cu:Bi atomic ratios varying between 18:1 and 3:2, sulfurised at 375, 400 and 425°C. Precursor films sulfurised at 450°C left bare substrates and thus photographs are not included.

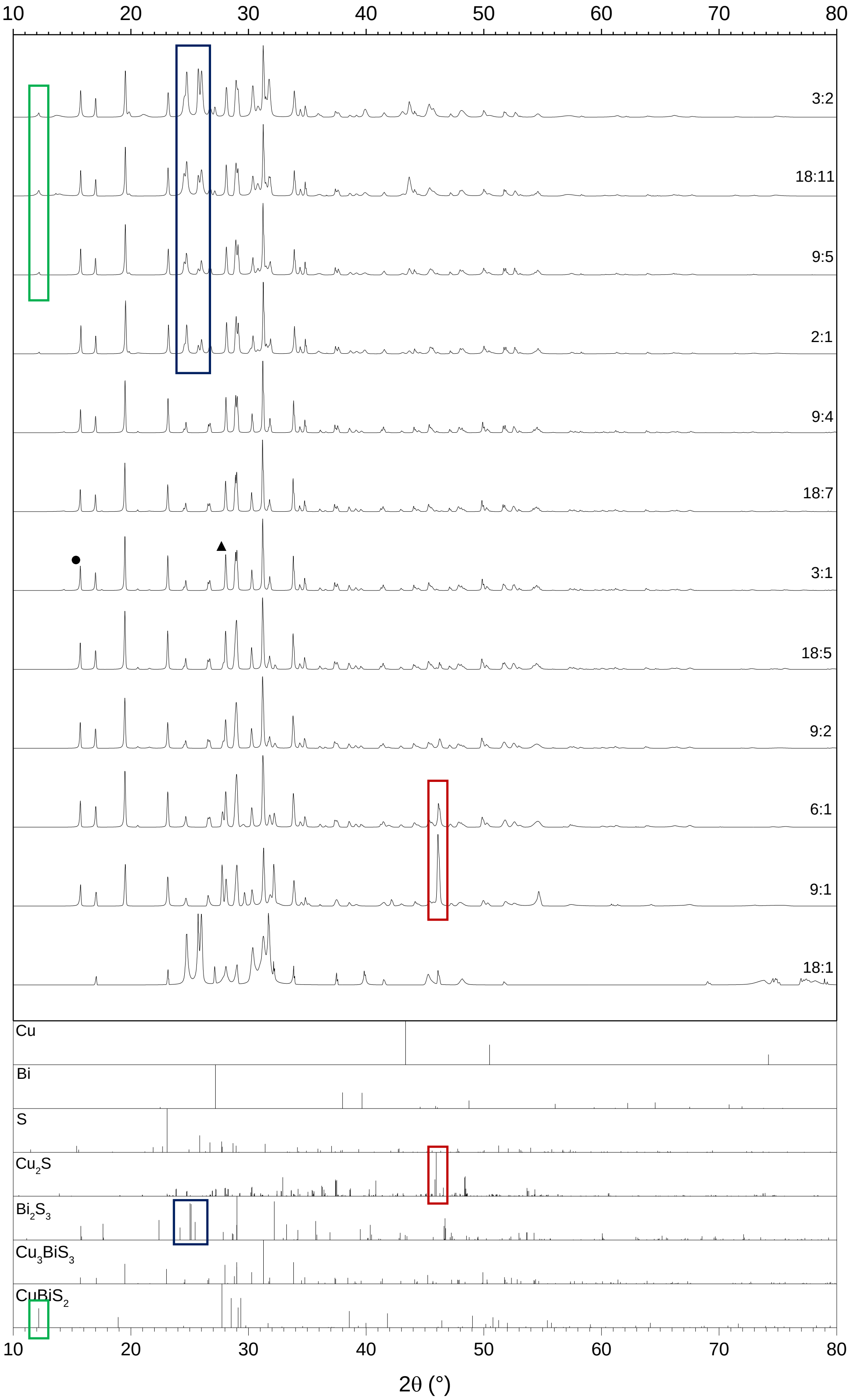

Figure 5.2: XRD spectra of Cu-Bi stacks sulfurised at 375°C with reference spectra for the target phase. Cu_3BiS_3, and other possible ternary, binary and elemental impurity phases. The Cu:Bi atomic ratio of the precursor films is indicated for each experimental XRD pattern. The desired phase was achieved with minimal impurity phases over the Cu:Bi range 9:5-9:2.

Figure 5.2 shows XRD patterns of the precursor films sulfurised at 375°C. The Cu: Bi atomic ratios are shown alongside each spectrum. The figure also shows reference spectra of the target phase and the likely elemental, binary and ternary phases that could be present as impurities in the films. From the figure it may be seen that a very wide range of Cu:Bi ratios in the precursor films can generate the desired Cu_3BiS_3 phase. However, those films prepared using the more extreme Cu- and Bi-rich precursor films contain greater amounts of unwanted impurity phases. For the case of the most Cu-rich films (Cu:Bi 18:1), there was significant loss of material making the acquisition of an XRD spectrum difficult. Nevertheless, there is evidence that the Cu_3BiS_3 phase is present alongside impurity phases including Cu_2S. Upon decreasing the Cu:Bi ratio into the range 9:1-18:5, the desired phase remains present but the amount of Cu_2S impurity is present in decreasing quantities as the Bi fraction increases. This may be seen by inspecting the variation of the intensity of the (630) peak of Cu_2S at $2\theta = 45.96°$ (outlined with a red box) in Figure 5.2. At the Bi-rich extreme of the sample set a cluster of peaks representing the presence of Bi_2S_3 is present, these being (301), (111), and (103) at 24.91°, 25.07°, and 25.16° (outlined with a blue box). However the intensity of these peaks progressively declines as the Bi fraction is decreased and the Cu:Bi ratio changes from 3:2 to 2:1. It should also be mentioned that for the three most Bi-rich compositions the $CuBiS_2$ phase appears as a minor component as evidenced by its (002) peak at 12.20° (outlined with a green box).

Hence Figure 5.2 shows that the region of compositions centred on the ideal composition of 3:1 contains the most phase pure Cu_3BiS_3 material. In particular the compositions 9:4, 18:7 and 3:1 are all capable of generating the target phase upon sulfurisation. It may therefore be said that the composition processing window at 375°C is tolerant to a wide range of precursor film compositions.

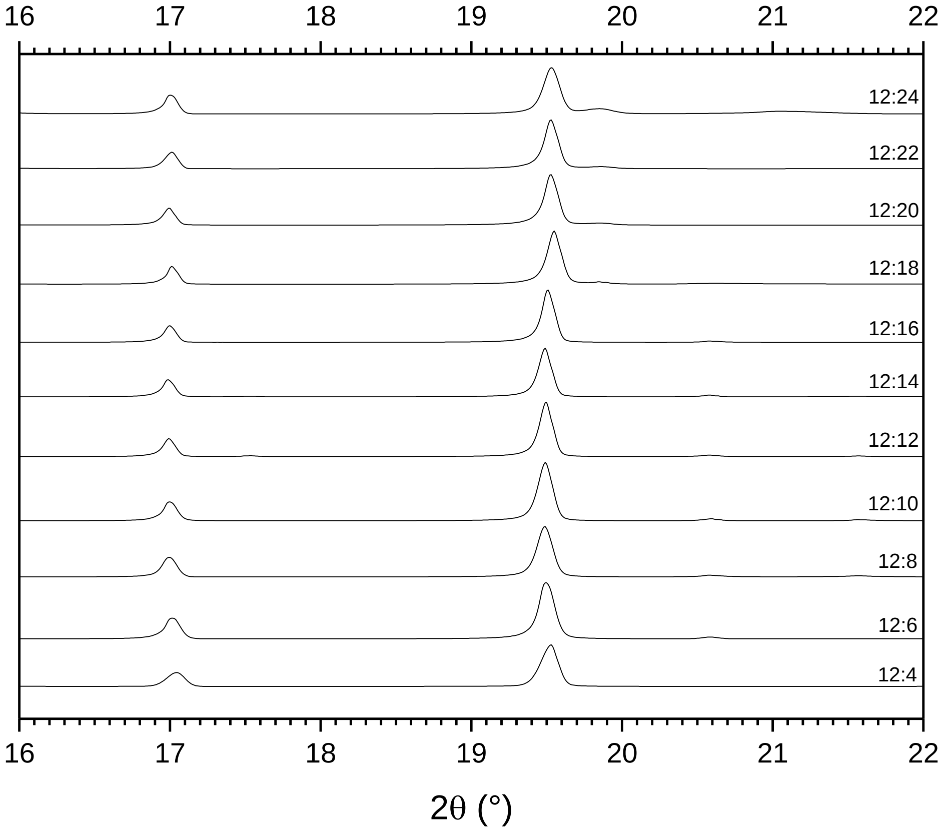

Figure 5.3 XRD spectra of Cu-Bi stacks sulfurised at 375°C between 2θ angles of 16 and 22°, displaying the (020) and (111) peaks.

Figure 5.3 shows the (020) and (111) peaks from the XRD spectra shown in full in Figure 5.2. The peak positions have a spread of 0.03° and 0.06° for (020) and (111) orientations respectively. This variation is not enough to be indicative of shifts due to significant strain or chemical composition variation.

Figure 5.4 shows an expanded XRD pattern of the 2θ = 15-35° region for the 3:1 atomic ratio film sulfurised at 375°C. It may be seen from the reference spectrum for Cu_3BiS_3 in the same figure that the film is substantially phase pure. Table 5.1 shows the XRD data including texture coefficients for each peak determined by comparison of the experimental intensities with the random powder values. The average of the texture coefficients is 1.41 with the standard deviation being 0.52. Two peaks stand out as having relatively high texture coefficients: (011) at 2.33 and (220) at 3.05 marked with a circle and triangle respectively on Figure 5.2. Overall though the close spread of texture coefficients around the average value indicates that the film has close to random texture.

SEM micrographs of films sulfurised at 375°C are shown in Figures 5.5a and b, and have the most consistently complete surface coverage of all the temperatures trialled. Nevertheless, pinholes are visible in all films. The grain size is approximately 800 nm.

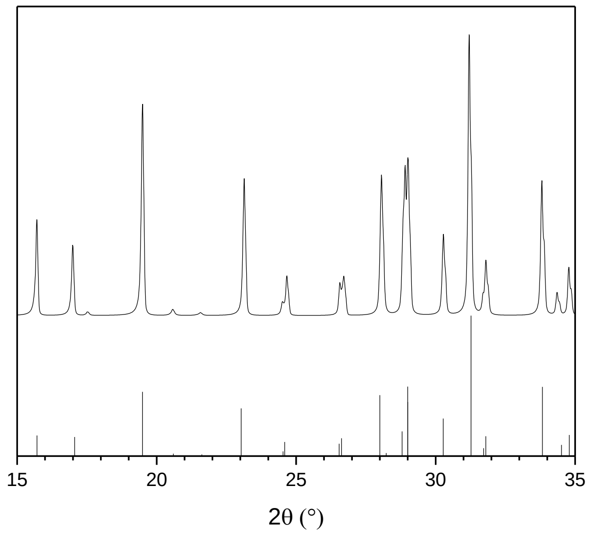

Figure 5.4: Segment of XRD spectrum from the 3:1 atomic Cu:Bi ratio film sulfurised at 375°C between 15 and 35° with the Cu_3BiS_3 reference spectrum.

Table 5.1: Texture analysis on the XRD spectrum taken from the 3:1 atomic Cu:Bi ratio film sulfurised at 375°C.

Experimental		Literature					Texture
2θ (°)	Intensity	2θ (°)	Intensity	h	k	l	coefficient
15.70	0.34	15.71	0.15	0	1	1	2.33
16.99	0.25	17.06	0.14	0	2	0	1.84
17.53	0.01	--	--	--	--	--	--
19.50	0.75	19.49	0.46	1	1	1	1.65
20.58	0.02	20.60	0.02	1	2	0	1.31
21.57	0.01	21.62	0.01	0	2	1	0.94
23.14	0.49	23.03	0.34	2	0	0	1.43
24.51	0.05	24.53	0.03	1	2	1	1.49
24.67	0.14	24.59	0.10	2	1	0	1.41
26.57	0.12	26.54	0.09	0	0	2	1.35
26.71	0.14	26.63	0.13	2	0	1	1.11
28.06	0.50	28.00	0.43	2	1	1	1.15
28.91	0.53	28.80	0.18	2	2	0	3.05
29.01	0.56	29.00	0.49	1	0	2	1.14
--	--	29.00	0.39	0	3	1	--
30.28	0.29	30.27	0.27	1	1	2	1.08
31.20	1.00	31.27	1.00	1	3	1	1.00
31.80	0.20	31.80	0.14	2	2	1	1.40
33.81	0.48	33.83	0.49	1	2	2	0.97
34.35	0.08	34.51	0.08	0	4	0	1.04
34.77	0.17	34.79	0.15	2	3	0	1.14

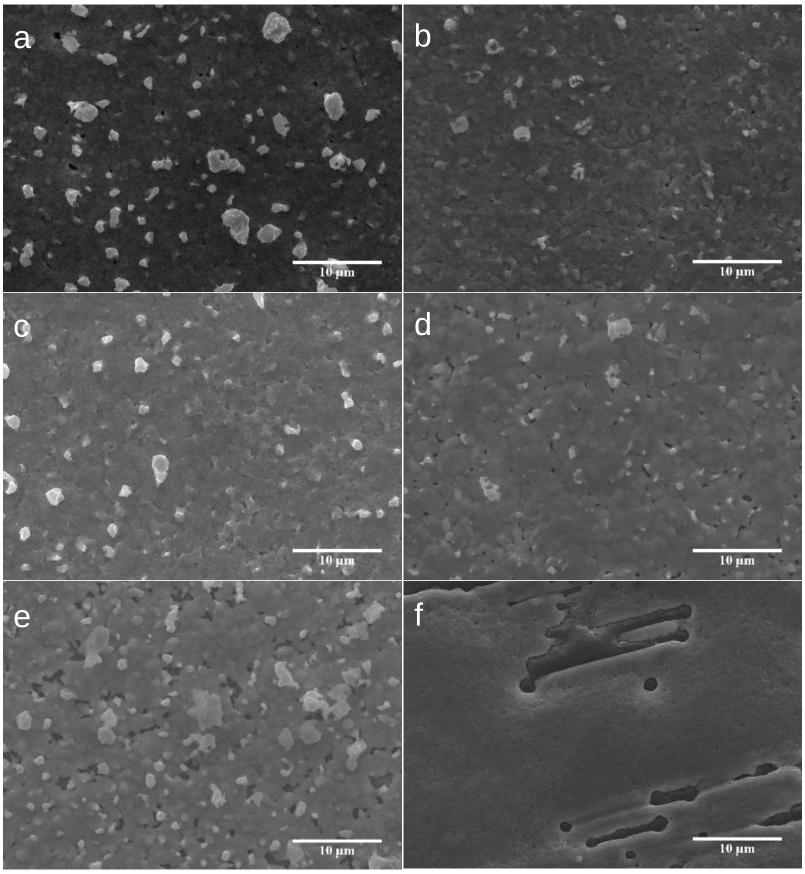

Figure 5.5: SEM micrographs of 3:1 Cu:Bi ratio Cu_3BiS_3 films sulfurised at (a, b) 375°C, (c, d) 400°C, and (e, f) 425°C. The bright grains most visible in (a) and present in most of the other micrographs were due to charge artefacts.

Figure 5.7 shows the XRD patterns and reference spectra for the complete composition range of precursor films sulfurised at 400°C. For the most Cu-rich sample (Cu:Bi 18:1) the XRD pattern shows a collection of very broad peaks that may indicate a breakdown of the crystal structure, perhaps by amorphisation. There is a sharp peak at $2\theta = 45.96°$ and attributed to Cu_2S (indicated in red). This film suffered very considerable material loss during processing making it unusable for further characterisation or devices. Similar to the case for films sulfurised at 375°C, the Cu-rich films all contain Cu_2S and decreasing the Cu fraction caused a corresponding decrease in the amount of this impurity phase. On the contrary, at the Bi-rich end of the series (3:2-2:1, in Figure 5.7) the spectra comprise a small number of sharp peaks. That at 25° represents a closely spaced cluster of peaks assigned to Bi_2S_3 (blue). In addition, there is a weak peak due to $CuBiS_2$ at 12.20° (green). The strong peak at 43.35° (orange) is most likely to be elemental Cu. However, the peak at 30.90° (yellow) could not be assigned by comparison with any of the reference spectra for any of the elements, binaries or ternaries expected to be present in this system. It was concluded that Bi-rich films comprise a mixture of Bi_2S_3, elemental Cu, a small amount of $CuBiS_2$, and an unidentified phase.

As for the case of films sulfurised at 375°C, those sulurised at 400°C and having compositions clustered around the ideal 3:1 composition predominantly comprised the desired Cu_3BiS_3 phase. As before, those films having composition ratios of 9:4, 18:7 and 3:1 appeared to be phase pure. However, it is clear that if the composition strays beyond 9:4, close to 2:1, then major compositional changes will take place. Hence it was realised that the processing window at 375°C was more tolerant to compositional variation than at 400°C.

The SEM images of these films shown in Figure 5.5c) and d) are typical for compositions of Cu:Bi 3:1 and show that the surface morphologies are similar to those of the films processed at 375°C. Grain size was estimated as shown in Figure 5.6 and Table 5.2, giving an increase from ~800 nm in the films sulfurised at 375°C to ~1000 nm in those sulfurised at 400°C.

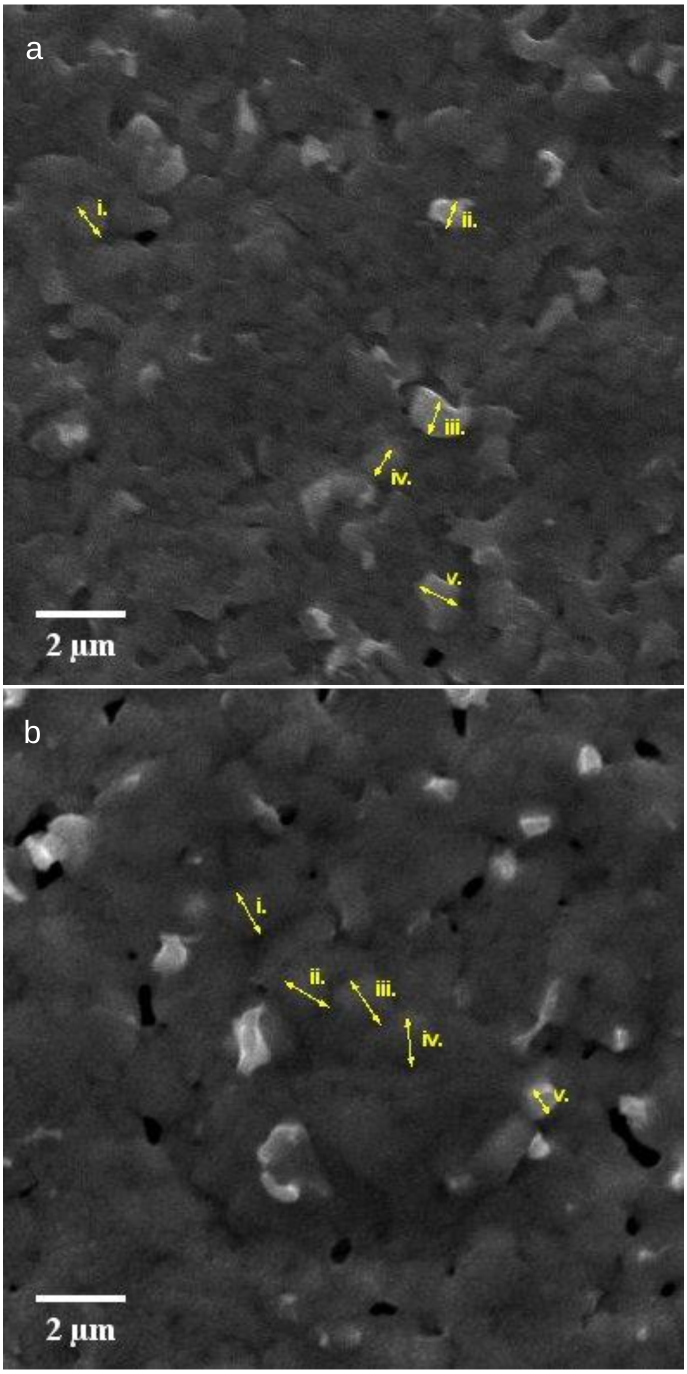

Figure 5.6: SEM micrographs of 3:1 Cu:Bi ratio Cu_3BiS_3 films sulfurised at (a) 375°C and (b) 400°C. The grains annotated on each were used to estimate the average grain size in the films.

Table 5.2: Sizes of grains indicated in Figure 5.6 and average of these values used to estimate the average grain size in films sulfurised at 375 and 400°C.

	Grain Size (nm)	
Grain	375°C	400°C
i	833	1001
ii	642	1067
iii	835	1063
iv	711	1018
v	850	627
Average	774.2	955.2

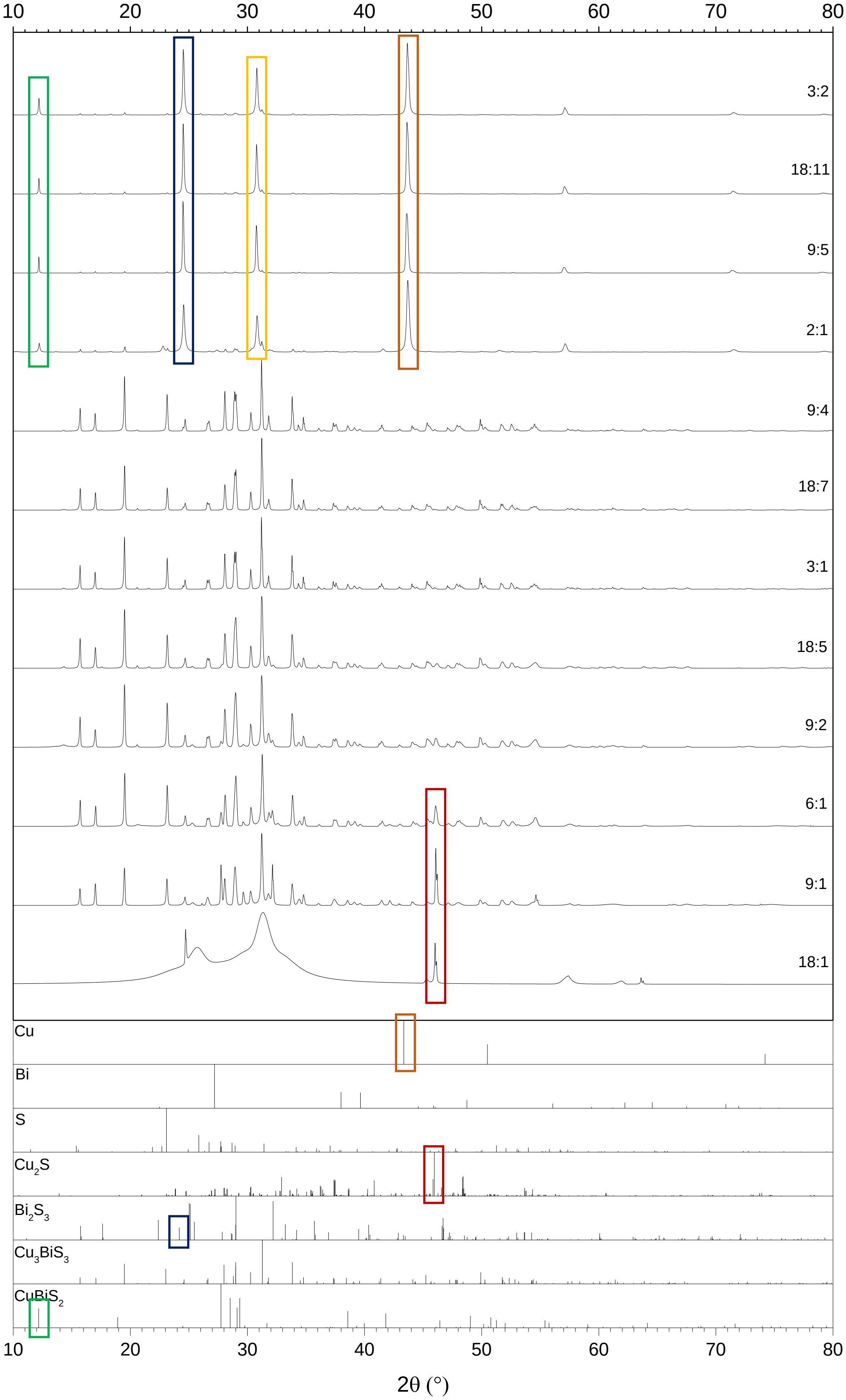

Figure 5.7: XRD spectra of Cu-Bi stacks sulfurised at 400°C with reference spectra for the target phase. Cu_3BiS_3, and other possible ternary, binary and elemental impurity phases. The Cu:Bi atomic ratio of the precursor films is indicated for each experimental XRD pattern. There is a smaller window of successful growth of low impurity films than seen in the 375°C analogue consisting of the four samples in the Cu:Bi range 9:4-18:5.

The final set of XRD patterns, for films sulfurised at 425°C is shown in Figure 5.8. For these films the thermal loss of material made it difficult to acquire noise-free XRD spectra, but those shown in the figure are fully adequate for phase analysis. Similar to the cases for sulfurisation at 375 and 400°C, the extreme Cu- and Bi-rich compositions gave mixed phases that did not include the target phase of Cu_3BiS_3. Again, it was the compositions near to the ideal composition that gave the most phase pure Cu_3BiS_3 material, for this temperature 18:7 giving the only spectrum with no evidence of secondary phases. Hence the trend of a narrowing material composition processing window with increasing temperature was seen to continue at 425°C. For this sample set the SEM micrographs shown in Figure 5.5e) and f) show a significant increase in the density of pinholes and void defects, this being consistent with the breakdown in film integrity shown in the photographs in Figure 5.1.

As mentioned earlier the thermal loss of material associated with processing at 450°C became extreme and these films could not be characterised.

Overall it was shown that although a wide range of temperatures could be used for the sulfurisation of Cu-Bi bilayers for the formation of Cu_3biS_3, the selection of 375°C gives the widest tolerance to the composition of the precursor films. Hence further work on alternative substrates for device making was conducted at this temperature, as reported in Section 5.3.2.

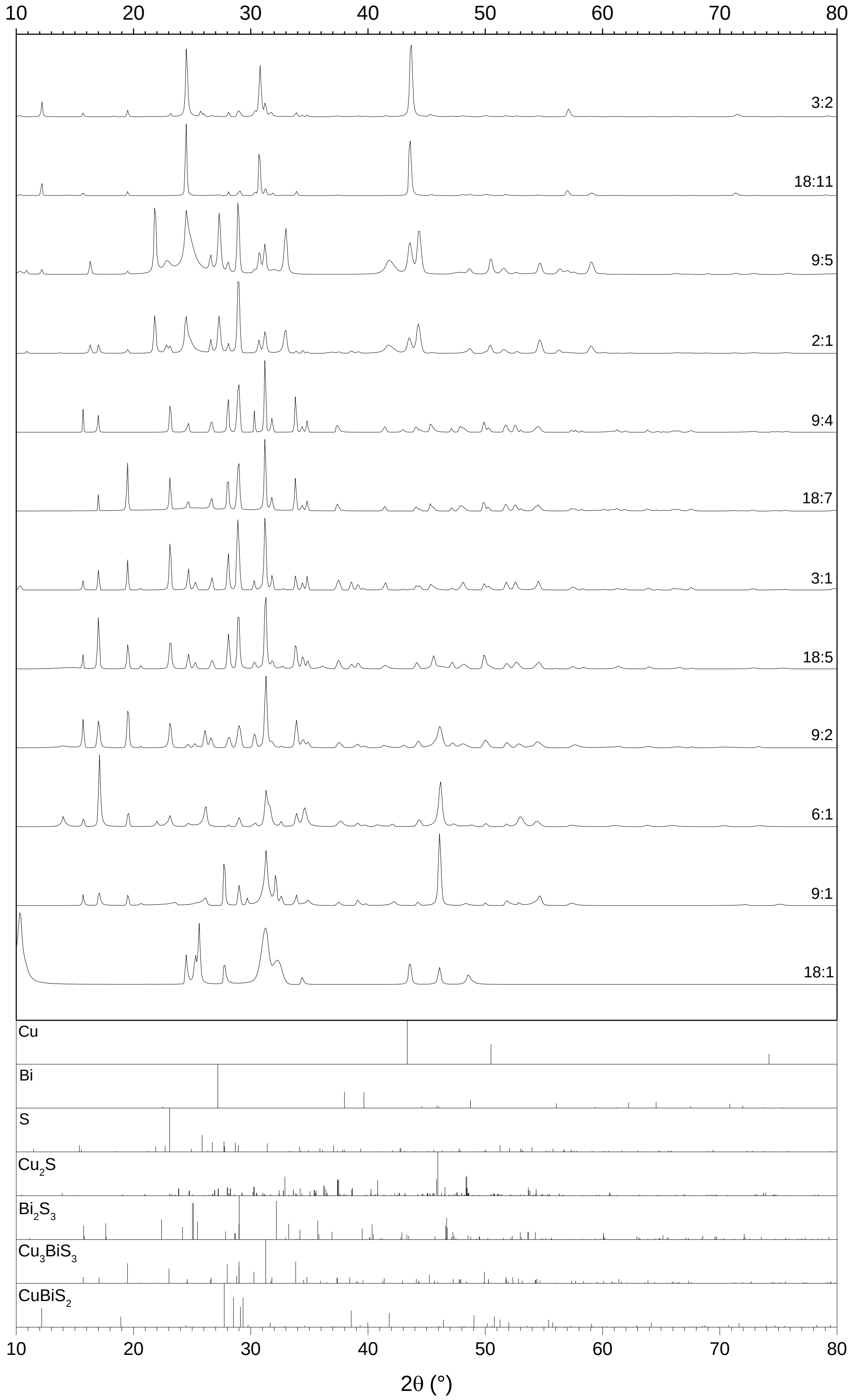

Figure 5.8: XRD spectra of Cu-Bi stacks sulfurised at 425°C with reference spectra for the target phase. Cu_3BiS_3, and other possible ternary, binary and elemental impurity phases. The Cu:Bi atomic ratio of the precursor films is indicated for each experimental XRD pattern. At this temperature only the 18:7 Cu:Bi ratio film was free of secondary phases.

Tauc plots for the films sulfurised at 375 and 400°C are shown in Figure 5.9. In these figures the full range of exponents, 2, ½, ⅔ and ⅓ for the y-axis term $(\alpha hv)^r$ as explained in Chapter 4 has been tested. It may be seen from the plots that none of them show a convincing linear section that could be used in order to make an extrapolation for the estimation of band gap values however the best estimate for each case is shown in Table 5.3#. Hence in this case the Tauc plot method has been unable to discriminate between the four cases of direct allowed, indirect allowed, direct forbidden and indirect forbidden band gap types. This is discussed further in Section 5.5. For the plots in Figures 5.9a and b for direct allowed and indirect allowed transitions, it may be seen that the plots leave the x-axis at ~ 1.5 and ~1.0 eV respectively. Although it is tempting to attribute this difference to a complex multiple band behaviour in this material, the evidence is for it here is weak. This is discussed further in Section 5.8.

Table 5.3: Best estimates of the energy for each of the potential optical transitions explored in the Tauc plots in Figure 5.9.

Direct		Indirect	
Allowed	Forbidden	Allowed	Forbidden
1.68 eV	1.45 eV	1.36 eV	1.20 eV

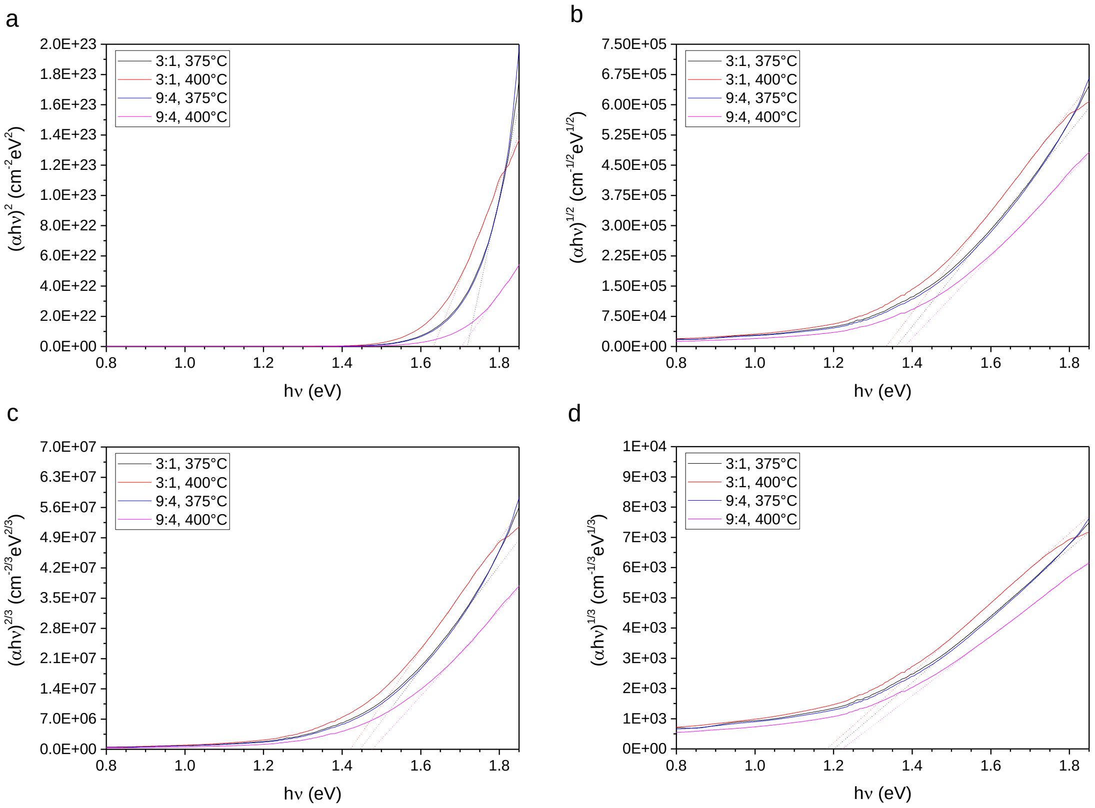

Figure 5.9: Tauc plots for films of atomic Cu:Bi ratio of 3:1 and 9:4 sulfurised at 375°C and 400°C plotted as (a) direct allowed, (b) indirect allowed, (c) direct forbidden, and (d) indirect forbidden band gaps. Solid lines represent the optical data and dashed lines the extrapolation of the best estimate to the linear portions of each curve.

5.3.2 Formation of Cu_3BiS_3 films on Mo

The growth of Cu_3BiS_3 on sputtered Mo substrates was explored since films grown on them may be incorporated into substrate device structures. The conditions for sulfurisation were similar to the optimum from the trials on glass (i.e. 375°C, 500 mg sulfur, 300 mTorr and 30 minutes). Two thickness ratios were used in this section: 3:2 (Cu:Bi 9:4) and 1:1 (Cu:Bu 3:1)

Films produced by this method were visually very similar to those on glass: brown/grey in colour and uniformly adherent to the substrate. However SEM micrographs (Figure 5.10) reveal more severe pinholes than in the case of those films deposited onto plain glass substrates but larger grains with a minimum size of approximately 1.1 µm compared to 750 nm for those sulfurised at 375°C on glass.

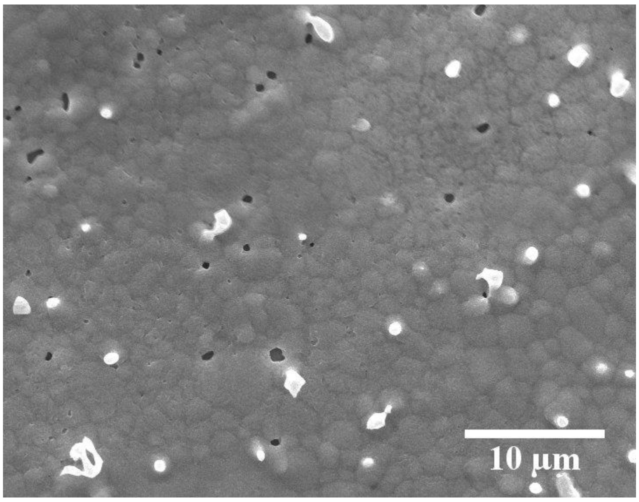

Figure 5.10: SEM micrograph of a 9:4 atomic Cu:Bi precursor ratio film on a Mo substrate, sulfurised at 375°C. The bright contrast grains are charge artefacts on the surface.

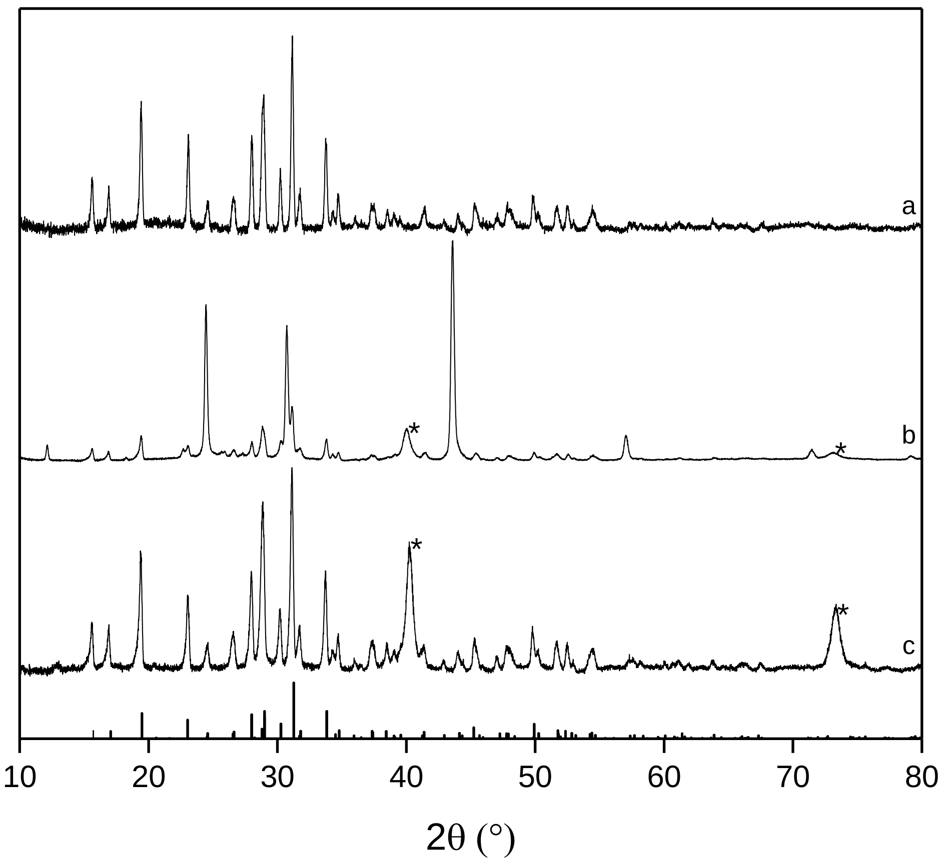

Figure 5.11: XRD spectra of Cu-Bi-S films with sulfurised from (a) Cu:Bi 9:4 on glass, (b) Cu:Bi 9:4 on Mo and (c) Cu:Bi 3:1 on Mo. Peaks marked belong to the Mo layer. Cu_3BiS_3 reference peaks are shown on underneath.

Figure 5.11 shows the XRD spectra for typical films sulfurised from slightly Bi-rich (Cu:Bi 9:4) precursor stacks on glass (a) and Mo (b) in addition to stoichiometric (3:1 Cu:Bi) precursor stacks (c) on Mo. Inspection of these spectra shows the presence of phase pure Cu_3BiS_3 in the case of the film grown on glass as before. The film grown on the Mo substrate using the slightly Bi-rich precursor stacks shows, in addition to the Cu_3BiS_3 peaks and those belonging to the substrate (denoted by asterisks), peaks at 12.2° and 43.6° peak which were both observed in Bi-rich films as seen in Figures 5.5 and 5.6. The 12.2° peak is attributed again to the presence of $CuBiS_2$ and the phases considered for the 43.6° peak are discussed in Table 5.4. Since the 43.6° peak has been observed in films grown in systems with no Mo, MoS_2 is excluded as a candidate. The high index peaks of Bi_2S_3, $Cu_4Bi_4S_9$ and $Cu_8Bi_{12}S_{22}$ are unlikely and hence also excluded. The remaining candidate phase is elemental Cu, the likelihood of its occurrence is explored in Section 5.5. The impurity phase introduced by growth on Mo is prevalent in Bi-rich films in the Cu-Bi-S system on glass, films for further study were grown with reduced Bi content (3:1 Cu:Bi). The XRD spectrum shown in Figure 5.11c is for a typical film grown under the best conditions tested.

Table 5.4: Possible candidates for the XRD peak at 43.6° observed in Cu_3BiS_3 films on Mo sulfurised at 375°C from precursor stacks with Cu:Bi atomic ratio 9:4. The XRD data were from the American Mineralogist Crystal Structure Database[7].

Substance	2θ	Powder Intensity	h	k	l	Notes
Cu	43.35	100.00	1	1	1	Likely
Bi_2S_3	43.53	8.13	2	0	5	Unlikely
MoS_2	43.33	5.20	0	0	6	Excluded
$Cu_4Bi_4S_9$	43.39	16.63	7	4	1	Unlikely
$Cu_8Bi_{12}S_{22}$	43.58	4.60	-1	1	11	Unlikely

5.3.3 Selenisation

Single layers of Cu and Bi were selenised individually for comparison with those films grown with Cu/Bi bilayers. Table 5.4 shows the temperatures and durations of selenisation runs. All trials were undertaken using 100 mg elemental Se and a background N_2 pressure of 300 Torr.

Table 5.4: Selenisation conditions for the Cu-Bi-Se films grown. In all cases 100 mg of elemental Se and a background N_2 pressure of 300 Torr were used.

Temperature (°C)	Time (minutes)
350	60
400	30
400	45
400	60
450	60
450	30

XRD spectra from those films selenised at 400°C for 30 minutes was taken and the data from these films are shown in Figure 5.12 alongside the reference spectra for the elements, binaries and ternaries. Inspection of these spectra verified that Cu_2Se could be formed easily. The growth of Bi_2Se_3, however, was not as successful, the spectrum taken from the Bi-Se sample being comprised of both Bi_2Se_3 and Se. The Cu-Bi-Se sample interrogated had prevalent Cu_2Se peaks corresponding to 111 (26.8°) and 220 (44.5°); the remaining peaks in this spectrum are troublesome to identify, some appearing to be from the Bi_2Se_3 phase while others are not identifiable by comparison with any of the elements, binaries or any of the reported ternary Cu-Bi-Se phases. Across all conditions selenised films had a severely corroded appearance and in none of the cases was there enough material remaining to warrant extensive analysis.

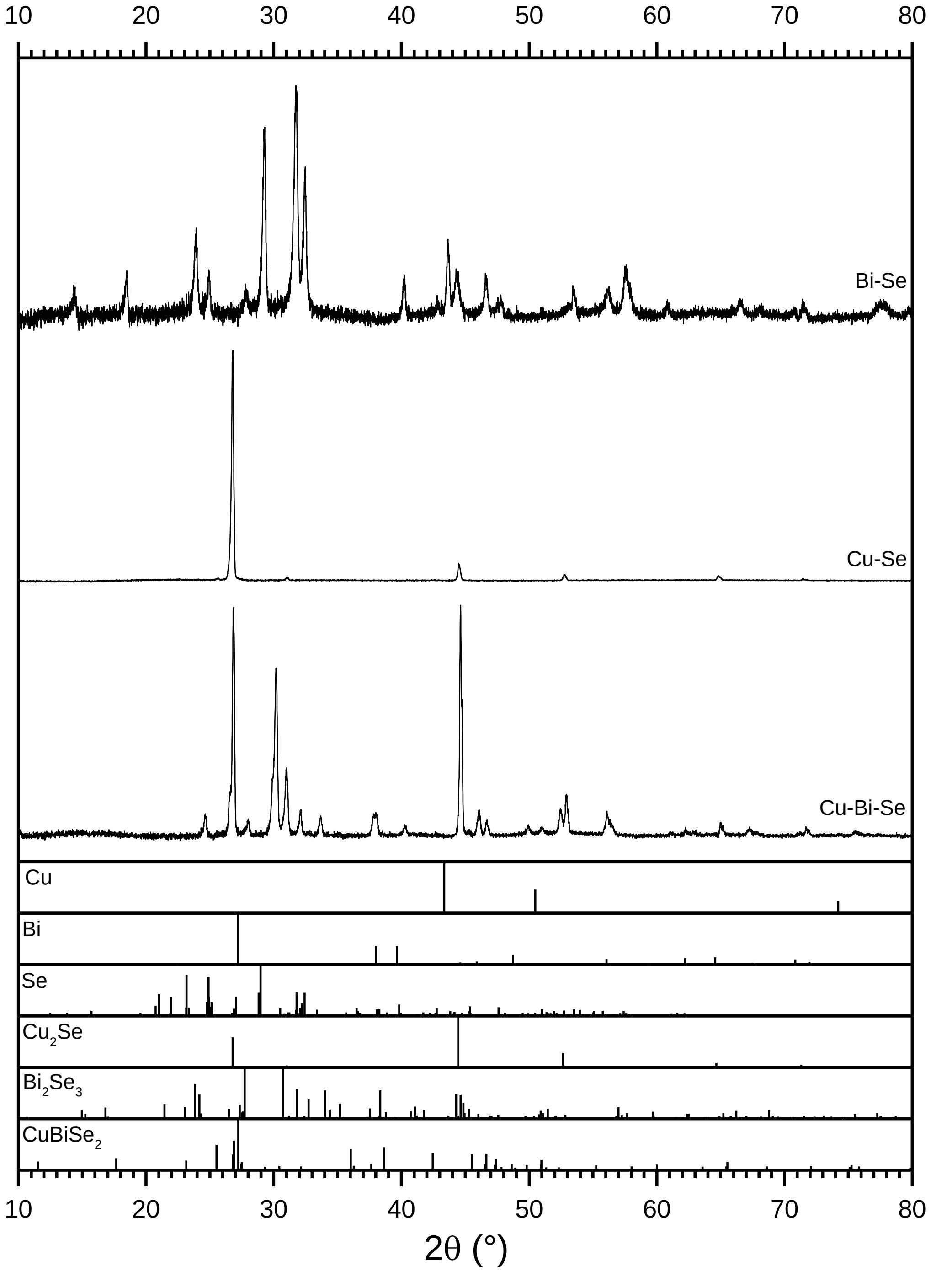

Figure 5.12: XRD spectra of selenised Cu, Bi, and Cu-Bi films. Reference spectra for the elemental constituents, the binary compounds and a potential ternary phase are also shown.

5.4 Cu_3BiS_3 device structures and characterisation

The window layers of choice in this study were CdS and ZnS. Figure 5.13 shows band offsets for these systems.

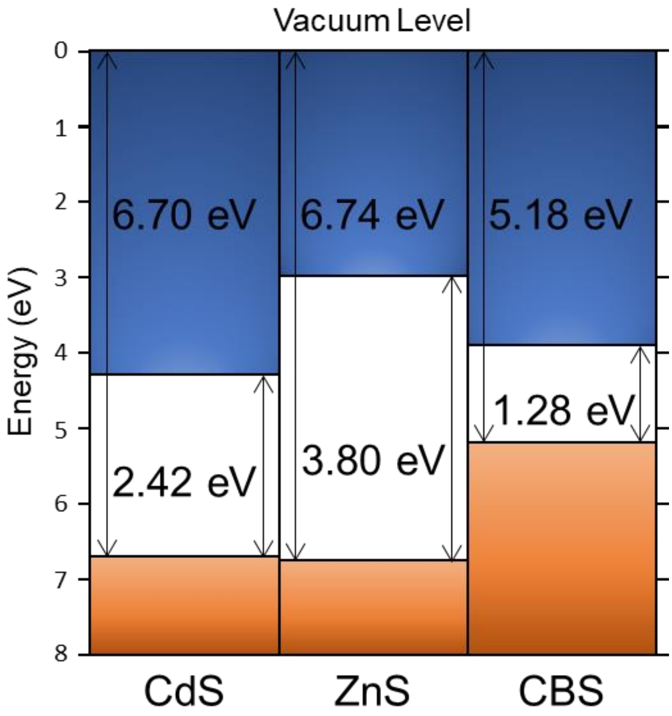

Figure 5.13: Band line-up for Cu_3BiS_3[5], CdS[8], and ZnS[9].

Layers of Cu_3BiS_3 were deposited into molybdenum coated glass using the optimised conditions from Section 5.3.2 and layers of CdS or ZnS were grown on top by sputtering as described in Section 5.2.5 followed by the ITO layer. The completed devices were scribed using a razor blade into 9 cells of size approximately 0.25 cm^2.

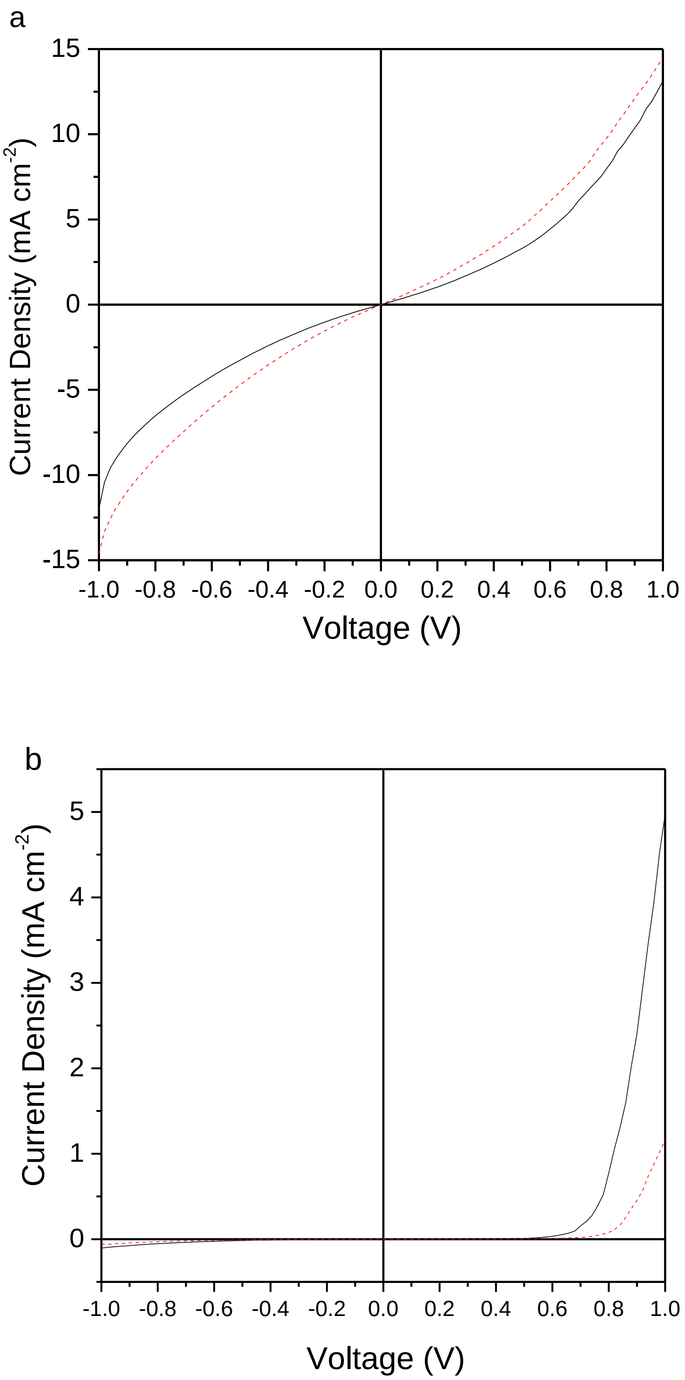

Figure 5.14: *J-V* responses of (a) glass/Mo/Cu_3BiS_3/CdS/ITO and (b) glass/Mo/Cu_3BiS_3/ZnS/ITO devices under AM1.5 illumination (solid line) and in the dark (dashed line).

The devices made were not photoactive as shown in the current-voltage data shown in Figure 5.14 and therefore no signal was obtained from the EQE scans attempted.

5.5 Discussion

Growth of Cu_3BiS_3 was demonstrated by the sulfurisation of metal layers, and the impact of precursor composition on the resulting phases in sulfurised films established. XRD of sulfurised films indicate that the intended phase may be successfully made with no evidence of secondary phases. In copper-rich precursor films Cu_2S peaks are observed in addition to the Cu_3BiS_3 peaks across all sulfurisation temperatures. At the lowest temperature investigated, 375°C, growing bismuth rich films also promotes growth of the binary, Bi_2S_3, in addition to the desired ternary phase. An undesired ternary phase, $CuBiS_2$, also begins to form. At higher temperatures the situation with bismuth rich films is more complicated; the $CuBiS_2$ phase and Bi_2S_3 phases are generated along with a phase which appears at $2\theta = 43.35°$. The main candidates for this are $Cu_4Bi_4S_9$ and unconverted Cu (111). The $Cu_4Bi_4S_9$ peak is a high index and there are no others that could be assigned to that phase, while for elemental Cu the (111) peak is the highest intensity. The peak is, therefore, more likely to be elemental Cu.

The appearance of elemental Cu alongside Bi_2S_3 in films created from bismuth-rich Cu-Bi films is unexpected and possible reasons for its appearance are now discussed. Table 5.6 shows the Gibbs free energy of formation of each of the important binaries in this system. The values of free energy are calculated for

400°C since this is the lowest temperature at which the 2θ = 43.35° peak was observed on glass.

Table 5.6: Calculations for the Gibbs free energy for the formation of each of the binary compounds covered in Equations 5.1 and 5.2.

Substance	ΔH^0 kJ mol^{-1}	S^0 J K^{-1} mol^{-1}	ΔG (400°C) kJ mol^{-1}
Bi_2S_3	-201.7	200.4	-341.6
Cu_2S	-79.9	120.9	-161.3
CuS	-52.3	66.5	-97.1

Equations 5.1 and 5.2 are considered here in order to understand the phases that exist in this system if it is at equilibrium.

$$6Cu + Bi_2S_3 \rightleftharpoons 3Cu_2S + 2Bi \ (\Delta G = -142.3) \qquad \text{Equation 5.1}$$

or

$$3Cu + Bi_2S_3 \rightleftharpoons 3CuS + 2Bi \ (\Delta G = +50.3) \qquad \text{Equation 5.2}$$

At 400°C Equation 5.1 has a Gibbs free energy change of -142.3 kJ mol^{-1} and therefore proceeds left to right whereas Equation 5.2 has a change of +50.3 kJ mol^{-1}, proceeding right to left. It is therefore important to know which of the Cu binaries are energetically favoured and Equation 5.3 is considered.

$$2CuS \rightleftharpoons Cu_2S + S \ (\Delta G = -32.9) \qquad \text{Equation 5.3}$$

Equation 5.3 has a Gibbs free energy change of -32.9 kJ mol^{-1} indicating that, provided the system is in equilibrium, the reaction in Equation 5.3 will proceed from left to right and CuS will be produced, therefore the equilibrium of CuS with Bi_2S_3 is considered (Equation 5.2). The Cu binary equilibrium creates CuS over Cu_2S which is then converted to Cu and Bi_2S_3 in the presence of Bi, allowing Equation 5.3 to proceed further. Therefore, in equilibrium, elemental Cu and

Bi_2S_3 are present in concordance with the experimental data. While this does explain the observations, it does not take into account any ternary phases present – such as the $CuBiS_2$ which is observed alongside the Bi_2S_3 and Cu in Figure 5.7 – so the ternary phase diagram from Figure 3.2 is consulted.

Inspection of the Cu-Bi-S phase diagram reveals that there is no tie line between Bi_2S_3 and Cu and hence they cannot exist in equilibrium without a third phase being present. Although $CuBiS_2$ is observed in the films alongside the Bi_2S_3 and Cu, there are no zones in the phase diagram in which these three phases can exist in equilibrium together and thus an alternative explanation must be sought.

The geometry of the sample is the next consideration for the understanding of what may be an incomplete reaction. In the precursor stacks the Bi is the top layer and therefore during the sulfurisation process Bi_2S_3 will form at the top surface. As the elemental sulfur penetrates the layer the reaction will propagate through the Bi layer in the precursor stack. The ternary will then be formed either via the reaction of the Bi_2S_3 with the metallic Cu, or by the reaction of S with the Cu and subsequent reaction of the binaries. The data suggest that the Bi fully reacts into Bi_2S_3 and begins to react with the Cu, in this case forming the $CuBiS_2$ ternary phase, but then the reaction stops when the sample is cooled to room temperature.

When the film is grown on sputtered Mo films the $2\theta = 43.35°$ peak (i.e. the peak due to Cu) is present at a higher Cu:Bi ratio (9:4 versus 2:1) and lower temperature (375°C versus 400°C) than on glass. It may, therefore, be inferred that the Mo substrate has had an effect on the presence of the Cu (111). The

Mo substrate may influence the nucleation and thus morphology of the deposited Cu and Bi films causing altered sulfurisation behaviour or it could affect the heat profile of the layers during the sulfurisation process and hence change the process itself. The layers grown with reduced bismuth (i.e. Cu:Bi of 3:1 rather than 9:4) content did not display this XRD peak. Hence films on Mo for the fabrication of full device structures were grown using Cu:Bi of 3:1 and were sullfurised at 375°C.

Considering the optical data presented in Figure 5.9, comparison with theory is helpful. Kehoe and Kumar both report theoretical values for the direct and indirect band gaps of Cu_3BiS_3. Kehoe reports these as 1.76 eV and 1.69 eV respectively[10] while Kumar's value of the direct band gap differs slightly (1.79 eV) but the indirect is the same[11]. The Tauc methodology of plotting $(\alpha h\nu)^r$ vs $h\nu$ to test the type of optical transition was employed for these Cu_3BiS_3 films and is shown in Figure 5.8. None of the plots, however, had straight line sections and thus inference of transition type was not possible. The lack of linear regions in the Tauc plots may be attributed to the mixed direct/indirect nature of the optical transition of the Cu_3BiS_3. Alternatively, it may be due to the quality of the optical data collected. Although α was estimated by taking into account both transmission and reflectance, the reflectance was measured using a system that collected only the specular component. Loss of intensity due to scattering rather than true absorption could lead to errors.

The device structures made with a CdS window layer showed s-shaped *J-V* responses as seen in Figure 5.14. Since the CdS was deposited at 200°C at a pressure of 5 mTorr the Cu_3BiS_3 film may experience material loss during the deposition, potentially opening up shunting pathways in the Cu_3BiS_3 layer.

Alternatively, there could be an electronic reason for the low performance. The band line-up shown in Figure 5.13 indicates the presence of a large conduction band offset of ~ -0.38 eV. Offsets of this magnitude have been identified as causes for poor efficiency in photovoltaic devices due to increased interface recombination[12–14].

In those cells with ZnS as a window layer the J-V response is diode-like indicating the presence of a junction, however, photocurrent is not generated. The ZnS layer was sputtered at room temperature and has a more favourable conduction band offset with Cu_3BiS_3 than CdS negating both issues considered with the CdS layer. The lack of photocurrent here is not explained by either of these issues and is considered further in Section 8.2.1.

Of the other authors who have presented device structures, only one other shows data for the current-voltage response of Cu_3BiS_3 devices[15]. This device has an efficiency of 0.11%, J_{sc} of 3.7 $mA \cdot cm^{-2}$, and a V_{oc} of 89 mV. The EQE presented has a peak value of below 6% and the absorption peaks at approximately 500 nm, tailing off rapidly indicating that the majority of the response seen from the device is from the CdS partner layer used. Despite the device's non-zero efficiency, the fact that the photocurrent is likely to be from the CdS layer is in agreement with the lack thereof observed in this work and, it might be speculated, the absence of reported current-voltage measurements in the Mesa publication[3].

5.6 Conclusions

The growth of Cu_3BiS_3 was investigated by the post-deposition annealing of Bi/Cu bilayers.

Films of Cu-Bi-S grown on glass had a broad range of Cu:Bi ratios which successfully sulfurised to the Cu_3BiS_3 phase at 375°C. The desired phase was also produced in films sulfurised at 400 and 425°C albeit with reducing “precursor film” ratio tolerance as temperature increased. Films sulfurised at 450°C exhibited extreme material loss.

Bi-rich films on glass formed films composed of Bi_2S_3, elemental Cu and $CuBiS_2$ when sulfurised using temperatures of 400°C and above. The presence of elemental Cu was observed in Cu-Bi-S films grown on Mo at 375°C at lower a Cu:Bi ratio than on glass which may be due to the impact of the Mo layer on the heat profile of the precursor films during the sulfurisation step.

The growth of the selenium analogue, Cu_3BiS_3, was attempted by the selenisation of Bi/Cu bilayers. This technique resulted in poor quality films consisting primarily of the binary compounds in the system. These films were, therefore, not suitable for optical characterisation or device incorporation

Phase pure Cu_3BiS_3 grown on Mo was incorporated into device structures with CdS and ZnS used as window layers. Those with CdS window layers exhibited s-shaped J-V responses while those with ZnS had diode-like responses. Neither device structure displayed any photocurrent. This result was similar to the findings of Hernádez-Mota[15].

The absence of any working Cu_3BiS_3 cells reported considering the volume of literature on this material is not promising for its prospects as a photovoltaic absorber.

References for Chapter 5

1. Peccerillo, E. & Durose, K. Copper–antimony and copper–bismuth chalcogenides—Research opportunities and review for solar photovoltaics. *MRS Energy Sustain.* **5**, (2018).

2. Yin, J. & Jia, J. Synthesis of Cu_3BiS_3 nanosheet films on TiO_2 nanorod arrays by a solvothermal route and their photoelectrochemical characteristics. *CrystEngComm* **16**, 2795 (2014).

3. Mesa, F., Dussan, A., Sandino, J. & Lichte, H. Characterization of Al/Cu_3BiS_3/buffer/ZnO solar cells structure by TEM. *J. Nanoparticle Res.* **14**, (2012).

4. Whittles, T. J. Electronic Characterisation of Earth-Abundant Sulphide for Solar Photovoltaics. (PhD thesis, University of Liverpool, 2017).

5. Whittles, T. J., Veal, T. D., Savory, C. N., Yates, P. J., Murgatroyd, P. A. E., Gibbon, J. T., Birkett, M., Potter, R. J., Major, J. D., Durose, K., Scanlon, D. O. & Dhanak, V. R. Band Alignments , Band Gap , Core-levels and Valence-Band States in Cu3BiS3 for Photovoltaics. *Manuscr. Prep.*

6. Claybourn, M., Brinkman, A. W., Russell, G. J. & Woods, J. Electron traps in single-crystal CdS. *Philos. Mag. B* **56**, 385–395 (1987).

7. American Mineralogist Crystal Structure Database. Available at: http://rruff.geo.arizona.edu/AMS/amcsd.php.

8. Burton, L. A. & Walsh, A. Band alignment in SnS thin-film solar cells: Possible origin of the low conversion efficiency. *Appl. Phys. Lett.* **102**, 6–9 (2013).

9. Klein, A. Energy band alignment in chalcogenide thin film solar cells from photoelectron spectroscopy. *J. Phys. Condens. Matter* **27**, (2015).

10. Kehoe, A. B., Temple, D. J., Watson, G. W. & Scanlon, D. O. Cu_3MCh_3 (M = Sb, Bi; Ch = S, Se) as candidate solar cell absorbers: insights from theory. *Phys. Chem. Chem. Phys.* **15**, 15477 (2013).

11. Kumar, M. & Persson, C. Cu_3BiS_3 as a potential photovoltaic absorber with high optical efficiency. *Appl. Phys. Lett.* **102**, 1–5 (2013).

12. Minemoto, T., Matsui, T., Takakura, H., Hamakawa, Y., Negami, T., Hashimoto, Y., Uenoyama, T. & Kitagawa, M. Theoretical analysis of the effect of conduction band offset of window/CIS layers on performance of CIS solar cells using device simulation. *Sol. Energy Mater. Sol. Cells* **67**, 83–88 (2001).

13. Nagoya, A., Asahi, R. & Kresse, G. First-principles study of Cu_2ZnSnS_4 and the related band offsets for photovoltaic applications. *J. Phys. Condens. Matter* **23**, (2011).

14. Sinsermsuksakul, P., Hartman, K., Bok Kim, S., Heo, J., Sun, L., Hejin Park, H., Chakraborty, R., Buonassisi, T. & Gordon, R. G. Enhancing the efficiency of SnS solar cells via band-offset engineering with a zinc oxysulfide buffer layer. *Appl. Phys. Lett.* **102**, (2013).

15. Hernádez-Mota, J., Espíndola-Rodríguez, M., Sánchez, Y., López, I., Peña, Y. & Saucedo, E. Thin film photovoltaic devices prepared with Cu_3BiS_3 ternary compound. *Mater. Sci. Semicond. Process.* **87**, 37–43 (2018).

6. Growth of Sb_2Se_3 films

6.1 Introduction

As described in the review in Chapter 3, Sb_2Se_3 possesses the materials properties desirable for PV, these being a near-ideal band gap (1.55 eV), high absorption (>10^5 cm^{-1}) and having constituent elements that are relatively abundant and non-toxic. Since it is a binary compound, phase control is more trivial than in the case of ternary (e.g. Cu_3BiS_3, as seen in Chapter 5) or quaternary (e.g CIGS, CZTS) compounds. A significant potential advantage of this material is that its structure comprises covalently bonded chains that are connected by van der Waals forces. Therefore, in principle, films oriented in the chain direction may contain grain boundaries that are van der Waals bonded and hence may be electrically benign. Hence if it is possible to grow highly oriented films it may be possible to unlock the full potential of the material over conventional diamond-like absorber materials. Wang [1] reports that the texture of Sb_2Se_3 on ZnO can be influenced by the orientation of the ZnO layer. In that work, randomly oriented ZnO encouraged Sb_2Se_3 films which were predominantly (221) oriented, and for which the covalent chains of Sb_2Se_3 are inclined, but not perpendicular to the substrate. Hence the opportunity remains to study the growth of Sb_2Se_3 in order to attempt to influence the crystal texture by adjusting the growth conditions with a view to optimising the benefit for device operation.

In metallurgy the Structure Zone Model (SZM) describes the relationship between the grain structure of a metallic film and the substrate temperature during its growth. This model separates the grain structure types into three categories each driven by different processes during the growth of the film. The relative dominance of each of the processes are governed by the temperature (T) of the system as a function of the melting point (T_M) of the material being deposited. The main three processes to consider are: shadowing, surface diffusion, and bulk diffusion.

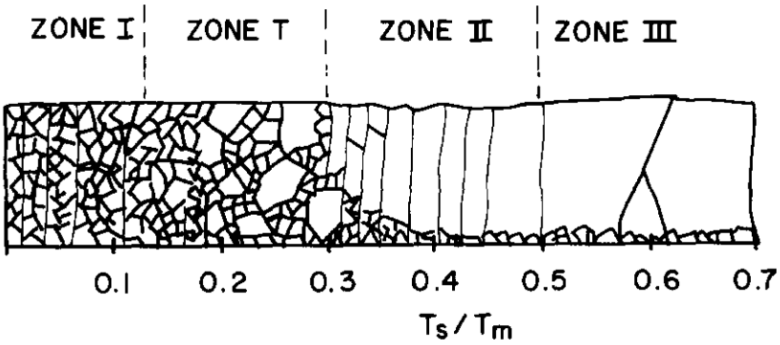

Figure 6.1: Grain structure in each zone according to the Structure Zone Model. Replicated from Grovenor *et al.*[2].

In Zone I ($0.3 > T/T_M$) shadowing processes dominate (i.e. high points on the surface receive higher adatom flux than low points) and there is not sufficient thermal energy to allow surface diffusion. The result of growth in Zone I is tapered crystals with domed tops having high dislocation density and voids at the grain boundaries. Zone II ($0.3 < T/T_M < 0.5$) has ample thermal energy to allow surface diffusion to dominate. Grains are columnar and have diameters that increase with temperature, this being consistent with the activation energy of the surface diffusion process. In Zone III ($0.5 < T/T_M$) the diameter of the grains is greater than the thickness and increases with T/T_M corresponding to an activation energy belonging to bulk diffusion[2]. The final zone indicated in

Figure 6.1 is Zone T, and this was proposed by Thornton as the regime existing as a transition between Zone I and Zone II occurring as the surface diffusion process beings to overcome the shadowing effects. This has lower activation energy and thus occurs at lower T/T_M as the substrate roughness decreases[3].

Control of the growth of Sb_2Se_3 into needle-like structures (Zone 1) is desirable due to its ribbon-like structure. However, metallic films grown in Zone I (below ~$0.3T_m$) often contain voids between grains – such a structure would be highly undesirable for any photovoltaic devices. In Zone II ($0.3T_m < T <$ and $0.5T_m$) however, columnar grains form which increase in width with the growth temperature into Zone III as temperature exceeds $0.5T_m$. With the melting point of Sb_2Se_3 being 611°C, Zone I would occur below -8°C, Zone II between -8 and 170°C, and Zone III above 170°C. However, since the bonding in Sb_2Se_3 is strongly anisotropic, its conformity to the Structure Zone Model is open to question.

In this chapter Sb_2Se_3 layer growth was therefore investigated for deeper understanding of the material with a view to incorporating it into devices. Sb_2Se_3 was grown by thermal evaporation and effect of substrate temperature on the crystal texture was investigated. Also, the effect of substrate type was tested with growth onto the following substrates: soda-lime glass, RF sputtered CdS, and n-type InP (100) wafers. The crystal texture of the films was monitored by XRD for the as-grown and heat-treated films and their optical properties measured via UV-vis-NIR spectroscopy.

6.2 Experimental

6.2.1 Film growth of Sb_2Se_3

a) Substrates

The substrates used in this work were:

i) Plain soda-lime glass

Glass substrates (Optiwhite, NSG Ltd.) were prepared as described in Section 5.2.1.a.i

ii) RF sputtered CdS

50 nm of CdS was deposited by RF magnetron sputtering onto TEC15 glass (NSG Ltd), cleaned as above from a 99.99% pure 2” target (Pi-KEM) in an AJA Orion chamber. Sputtering took place under Ar at 3 mTorr for 30 minutes at a power of 50 W with the substrate temperature being 200°C.

iii) N-type InP (100) wafers

InP wafers were purchased from Wafer Technology Ltd and were n-type, S doped, 2” diameter, having (100) orientation, and 10^{17} cm^{-3} carrier concentration. Wafers were removed from individually sealed packaging and immediately transferred into the vacuum chamber for deposition.

b) Sb_2Se_3 film growth conditions

Sb_2Se_3 films were grown by thermal evaporation from the 99.999% pure compound (Alfa Aesar) from a carbon crucible in a Moorfield MiniLab 080 thermal evaporator at a rate of 0.3 Å/s as monitored by an in-situ quartz crystal monitor. Where films where grown at an elevated substrate temperature, the substrates were maintained at the growth temperature for 20 minutes prior to deposition in order to reach equilibrium. The Sb_2Se_3 was deposited at temperatures between ambient and 550°C, making Zones II and III accessible in these experiments. Within Zone II substrate temperatures of 24 and 150°C were chosen. In Zone III temperatures between 250 and 550°C in 100°C intervals were trialled with an additional deposition at 500°C being also included.

c) Post-growth annealing steps

Since this work and the device studies presented in the next chapter were performed concurrently, the annealing temperatures chosen here were centred on 350°C which produced the highest efficiency devices. Annealing of films was carried out in two different ways:

i) Annealing in a box furnace

Samples were placed in the centre of a box furnace (MTI KSL1100X) and flushed with dry nitrogen. The samples were heated to 350°C while maintaining the nitrogen flow, held at temperature for 30 minutes and allowed to cool naturally under the same flow.

ii) Hotplate annealing in a glovebox

The annealing process in the glovebox involved placing samples onto a pre-heated hotplate under dry nitrogen and removing them after the desired length of time. Annealing temperatures used for various substrates are reported along with the results.

6.2.2 Characterisation of Sb_2Se_3 films

Characterisation was by XRD and UV-vis-IR spectroscopy. XRD spectra were taken in the range $15 < 2\theta < 80°$ on a Rigaku SmartLab X-ray diffractometer. Texture analyses on these data were performed as described by Kim.[4] Transmission and specular reflectance were measured from samples deposited on glass using a Shimadzu SolidSpec-3700 UV-Vis-NIR spectrophotometer.

6.3 Results

6.3.1 As-grown evaporated Sb_2Se_3 films on glass

Figure 6.2 shows the θ - 2θ XRD patterns for the set of as-grown evaporated films of Sb_2Se_3 grown on glass at substrate temperatures in the range 24 – 550°C. There is a clear trend in that films deposited at ≤ 450°C all show diffuse XRD intensity indicating that the material is amorphous. Only at 500°C and above do clear Bragg peaks emerge, indicating that the material has become polycrystalline.

The XRD patterns and the data in Figure 6.2 and Table 6.3 both demonstrate that the film grown on glass substrates held at 500°C has a strong preferred (020) orientation whereas the 550°C film contains more peaks and is more random. For the layer deposited at 500°C, the (020) peak at 15.05° is exceptionally strong giving it a texture coefficient of 13.35, this being very much greater than for the other peaks in the spectrum. The standard deviation of the texture coefficient values is correspondingly large, at 3.06. Hence growth of the (020) planes is very much favoured at this temperature, and the covalently bonded ribbons lie parallel to the surface of the film and hence the substrate. On the contrary, in the case of the 550°C film there are more peaks present. Of these a larger number have texture coefficients approaching unity with none being greater than 3.66. The standard deviation of the texture coefficients is 0.93 for the 550°C film, confirming that the films are much more random at 550 than at 500°C.

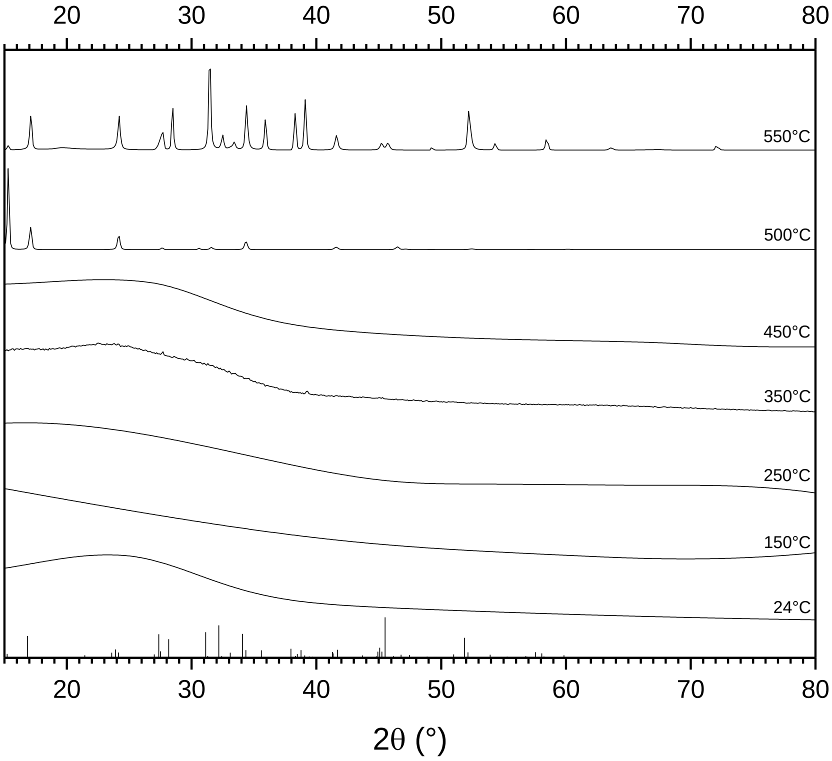

Figure 6.2: XRD spectra of evaporated Sb_2Se_3 films grown on glass with substrate temperatures ranging from 24°C to 550°C. The films are amorphous in nature until substrate temperatures of 500°C are reached, above which they become crystalline. The spectra for the layers showing crystalline peaks have been background subtracted for clarity. Sb_2Se_3 reference peaks are shown at the bottom of the figure.

Figure 6.3 shows the XRD spectra collected from films grown on 500 and 550°C substrates before background subtraction was applied. Both films exhibit both Bragg peaks and a diffuse background. It is unclear, however, to what extent the possible amorphous component is from the glass substrate or amorphous Sb_2Se_3.

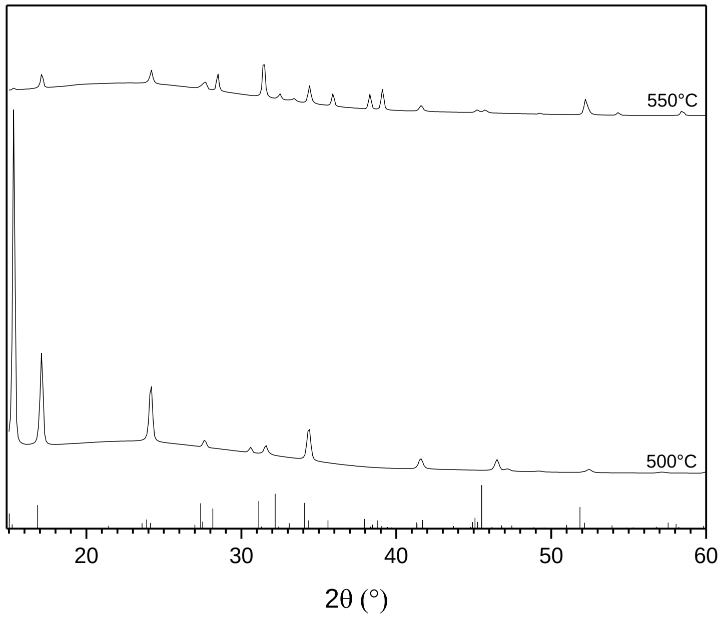

Figure 6.3: XRD spectra of Sb_2Se_3 evaporated onto glass substrates at 500 and 550°C without background subtraction or normalisation performed. Sb_2Se_3 reference peaks are shown at the bottom of the figure.

Table 6.1: XRD data for as-grown Sb_2Se_3 films grown on glass at 500 and 550°C (see also Fig. 6.1). The texture coefficients (TC) indicate that the 500°C film is highly oriented (020) while the 550°C is not.

	Literature		500°C		550°C	
2θ (°)	*hkl*	Intensity	Intensity	TC	Intensity	TC
15.05	020	0.136	1.000	13.35	0.056	0.34
16.89	120	0.457	0.275	1.09	0.419	0.75
24.19	310	0.115	0.164	2.60	0.417	2.99
27.43	230	0.473	0.020	0.08	0.217	0.38
28.30	211	0.734	0.000	0.00	0.515	0.58
31.27	221	1.000	0.027	0.05	1.000	0.82
32.32	301	0.650	0.000	0.00	0.186	0.23
33.23	311	0.208	0.000	0.00	0.099	0.39
34.16	240	0.461	0.092	0.36	0.547	0.98
35.72	231	0.314	0.000	0.00	0.373	0.98
37.96	401	0.222	0.000	0.00	0.451	1.67
38.90	141	0.298	0.000	0.00	0.623	1.72
41.49	421	0.173	0.031	0.32	0.179	0.85
45.23	501	0.210	0.000	0.00	0.083	0.32
45.80	002	0.396	0.000	0.00	0.084	0.17
52.27	360	0.108	0.009	0.15	0.479	3.66
54.22	232	0.120	0.000	0.00	0.081	0.56
58.36	242	0.167	0.000	0.00	0.127	0.62

The Tauc plot methodology was employed for the estimation of the band gaps of the films from the transmission and reflectance spectra determined by UV-vis-IR spectroscopy. Figure 6.4 shows the plots for each of the films. Since the plots do not contain clear linear sections it was not possible to make an accurate determination of the band gaps from them. Nevertheless, the plots do fall into two clear groups, the amorphous films forming a set on the right, having band gaps of approximately 1.0 – 2.1 eV, while the two crystalline ones have lower gaps, approximately 1.6 - 1.7 eV. This is reminiscent of the behaviour of thin film Sb_2S_3 [5] for which both amorphous and crystalline films have been studied both structurally and optically. In that case, the amorphous films also displayed a slightly higher band gap than the crystalline ones.

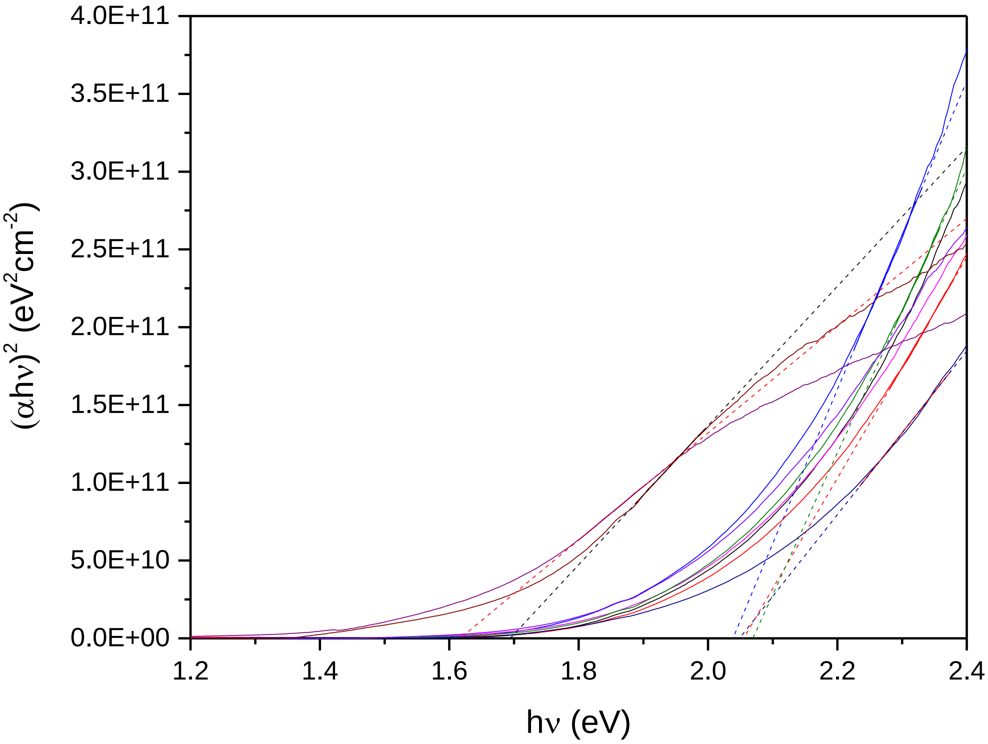

Figure 6.4: Tauc plots for Sb_2Se_3 films evaporated onto glass at substrate temperatures ranging from room temperature to 550°C. They clearly display a reduction of the band gap upon the appearance of polycrystalline structure above 500°C.

6.3.2 Post-growth annealing of evaporated Sb_2Se_3 films

The XRD spectra shown in Figure 6.5 belong to films grown at 24, 150 and 250°C (see above) after post-growth annealing at 350°C for 30 minutes on a hotplate in a N_2 glovebox. For all three films the amorphous character is lost and the XRD patterns show distinct peaks indicating their crystalline character. While the number of peaks in each pattern differs, all three contain Sb_2Se_3 peaks for the (120) and (420) planes at approximately $2\theta = 17°$ and 34° respectively. Nevertheless, there are differences in the preferred orientations of the three films.

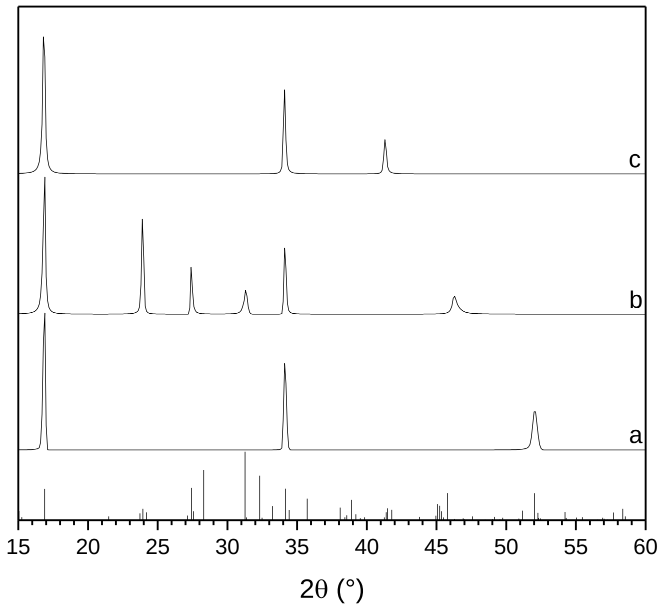

Figure 6.5: Effect of post-growth annealing on the XRD patters of Sb_2Se_3 films evaporated onto glass at a) room temperature, b) 150°C and c) 250°C. The annealing took place under nitrogen at 350°C. The Sb_2Se_3 reference peaks are shown underneath the experimental data.

These differences are likely due to one or more of the following: the thermal history of the films (i.e. the substrate temperature during deposition), small variations in the evaporation process, or small variations in the annealing process.

In order to explore the causes, further experiments on growth and annealing were designed to discriminate between the effects of run to run variations in either the deposition (evaporation run) or the post-growth annealing. Figures 6.5 - 8 and Tables 6.2 - 4 show the comparisons of the XRD patterns and texture data between films grown at each substrate temperature, but which were all post-growth annealed at 350°C but using various combinations of simultaneous deposition and/or annealing steps.

For the films grown at room temperature and shown in Figure 6.6 and Table 6.2 two deposition runs were made (evaporation #1 and evaporation #2) and also two annealing runs (annealing #1 and annealing #2). Figure 6.6 shows the outcome of three combinations: a) evaporation #1 / annealing #1, b) evaporation #1 / annealing #2, and c) shows evaporation #2 / annealing #2. Of these b) and c) are very similar and are different from a). This indicates that it is the *annealing part* of the process that has influenced the texture of the film – films b) and c) were annealed together but grown separately – rather than the growth. These observations are backed up by the peaks' texture coefficients in Table 6.2. Furthermore, all spectra show that the most prevalent orientations are those for which the covalent ribbons run parallel to the substrate. This is discussed further in Section 6.4.

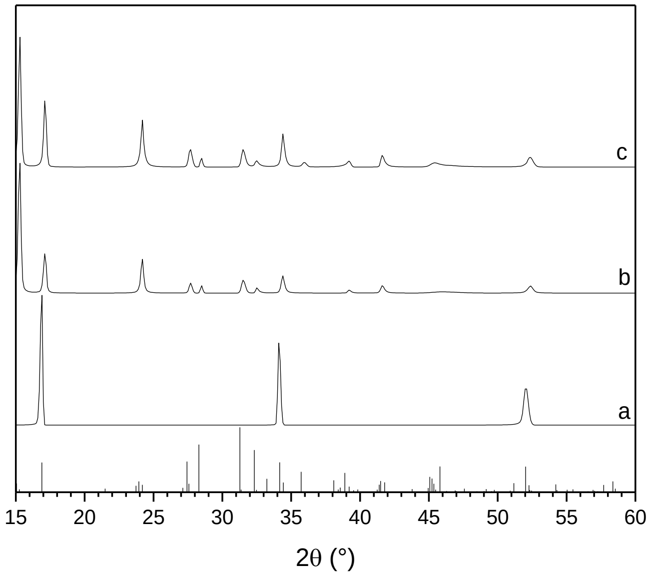

Figure 6.6: XRD comparison of room temperature grown films (24°C). (a) evaporation run #1, annealing run #1 (b) evaporation run #1, annealing run #2 and (c) evaporation run #2, annealing run #2. Sb_2Se_3 reference peaks are shown underneath.

Table 6.2: Texture coefficients for each of the indexed peaks in the films grown on room temperature substrates (24°C). The letters a, b and c correspond to the XRD spectra shown in Figure 6.6. Films b) and c) were post growth annealed simultaneously and show similar texture coefficients.

	Literature		Film a		Film b		Film c	
2θ (°)	Intensity	*hkl*	Intensity	TC	Intensity	TC	Intensity	TC
15.05	0.136	020	0.00	0.00	1.00	8.66	1.00	7.16
16.89	0.457	120	1.00	4.98	0.30	0.78	0.51	1.08
24.19	0.115	310	0.00	0.00	0.26	2.67	0.36	3.07
27.43	0.473	230	0.00	0.00	0.08	0.19	0.13	0.28
28.30	0.734	211	0.00	0.00	0.06	0.09	0.07	0.09
31.27	1.000	221	0.00	0.00	0.10	0.12	0.13	0.13
32.32	0.650	301	0.00	0.00	0.04	0.07	0.05	0.07
34.16	0.461	241	0.63	3.12	0.13	0.34	0.26	0.54
35.72	0.314	231	0.00	0.00	0.00	0.00	0.03	0.11
38.90	0.298	141	0.00	0.00	0.02	0.09	0.05	0.15
41.49	0.173	421	0.00	0.00	0.06	0.39	0.09	0.51
45.23	0.210	501	0.00	0.00	0.00	0.00	0.03	0.15
45.80	0.396	002	0.00	0.00	0.00	0.00	0.00	0.00
52.27	0.108	360	0.28	5.90	0.05	0.59	0.07	0.67

Figures 6.7 and 6.8 show a comparison between the XRD patterns observed after the annealing step for films grown at substrate temperatures of 150 and 250°C respectively. For each substrate temperatures, two samples a) and b) (as seen in the respective XRD spectra figures) were formed in the same evaporation run before being annealed in separate runs.

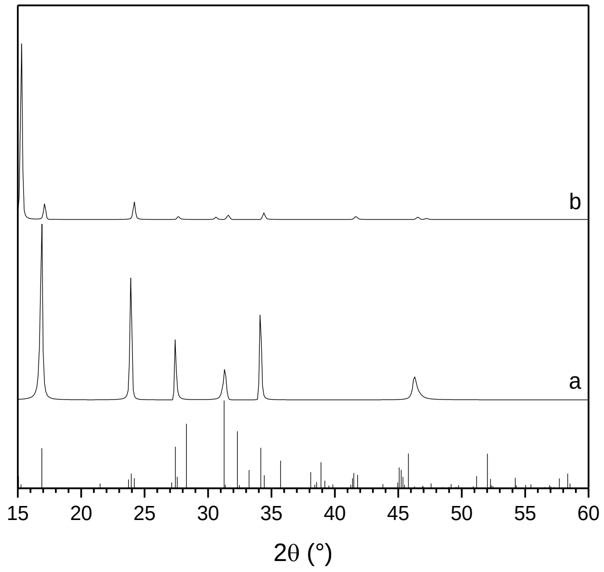

Figure 6.7: XRD of Sb_2Se_3 films grown on glass simultaneously at 150°C and then post-growth annealed separately at 350°C.

Table 6.3: Texture coefficients for each of the indexed peaks in the XRD patterns from films grown at 150°C and then post-growth annealed as shown in Figure 6.7.

	Literature		Film a		Film b	
2θ (°)	Intensity	*hkl*	Intensity	TC	Intensity	TC
15.05	0.136	020	0.00	0.00	1.00	11.86
16.89	0.457	120	1.00	2.91	0.09	0.31
24.19	0.115	310	0.69	8.06	0.10	1.39
27.43	0.473	230	0.34	0.96	0.01	0.05
28.30	0.734	211	0.00	0.00	0.01	0.03
31.27	1.000	221	0.17	0.23	0.02	0.04
32.32	0.650	301	0.00	0.00	0.00	0.00
34.16	0.461	241	0.48	1.40	0.04	0.13
35.72	0.314	231	0.00	0.00	0.00	0.00
38.90	0.298	141	0.00	0.00	0.00	0.00
41.49	0.173	421	0.00	0.00	0.02	0.14
45.23	0.210	501	0.00	0.00	0.00	0.00
45.80	0.396	002	0.13	0.44	0.01	0.05
52.27	0.108	360	0.00	0.00	0.00	0.00

Figure 6.7a and b show that the two different post-growth annealing runs give very different texture outcomes, as was the case for films deposited at room temperature. The values in Table 6.3 for film a) demonstrate the presence of six different orientations, and the peaks for (120) and (310) at 2θ = 16.9 and 24.2° respectively have significantly higher texture coefficients than the others. Nevertheless, the patterns differ significantly with sample b) showing weaker XRD peaks all round but a high intensity for the (020) planes (2θ = 15.05°), which does not appear in sample a).

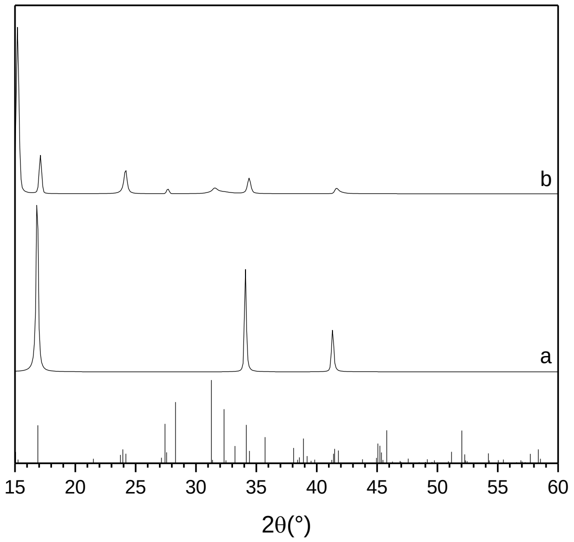

Figure 6.8: XRD of Sb_2Se_3 films grown on glass simultaneously at 250°C and then post-growth annealed separately at 350°C in runs a) and b). Sb_2Se_3 reference peaks are shown underneath.

Similarly Figure 6.8 and Table 6.4 show the XRD and texture coefficients for films deposited simultaneously but annealed separately at 250°C. The same behaviour for the room temperature and 150°C deposited films is evident: the two post-growth annealing runs confer different crystallographic textures on the films. Run to run variability in the annealing has a significant influence on the crystallographic texture, independent of the deposition temperature. These Sb_2Se_3 films appear to be unusually sensitive in this regard.

Table 6.4: Texture coefficients for each of the indexed peaks in the XRD patterns from films grown at 250°C shown in Figure 6.8.

	Literature		Film a		Film b	
2θ (°)	Intensity	*hkl*	Intensity	TC	Intensity	TC
15.05	0.136	020	0.00	0.00	1.00	10.78
16.89	0.457	120	1.00	6.17	0.23	0.74
24.19	0.115	310	0.00	0.00	0.14	1.77
27.43	0.473	230	0.00	0.00	0.03	0.09
28.30	0.734	211	0.00	0.00	0.00	0.00
31.27	1.000	221	0.00	0.00	0.03	0.05
32.32	0.650	301	0.00	0.00	0.00	0.00
34.16	0.461	241	0.61	3.76	0.09	0.30
35.72	0.314	231	0.00	0.00	0.00	0.00
38.90	0.298	141	0.00	0.00	0.00	0.00
41.49	0.173	421	0.25	4.06	0.03	0.27
45.23	0.210	501	0.00	0.00	0.00	0.00
45.80	0.396	002	0.00	0.00	0.00	0.00
52.27	0.108	360	0.00	0.00	0.00	0.00

The SEM micrographs in Figure 6.9 show three typical films grown by thermal evaporation onto a room temperature substrate for each of the following cases: as grown, annealed post growth at 350°C on a hotplate in a N_2 atmosphere, and annealed post growth at 400°C on a hotplate in a N_2 atmosphere. In agreement with the XRD evidence that the films are amorphous films (Figure 6.2) there is no visible grain structure in the as grown sample. Once annealed, the films crystallise into ~500 nm sized grains. When annealed at 350°C films have good adherence to the substrate and near complete surface coverage. Those annealed at 400°C have a grain size of ~500 nm as in the case of the 350°C films, however the films are visibly less continuous.

Visually, all films were grey in colour and before the annealing step the films have a mirror-like finish. Once annealed the samples had a lighter grey, matte finish with the number of pinholes visible when held up to a light source increasing with the annealing temperature.

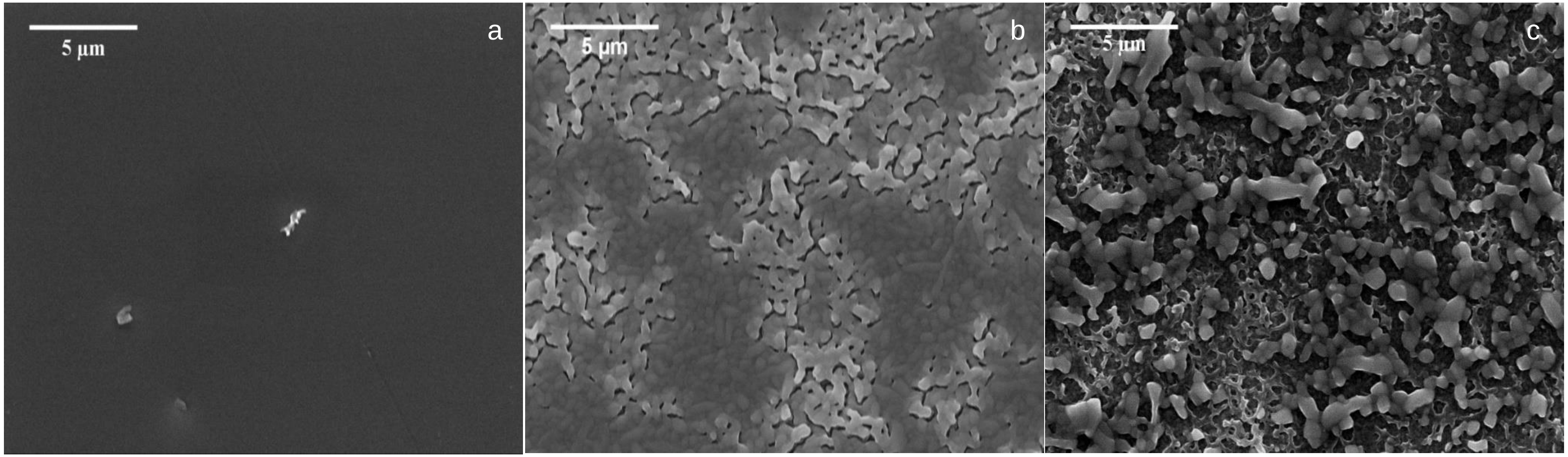

Figure 6.9: SEM micrographs of Sb_2Se_3 films deposited by thermal evaporation. Shown here are the as grown case (a), film annealed at 350°C for 30 minutes on a hotplate in a N_2 atmosphere (b), and 400°C for 30 minutes on a hotplate in a N_2 atmosphere (c).

6.3.3 Growth of Sb_2Se_3 on InP (100) wafers

The growth of Sb_2Se_3 on glass (i.e. amorphous) substrates did not show a specific preferred growth orientation. The extent to which the growth can be templated by growth on highly oriented substrates is now explored. Sb_2Se_3 was thermally evaporated onto room temperature (100) InP wafers and its crystallographic texture investigated. Figure 6.10 shows the XRD spectra of the as deposited and post-growth annealed Sb_2Se_3 films. The annealing temperature of each film is indicated alongside its respective spectrum. In all of the spectra the InP (200) and (400) peaks are observed at 30.5 and 63.4° respectively (marked with diamonds) and are so intense as to obscure any other peaks from phases of similar 2θ angles.

The XRD of the as grown Sb_2Se_3 films on the (100) InP wafers (Figure 6.10) shows two peaks corresponding to the (230) and (171) orientations in the material, having 2θ angles of 27.7 and 60.3° respectively. The (230) peak is denoted with a triangle and the (171) with a circle. Contrary to the case seen in Figure 6.2 for films on glass, films deposited onto room temperature (100) InP substrates display a partly oriented polycrystalline structure demonstrating that the growth of the Sb_2Se_3 is at least somewhat templated by the substrate. The two peaks visible in the XRD spectrum are not harmonics so the film is not epitaxial. Overall these films show a strong preferred orientation of (171).

Annealing causes the films to recrystallise, with the (171) peak disappearing in those films annealed at 300°C or above and with the (230) peak remaining in all but the 300°C annealed film. As on glass the (020) and (120) peaks are represented in the spectra, although orientation control beyond that in the unannealed film is not seen.

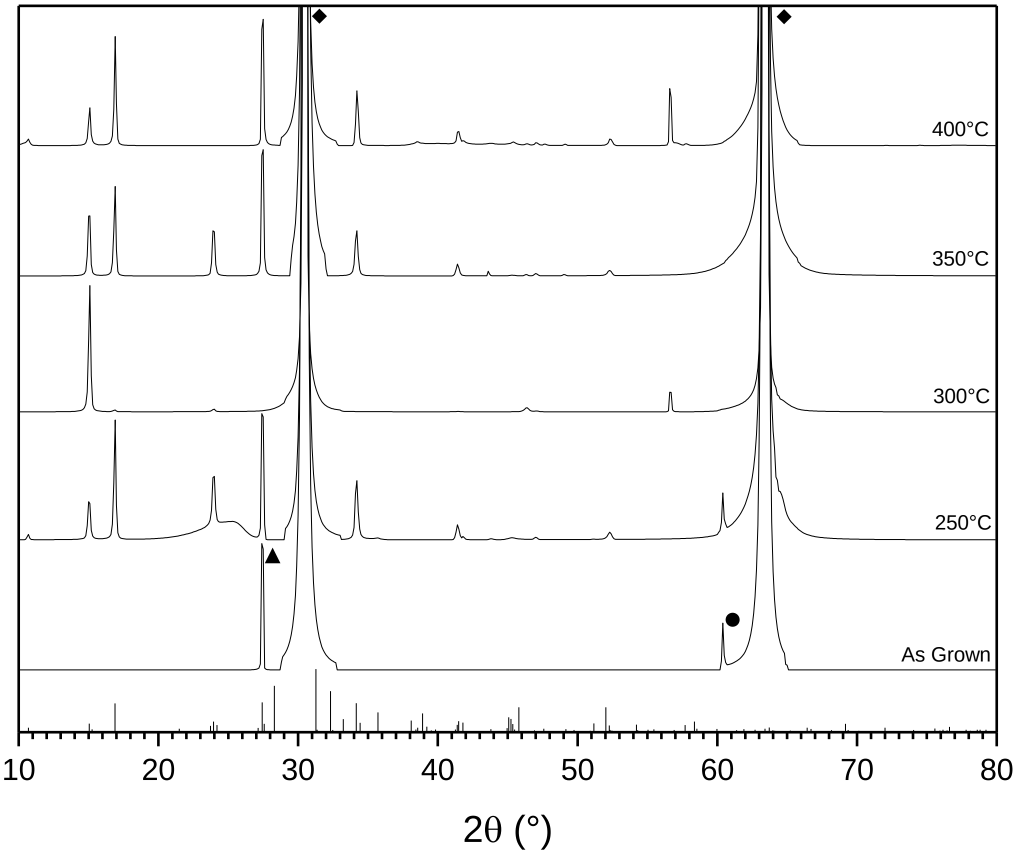

Figure 6.10: XRD spectra of Sb_2Se_3 films deposited onto room temperature (100) InP wafers and annealed at 250-400°C. The large peaks at 2θ values of 30.5 and 63.4° belong to the (200) and (400) planes of InP respectively. Sb_2Se_3 reference peaks are shown underneath.

Table 6.5: Texture coefficients for each of the peaks analysed in the Sb_2Se_3 film grown on InP wafers shown in Figure 6.10. TC values are calculated from the spectra for the as grown films and for those anneal post deposition at temperature in the range 250-400°C.

	Literature		As Grown		250°C		300°C		350°C		400°C	
2θ (°)	Intensity	*hkl*	Intensity	TC	Intensity	TC	Intensity	TC	Intensity	TC	Intensity	TC
10.7	0.15	110	0.00	0.00	0.00	0.00	0.00	0.00	0.00	0.00	0.05	0.17
15.05	0.29	020	0.00	0.00	0.30	0.67	1.00	3.69	0.48	3.22	0.30	0.50
16.89	0.97	120	0.00	0.00	0.95	0.62	0.02	0.02	0.71	1.42	0.86	0.42
23.94	0.35	130	0.00	0.00	0.50	0.90	0.02	0.06	0.36	1.96	0.00	0.00
27.43	1.00	230	1.00	0.88	1.00	0.64	0.00	0.00	1.00	1.94	1.00	0.47
34.16	0.97	240	0.00	0.00	0.47	0.31	0.00	0.00	0.36	0.71	0.43	0.21
41.39	0.24	250	0.00	0.00	0.12	0.31	0.00	0.00	0.09	0.75	0.00	0.00
41.49	0.37	421	0.00	0.00	0.00	0.00	0.00	0.00	0.00	0.00	0.11	0.15
56.56	0.03	142	0.00	0.00	0.00	0.00	0.16	6.23	0.00	0.00	0.45	8.09
60.33	0.04	171	0.37	9.12	0.37	6.56	0.00	0.00	0.00	0.00	0.00	0.00

6.3.4 Growth of Sb_2Se_3 on RF sputtered CdS thin films

Since CdS is a candidate for the window layer in Sb_2Se_3 devices the behaviour of Sb_2Se_3 grown on CdS-coated “TEC15” glass substrates was also investigated. Depositions were carried out on substrates at room temperature. Figure 6.11a is the XRD spectrum obtained from RF sputtered CdS on TEC15 for the purpose of identifying substrate. Figures 6.11b) and c) are the spectra obtained from Sb_2Se_3/CdS/TEC15 samples, b) is taken from an as-grown film and c) is from a film after annealing at 350°C on a hotplate in a N_2 atmosphere for 30 minutes. Figure 6.11d is the spectrum obtained from Sb_2Se_3 films deposited onto glass and annealed simultaneously with those on the CdS substrates.

The as-grown sample on a CdS substrate does not display sufficiently different XRD response to the bare substrate, so there is no evidence to suggest that crystalline Sb_2Se_3 is formed under these conditions. However, both annealed films show predominant Sb_2Se_3 peaks. The films grown on glass show a strong preferred orientation of (020). By comparison, those grown on CdS display a (101) preferred orientation, albeit much less strong.

These films were annealed simultaneously and thus have as close to identical heating conditions as is possible indicating that the orientation of the annealed Sb_2Se_3 films is dependent not only on the conditions during the anneal, but also on the nature of the substrate.

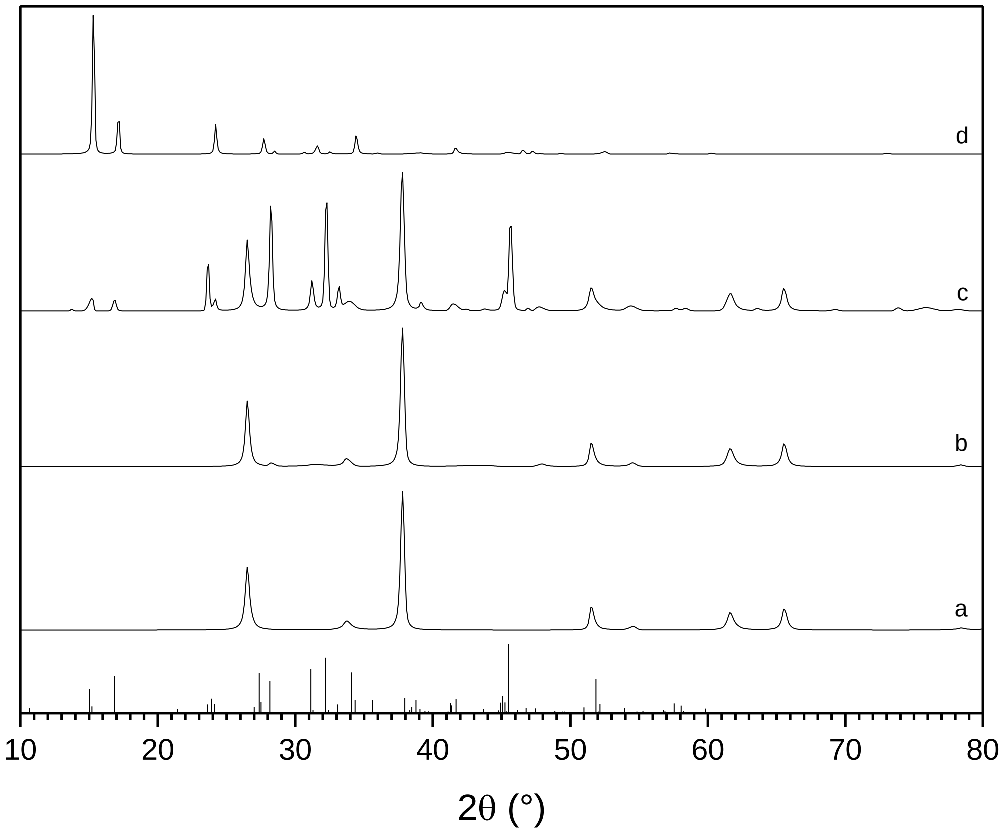

Figure 6.11: XRD spectra of (a) CdS RF sputtered onto TEC15 glass to be used as substrates for the Sb_2Se_3 films (b) Sb_2Se_3 deposited onto CdS substrates (c) Sb_2Se_3 deposited onto CdS substrates and annealed at 350°C on a hotplate for 30 minutes in a N_2 atmosphere, and (d) Sb_2Se_3 deposited onto soda-lime glass and annealed at 350°C on a hotplate for 30 minutes in a N_2 atmosphere. Sb_2Se_3 reference peaks are shown underneath

Table 6.6: Texture coefficients for each of the indexed peaks in the films grown on room temperature substrates shown in Figure 6.11.

	Literature		On Glass		On CdS	
2θ (°)	Intensity	*hkl*	Intensity	TC	Intensity	TC
15.05	0.14	020	1.00	6.88	0.12	0.73
16.89	0.46	120	0.23	0.48	0.10	0.18
23.73	0.10	101	0.00	0.00	0.43	3.62
24.19	0.11	310	0.21	1.74	0.11	0.82
28.30	0.73	211	0.02	0.03	0.97	1.11
31.27	1.00	221	0.06	0.06	0.28	0.24
32.32	0.65	301	0.00	0.00	1.00	1.30
33.23	0.21	311	0.13	0.59	0.23	0.92
41.49	0.17	421	0.04	0.22	0.07	0.32
45.23	0.21	501	0.00	0.00	0.19	0.77
45.80	0.40	002	0.00	0.00	0.78	1.67
46.91	0.03	600	0.03	0.87	0.03	0.79
47.58	0.06	610	0.00	0.00	0.04	0.59

6.3.5 Comparison of Sb_2Se_3 post growth annealing in a furnace and on a hotplate

The nature of the hotplate setup does not allow for more consistent annealing steps, so alternatives were investigated. Figure 6.12 shows photographs of annealed films in both the box furnace and hotplate arrangements described in 6.2.1.c i and ii respectively. Both annealing processes were performed at the same temperature (350°C) and for the same duration (30 minutes). The temperature in the furnace was measured using a thermocouple in the centre of the furnace and the hotplate was preheated and its temperature checked using a radiative thermometer.

The box furnace method was not successful since films on glass, CdS and InP do not survive annealing by this method without serious loss of material. XRD carried out on these films is shown in Figures 6.13 and 6.14. In both the CdS and the InP cases peaks which cannot be attributed to Sb_2Se_3 or the substrate form upon annealing. These are most likely due to oxides due to incomplete purging of the furnace with nitrogen. The disappearance of the (200) InP peak at $2\theta = 30.5°$ in the annealed sample (Figure 6.14), while curious, is of little consequence to the success of annealing in this arrangement. The main finding is that annealing in the box furnace caused significant materials loss and hence film degradation.

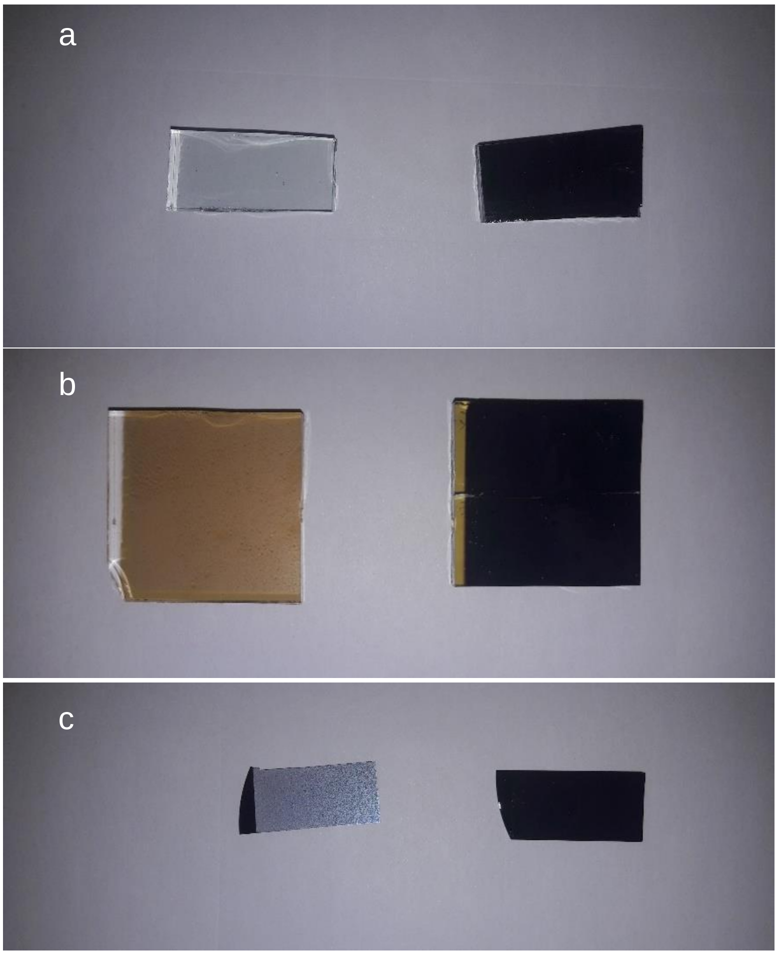

Figure 6.12: Thermally evaporated Sb_2Se_3 films on (a) soda-lime glass (b) RF sputtered CdS on TEC15 glass and (c) (100) InP wafers. Post growth annealing was performed on each for 30 minutes at 350°C in box furnace with N_2 feed in (left) and on a hotplate in a N_2 atmosphere (right).

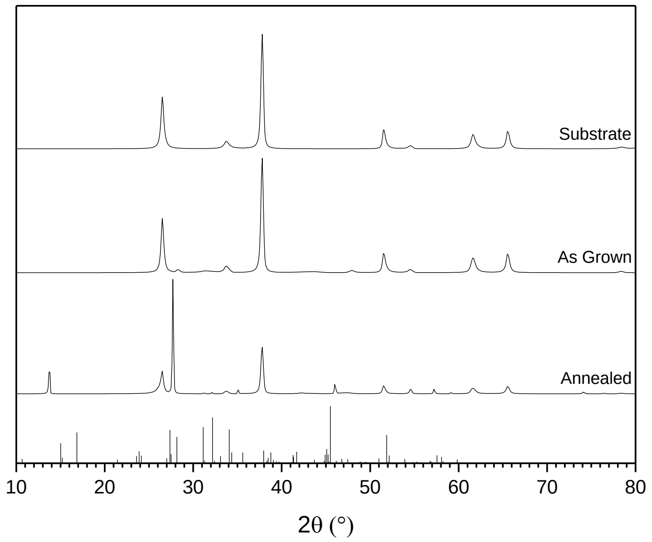

Figure 6.13: XRD spectra of Sb_2Se_3 films deposited onto RF Sputtered CdS films pre- and post-annealing at 350°C for 30 minutes in a box furnace with a N_2 feed in. Sb_2Se_3 reference peaks are shown underneath.

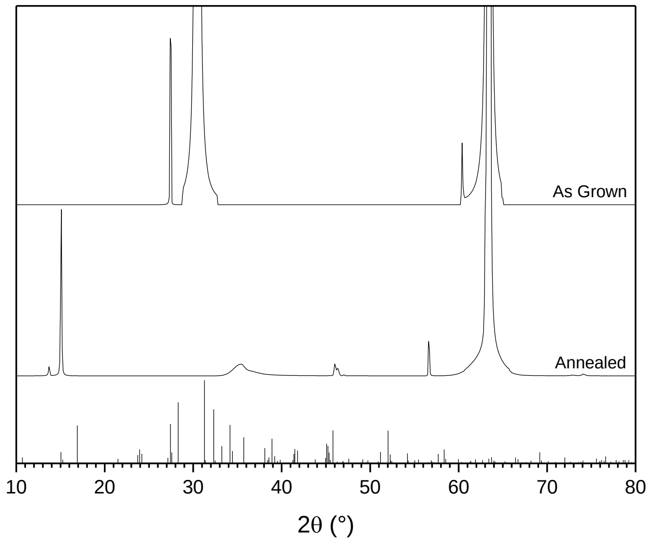

Figure 6.14: XRD spectra of Sb_2Se_3 films deposited onto (100) InP wafers pre- and post-annealing at 350°C for 30 minutes in a box furnace with a N_2 feed in. Sb_2Se_3 reference peaks are shown underneath.

6.4 Discussion

Sb_2Se_3 was deposited by thermal evaporation from a compound source. The resultant films did not exhibit evidence of secondary phases and all peaks in XRD spectra of these polycrystalline films were able to be attributed to the intended binary material.

In all cases with glass substrates at temperatures ranging between 24°C (i.e. room temperature) and 450°C the films produced by thermal evaporation were entirely amorphous as shown in Figure 6.2. Amorphous material is undesirable for PV not only due to its increased band gap (~1.9 eV versus ~1.6 eV for polycrystalline films) but also in that the main potential advantage of Sb_2Se_3 over similar band gap semiconductors lies in its structure. This benefit is negated by a lack of crystallinity, amorphous semiconductors being unable to display anisotropic properties but also having low mobility. Once substrate temperatures of 500°C or greater are used, the Sb_2Se_3 forms polycrystalline films during growth, however with the available data it is not possible to determine if these are entirely polycrystalline or whether they still have an amorphous component. Regardless, the necessity of such high substrate temperatures to achieve any degree of crystallinity is not attractive for production of devices, especially with a view to upscaling, thus an alternative method of achieving polycrystallinity is desirable.

The Structure Zone Model is appropriate for materials which form crystalline layers even below $0.3T_m$ (-8°C for Sb_2Se_3). The films grown at “Zone II” substrate temperatures (i.e. 24 and 150°C) are amorphous in structure and this remains the case through “Zone III” up to substrate temperatures of 500°C (~0.8T_m). Both 500 and 550°C samples have distinct Sb_2Se_3 diffraction peaks. In the 500°C sample one peak has much greater intensity than any others observed, indicative of a preferred orientation.

The Structure Zone Model originates from metallurgy so its applicability to semiconductors is compromised even before considering the structure of Sb_2Se_3 with its strong, covalent bonds along one axis and weak van der Waals bonds along the remaining two. This may account for the discrepancies from it seen experimentally in this work.

The (020) orientation seen in the 500°C sample is problematic for device incorporation, since here the Sb_2Se_3 ribbons run parallel to the substrate. Not only does this orientation mean that the grain boundaries will likely have dangling bonds and hence be electrically active, but also that charge carriers must “hop” between adjacent chains to enable separation of the electron-hole pair. In the 550°C film there are two orientations with high texture coefficients compared to the other peaks present in the film are (310) and (360) which are again orientations where Sb_2Se_3 ribbons run parallel to the substrate. The (221) orientation found to be beneficial by Zhou[6] occurs in the 550°C substrate temperature film, and despite being the strongest peak of those orientations considered from the data, it is not as well-represented as would be expected in random orientation.

The amorphous nature of the films deposited onto glass substrates at temperatures below 500°C as shown in Figure 6.2 suggests that there is insufficient thermal energy available to allow atoms to move once deposited onto the substrate. The activation energy is overcome in the films when the energy is provided by high substrate temperatures (i.e. ≥ 500°C) giving Sb_2Se_3 the ability to organise into a polycrystalline structure.

The annealing temperature (350°C) required to cause crystallisation of amorphous films is lower than that of the substrate temperature required to grow polycrystalline films directly (500°C). Starting from the assumption that the mechanism behind the transition between amorphous and polycrystalline films is thermally activated, the cause of this difference is now discussed. Factors considered for the heating process here are: i) geometry, ii) time, iii) temperature and iv) pressure.

i. The geometry of the heating setup in both circumstances is that the substrate is heated from the opposite side to the film, so the origin of the discrepancy is unlikely to be from a temperature difference from the annealing configuration.
ii. The duration of the post-growth anneal is 30 minutes while the deposition was carried out at ~3 $Ås^{-1}$ for a thickness of ~350 nm, leading to a deposition time of approximately 20 minutes; while the anneal duration was 1.5 times that of the deposition, this is not considered significant enough to be solely responsible for the transition from amorphous to polycrystalline films.
iii. The temperature was measured slightly differently in each case. The hotplate used for the post-growth annealing step was heated to temperature and measured by a radiative thermometer before the sample was placed on top. For the evaporation the stage (made of steel) temperature was monitored by a thermocouple and the substrate

was allowed 20 minutes to equalise to the desired temperature. For both annealing and evaporation, temperatures were measured at the base of the glass. There is, however, a difference here between the two heating processes due to the presence of a larger temperature gradient through the glass in the annealing setup. Such a temperature gradient may result in a lower effective annealing temperature however this would only serve to increase the discrepancy between the two temperatures required to achieve crystalline material.

iv. The pressure of the two systems was different. The anneal was undertaken in a N_2 glovebox at atmospheric pressure whereas the evaporation was performed at a pressure of 5×10^{-4} mbar. This is the most drastic difference between the four conditions listed above when considering the difference between the annealing and film growth thermal conditions.

The difference in behaviour during growth and annealing may also lie in the fact that the growth is an additive process whereas the annealing is a reconstruction.

The growth process involves species arriving at the surface and, provided they do not immediately leave, they begin migration across the surface. These species will either stick at low energy sites or leave the substrate. The migration process required to generate crystalline films requires an activation energy, provided here by the substrate heating.

In the annealing process, the reorganisation of the films is described with reference to the theory of annealing of cold worked metals (i.e. “recovery”, “recrystallisation” and “grain growth”). Cold worked metals are highly strained, this volume strain drives “recovery” in which the material crystallises coherently from its defective state (this is similar to the transition from amorphous to crystalline). Similarly, in the “recrystallisation” stage the still strained material nucleates the formation of new, more perfect grains again driven by volume strain. The final stage, “grain growth” acts to minimise grain boundary energy in the entire film [7]. Here the volume strain driven amorphous to crystalline transition apparently takes place at a lower temperature than the migration of surface species during growth to produce crystalline films. This indicates that the activation energy for the “recovery”-like processes is less than the activation energy for the surface mobility of Sb-Se species.

Thermally activated diffusion can be described by Equation 6.1

$$D(T) = D_0 \exp\left(-\frac{E_A}{\mathrm{k}T}\right) \qquad \text{Equation 6.1}$$

where the diffusion rate of each process is dependent on its respective activation energy (E_A). It would be expected that the activation energy for surface mobility is lower for the surface than for the volume mobility and therefore that the activation energy will be lower for the growth than annealing-induced crystallisation. This is at odds with the experimental observation and is likely due to the peculiarity of the material itself and its anisotropic bonding.

Recystallisation and high temperature annealing processes are used more widely in solar processing. For example, Khrypunov reports the growth of CdTe devices by evaporation of both CdS and CdTe where both are grown at elevated temperatures[8]. The CdS was deposited at 150°C and recrystallised by a 450°C anneal; the CdTe was grown at 300°C and $CdCl_2$ treated at 430°C in air. CIGS devices use high temperature steps during the deposition of the absorber layer[9], the world record efficiency for CZTS devices requires an annealing step at 540°C[10]. Whether the high temperature is required for crystallinity in these materials is unclear from the publications.

Growth on (100) InP appears to have encouraged textured Sb_2Se_3 films (with the reservation that the relative quantities of polycrystalline and amorphous material are not revealed by XRD alone). It is worth noting however, contrary to what is observed on the soda-lime glass substrates (where thermally evaporated films are amorphous), that highly textured grain structure is formed even onto InP substrates at room temperature. This texturing is lost during annealing steps, the presence of the strong (171) orientation disappearing completely at 300°C and with one or more of the common (020) and (120) peaks at all annealing temperatures.

The ability to grow ordered films at room temperature on InP wafers suggests that it is possible, given an appropriate substrate, to grow highly oriented Sb_2Se_3 films. What is not clear from these results, however, is whether this templated growth is possible with favoured orientations having the c-axis of the Sb_2Se_3 unit cell perpendicular to the substrate surface which would be the ideal case for charge transport through a layered device. The films made in this study show a tendency toward growth in <*hk*0> directions (i.e. ribbon direction parallel to the substrate and hence surface). The prevalence of these orientations grown onto the substrates investigated, whether it be via deposition (in those samples with substrate temperatures of ≥500°C) or via annealing induced crystallisation, suggests that there is a mechanism promoting ribbon growth parallel to the substrate. It is most likely that these orientations have the lowest energy.

Templated growth of crystalline Sb_2Se_3 on CdS was not successful. The XRD spectra taken from samples of Sb_2Se_3 grown onto CdS coated substrates displayed only peaks from the uncoated CdS before the Sb_2Se_3. These films were amorphous but annealing of Sb_2Se_3 films grown on CdS/SnO_2:F/glass caused the appearance of strong Sb_2Se_3 peaks in XRD spectra. Polycrystalline films produced by annealing these samples do not exhibit strong preferred orientations. They do, however, differ in orientation from films on uncoated glass substrates, even when annealed in identical conditions, indicating that the nature of the substrate has substantial impact on the crystallisation of the films.

A summary of the substrates used for Sb_2Se_3 growth and the observations before and after the post-growth anneal is presented in Table 6.7.

Table 6.7: Summary of substrates used for Sb_2Se_3 growth, preparation conditions for the substrates pre-Sb_2Se_3 deposition, and details on the crystallinity of the resulting Sb_2Se_3 films before and after the post-growth anneal.

Substrate	**Preparation**	**Pre-anneal**	**Post-anneal**
Glass	Rinse and scrub with DI water and IPA	Amorphous	Polycrystalline
CdS	CdS sputtered immediately prior	Amorphous	Polycrystalline
InP	Transferred from inert	Some crystallinity, not monocrystalline	Polycrystalline, pre-anneal orientation lost

Polycrystalline Sb_2Se_3 films produced in this way show promise for incorporation into full device structures despite the lack of orientation control. This will be explored in Chapter 7.

The use of a box furnace was attempted as a method of annealing samples in a more repeatable manner than the use of the hotplate. The severity of material loss in addition to the presence of impurities in the annealed samples exclude this as a reasonable alternative for the production of device quality Sb_2Se_3 films.

6.5 Conclusions

The extent to which Sb_2Se_3 adheres to the Structure Zone Model has been investigated, the results of which strongly suggest that the material does not follow this model at all, favouring the formation of amorphous films. Sb_2Se_3 grown by thermal evaporation on soda-lime glass has been shown to form amorphous layers at substrate temperatures below 500°C and polycrystalline films above.

For the amorphous films, annealing has been shown to convert them to polycrystalline material, and this takes place independently of the substrate type. The growth of Sb_2Se_3 on a single crystal substrate – (100) InP – has been shown to template the growth of the material, encouraging the (171) orientation. However, growth on polycrystalline RF sputtered CdS substrates results in amorphous Sb_2Se_3 films.

As on glass, amorphous Sb_2Se_3 films on CdS can be converted to polycrystalline by an annealing step. Run-to-run inconsistency in the orientations observed in post-annealed films was observed and demonstrated to be caused by the annealing step itself.

Sb_2Se_3 films suitable for device incorporation were produced by annealing layers deposited onto room temperature CdS/SnO_2:F/glass at 350°C for 30 minutes. The films produced by this method, though polycrystalline are unpredictable in their preferred orientation which must be considered when comparing similarly processed devices. It is concluded that the only reliable way to draw true comparisons in making devices is to break up larger areas of annealed films into device-sized pieces (since the annealing step is the origin of this unpredictability).

References for Chapter 6

1. Wang, L., Li, D., Li, K., Chen, C., Deng, H., Gao, L. & Zhao, Y. Stable 6%-effcient Sb_2Se_3 solar cells with a ZnO buffer layer. *Nat. Energy* **2**, 17046 (2017).
2. Grovenor, C. R. M., Hentzells, H. T. G. & Smith, D. A. The development of grain structure during growth of metallic films. **32**, 773–781 (1984).
3. Thornton, J. A. High rate thick film growth. *Annu. Rev. Mater. Sci.* **7:239-260**, (1977).
4. Kim, K. H. & Chun, J. S. X-ray studies of SnO_2 prepared by chemical vapour deposition. *Thin Solid Films* 287–295 (1986).
5. Ghosh, C. & Varma, B. P. Optical properties of amorphous and crystalline Sb_2S_3 thin films. *Thin Solid Films* **60**, 61–65 (1979).
6. Zhou, Y., Wang, L., Chen, S., Qin, S., Liu, X., Chen, J., Xue, D.-J., Luo, M., Cao, Y., Cheng, Y., Sargent, E. H. & Tang, J. Thin-film Sb_2Se_3 photovoltaics with oriented one-dimensional ribbons and benign grain boundaries. *Nat. Photonics* **9**, 409–415 (2015).
7. Humphreys, F. J. & Hatherly, M. *Recrystallization and Related Annealing Phenomena*. (Pergamon, 1995).
8. Khrypunov, G., Romeo, A., Kurdesau, F., Bätzner, D. L., Zogg, H. & Tiwari, A. N. Recent developments in evaporated CdTe solar cells. *Sol. Energy Mater. Sol. Cells* **90**, 664–677 (2006).
9. Jackson, P., Hariskos, D., Wuerz, R., Kiowski, O., Bauer, A., Friedlmeier, T. M. & Powalla, M. Properties of Cu(In,Ga)Se_2 solar cells with new record efficiencies up to 21.7%. *Phys. Status Solidi - Rapid Res. Lett.* **9**, 28–31 (2015).
10. Wang, W., Winkler, M. T., Gunawan, O., Gokmen, T., Todorov, T. K., Zhu, Y. & Mitzi, D. B. Device Characteristics of CZTSSe Thin-Film Solar Cells with 12.6% Efficiency. *Adv. Energy Mater.* **4**, 1301465 (2014).

7. Growth of Sb_2Se_3 devices

7.1 Introduction

In this chapter evaporated Sb_2Se_3 is used to make photovoltaic devices. The material's behaviour established in Chapter 6 will be used to inform device growth. Firstly, the importance of a P3HT hole blocking layer will be investigated. Since the addition of an extra layer in the device structure will increase series resistance it must increase the performance by enough to offset the resistance losses. Work function measurements are not present in the literature so common window layer choices are examined. In Chapter 6 a post-growth annealing step was demonstrated to be essential for formation of polycrystalline Sb_2Se_3 films so its impact on device performance is explored here. Stoichiometric variation in the absorber layer is performed by the co-evaporation of compound Sb_2Se_3 and elemental Sb or Se to investigate defect control. The optimum conditions were then used to grow the best possible device with these methods.

7.2 Experimental methods

In this study superstrate devices were grown onto SnO_2:F coated glass in the structure glass/SnO_2:F/window layer/Sb_2Se_3/pinhole blocking layer/Au. Details of fabrication of these follow:

a) Substrates

The substrates used in this work were “TEC15” SnO_2:F coated glass (NSG Ltd). Substrates were thoroughly cleaned with isopropanol followed by deionised water.

b) Window layers

The window layers used in this work were deposited by:

i) RF sputtering

50 nm of CdS and ZnS were both deposited by RF sputtering. Sputtering was undertaken from 2” targets (Pi-KEM) in an AJA Orion chamber. CdS sputtering was performed under 3 mTorr Ar for 30 minutes at a power of 50 W onto 200°C substrates. ZnS sputtering was performed under 3 mTorr Ar for 1 hour at a power of 50 W onto room temperature substrates.

ii) Spin coating

TiO_2 was deposited onto TEC15 glass by spin coating in a N_2 glovebox. Fresh 0.15 M and 0.3 M solutions of titanium isopropoxide in ethanol were prepared. 250 µl 0.15 M solution was coated dynamically at 3000 rpm for 30 seconds, then dried on a hotplate at 120°C for 10 minutes. Once dried 275 µl 0.3 M solution was coated on top dynamically, again at 3000 rpm for 30 seconds and dried at 120°C for 10 minutes. These layers were then removed from the glovebox immediately before use and annealed in air at 550°C for 30 minutes.

c) Sb_2Se_3 film deposition

The 300 nm thick Sb_2Se_3 films were grown onto room temperature substrates from the 99.999% pure compound source by thermal evaporation from a carbon crucible in a Moorfield MiniLab 080 thermal evaporator. The thickness of the films was monitored in-situ with a quartz crystal monitor and rate was maintained at 0.3 Å/s.

d) Post-growth annealing

Annealing of films was carried out on a hotplate in a nitrogen atmosphere. The hotplate was heated to the desired temperature, as measured with a radiative thermometer, before the samples were placed on top. Once the anneal had been performed, samples were removed and allowed to cool before removal from the N_2 atmosphere.

e) P3HT pinhole blocking layer

10 mg/ml solutions of P3HT in chlorobenzene were prepared by stirring on a hotplate at 70°C for 1 hour before passing through a PTFE filter. For 2.5×2.5 cm^2 and 5×5 cm^2 samples 70 µl and 125 µl solution respectively was spin coated dynamically onto substrates at 4000 rpm for 30 seconds. Samples were then placed on a hotplate at 150°C for 10 minutes to drive off the remaining solvent.

f) Contact deposition

i) Au contacts

50 nm thick Au contacts were deposited onto the devices by thermal evaporation with a mask for 0.1 cm^2 contact size. For each sample measuring 2.5×2.5 cm^2 a total of 16 contacts was applied, each of which formed an individual PV device.

ii) Front contact

Since the devices had the superstrate configuration, the semiconductor and contact materials were deposited on top of the FTO coating. Hence to form a front (light side contact), a small area of the P3HT and Sb_2Se_3 layers were removed with a razor blade and the CdS underneath was etched off using an HCl solution. Contact was then made through to the FTO with silver electrodag (Agar Scientific) for more reliable contacting for J-V and EQE measurements that could be achieved with a probe.

e) Characterisation

XRD spectra were obtained using a Rigaku SmartLab X-ray diffractometer. Measurements were taken in the range $15 < 2\theta < 80°$, and the resulting spectra were background subtracted and normalised. The J-V response under AM1.5 was measured using a TS Space Systems solar simulator. The EQE of devices was measured using a Bentham PVE 300. Samples were sent to NSG Ltd. for ToF SIMS analysis using a 25KeV Bi^{3+} analysis beam and a 1KeV Cs^{+} sputtering beam.

7.3 Results

7.3.1 P3HT pinhole blocking layer

In this section all devices comprised 300 nm Sb_2Se_3 evaporated onto CdS coated (50 nm) TEC15 glass which was post-growth annealed at 350°C for 30 minutes. The pinhole blocking layer was, where applicable, then applied before the Au contacts were evaporated onto the devices.

Figure 7.1 shows the current-voltage response of four devices: (a) a control sample (i.e. no pinhole blocking layer), (b) a sample with only the “drying” step performed (a sample with no P3HT layer but with the inclusion of heating on a hotplate at 150°C for 10 minutes), (c) with the P3HT pinhole blocking layer but no drying step, and (d) with both the P3HT and a drying step (heating as for (b) to remove any remaining chlorobenzene).

The control case (i.e. sample (a) with neither P3HT nor the drying step) shunts severely, exhibiting an Ohmic J-V trace (0.95 Ω·cm^2). The device with only the drying step performed (b) had a near-zero current across the full range of applied voltages indicating a high ohmic resistance, possibly due to oxides forming at the back surface of the Sb_2Se_3. With the P3HT applied, both (c) and (d) show vastly improved J-V response. Figure 7.2 shows box plots for *PCE*, J_{sc}, V_{oc}, and *FF* for devices (c) and (d). Devices with both the P3HT applied and the drying step performed show increased and more consistent values for each value than those with only the P3HT layer.

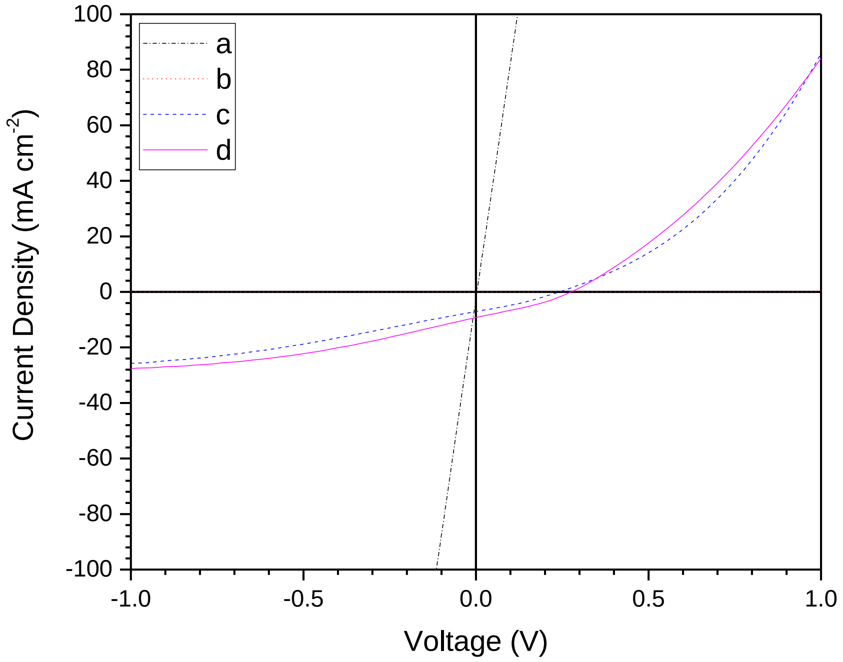

Figure 7.1: *J-V* response under AM1.5 from (a) Sb_2Se_3 device without P3HT or the annealing step (b) Sb_2Se_3 device without P3HT but with the 150°C anneal (c) Sb_2Se_3 device with a P3HT

pinhole blocking layer but no anneal (d) Sb_2Se_3 device with a P3HT pinhole blocking layer and 150°C anneal.

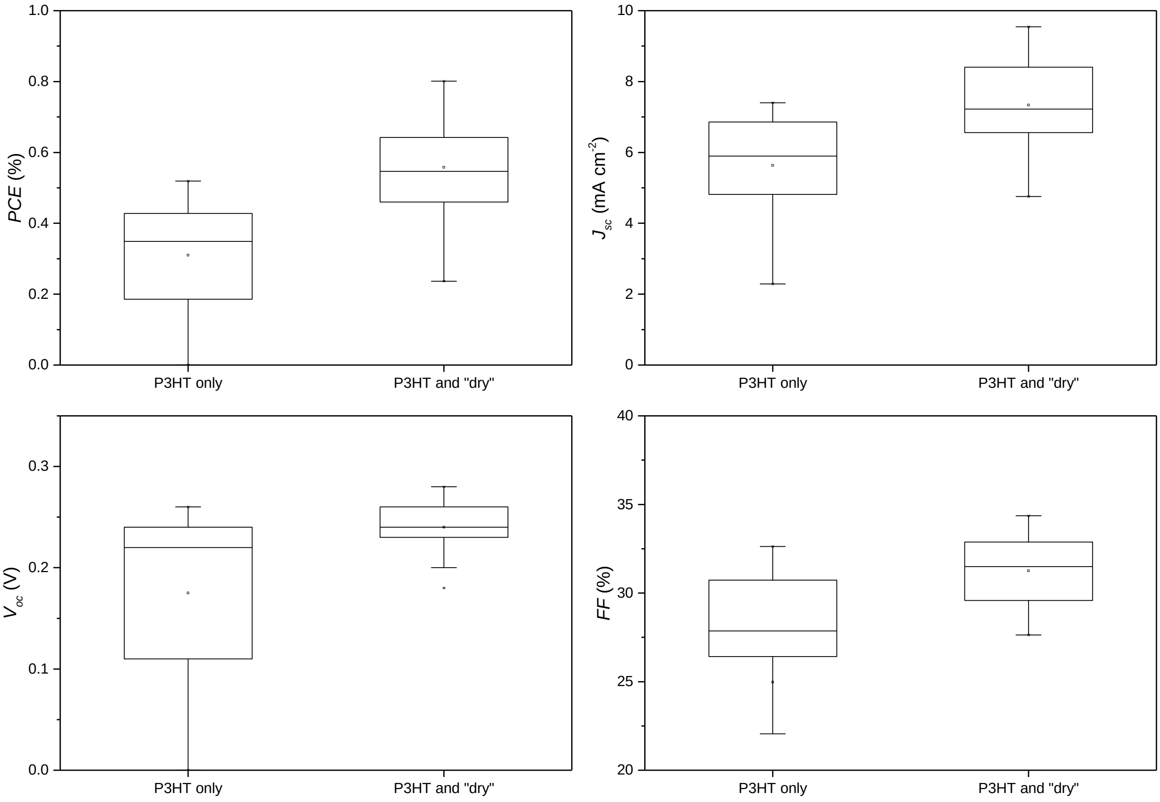

Figure 7.2: Box plots for the *PCE*, J_{sc}, V_{oc}, and *FF* of devices with the P3HT pinhole blocking layer both with and without the drying step.

7.3.2 Choice of window layer in evaporated Sb_2Se_3 devices

Figure 7.3 shows the *J-V* response of TEC15/Window/Sb_2Se_3/P3HT/Au devices and Table 7.1 shows the PCE, J_{sc}, V_{oc}, and *FF* of the best pixel from each device. The window layers used here were CdS, ZnS and TiO_2. Devices made using ZnS as the window layer showed diode-like behaviour but no photocurrent. Devices with either CdS or TiO_2 window layers show both diode-like curves and photocurrents of 20.2 and 15.2 mA·cm^2 respectively.

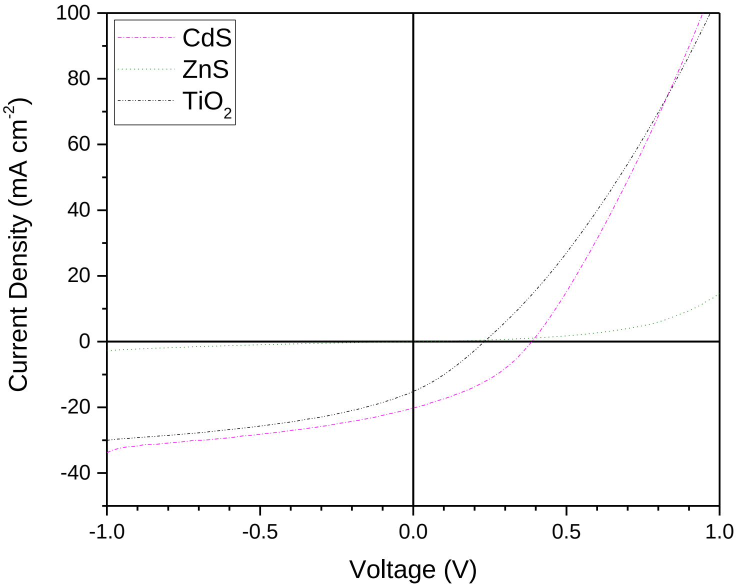

Figure 7.3: *J-V* responses under AM1.5 from devices with CdS, ZnS or TiO_2 as a window layer.

Table 7.1: Values of *PCE*, J_{sc}, V_{oc}, and *FF* for the highest efficiency Sb_2Se_3 PV devices made using CdS and TiO_2 window layers.

	PCE (%)	J_{sc} (mA·cm^{-2})	V_{oc} (V)	*FF* (%)
CdS	2.85	20.2	0.38	37.1
TiO_2	1.05	15.2	0.24	28.9

The J-V curve for TiO_2 shown in Figure 7.3 is for the response 2 days after the first measurement. Figure 7.4 shows the responses for the first 3 days. On the first day of measurement, the *J-V* response is s-shaped and has lower J_{sc}, *FF*, and hence *PCE* compared to the following two days. Measurements from days

2 and 3 display standard diode-like response. Values of *PCE*, J_{sc}, V_{oc}, and *FF* for each day are shown in Table 7.2.

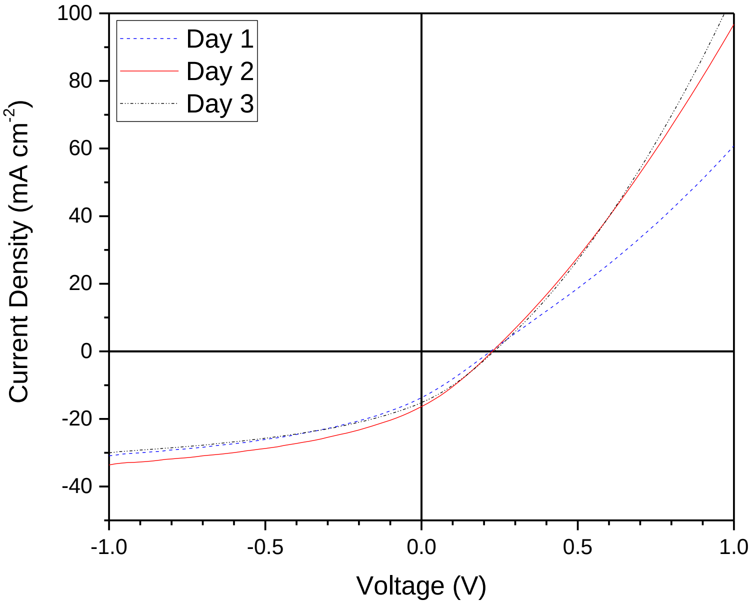

Figure 7.4: *J-V* response from the TiO_2 device taken over consecutive days, the initial measurement being 3 days after the growth of the device.

Table 7.2: Values of *PCE*, J_{sc}, V_{oc}, and *FF* for the highest efficiency pixel in the TiO_2/Sb_2Se_3 devices.

	PCE (%)	J_{sc} (mAcm^{-2})	V_{oc} (V)	*FF* (%)
Day #1	0.82	13.7	0.22	27.3
Day #2	1.08	16.3	0.22	29.9
Day #3	1.05	15.2	0.24	28.9

Figure 7.5 shows the Cd, S, Sb and Se profiles obtained from ToF SIMS on an evaporated Sb_2Se_3 device with CdS window layer. The intermixing between the

CdS and Sb_2Se_3 appears to be significant, the tail in the Sb and Se profiles reaching approximately half way through the CdS layer and likewise the Cd and S profiles both intrude into the Sb_2Se_3 layer.

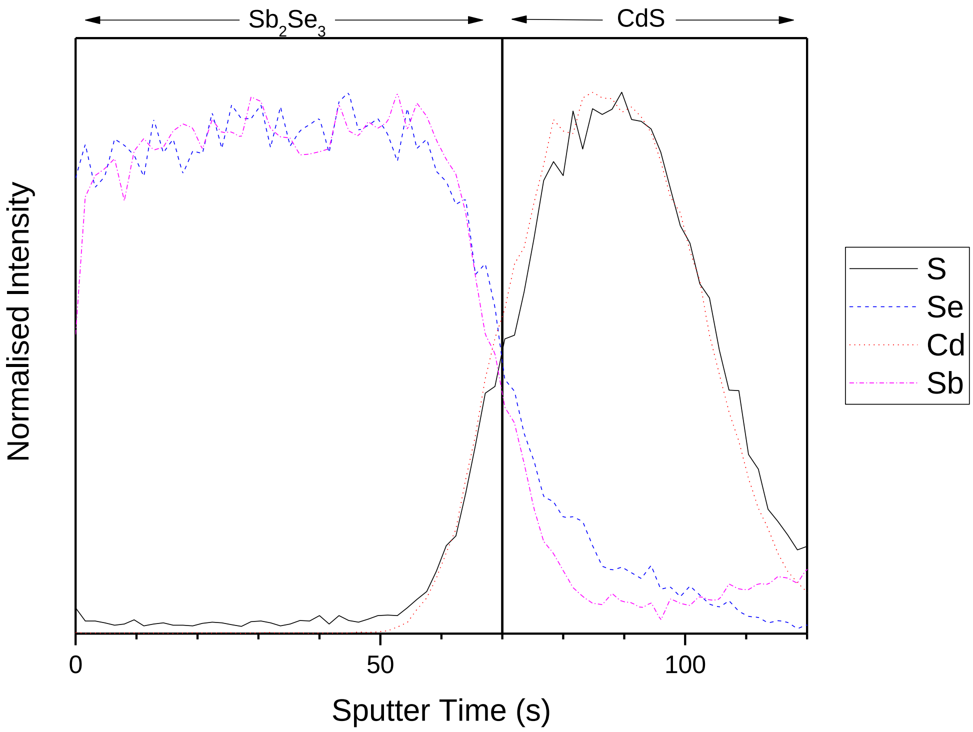

Figure 7.5: ToF SIMS of a CdS/Sb_2Se_3 device.

Figure 7.6 shows the Ti, TiO, O, Sb and Se profiles obtained from ToF SIMS on a TiO_2/Sb_2Se_3 device structure. The profiles associated with the TiO_2 window layer extend into the Sb_2Se_3 layer a similar depth (i.e. approximately 10 s worth of sputtering time). There is also an oxygen-rich region at the interface.

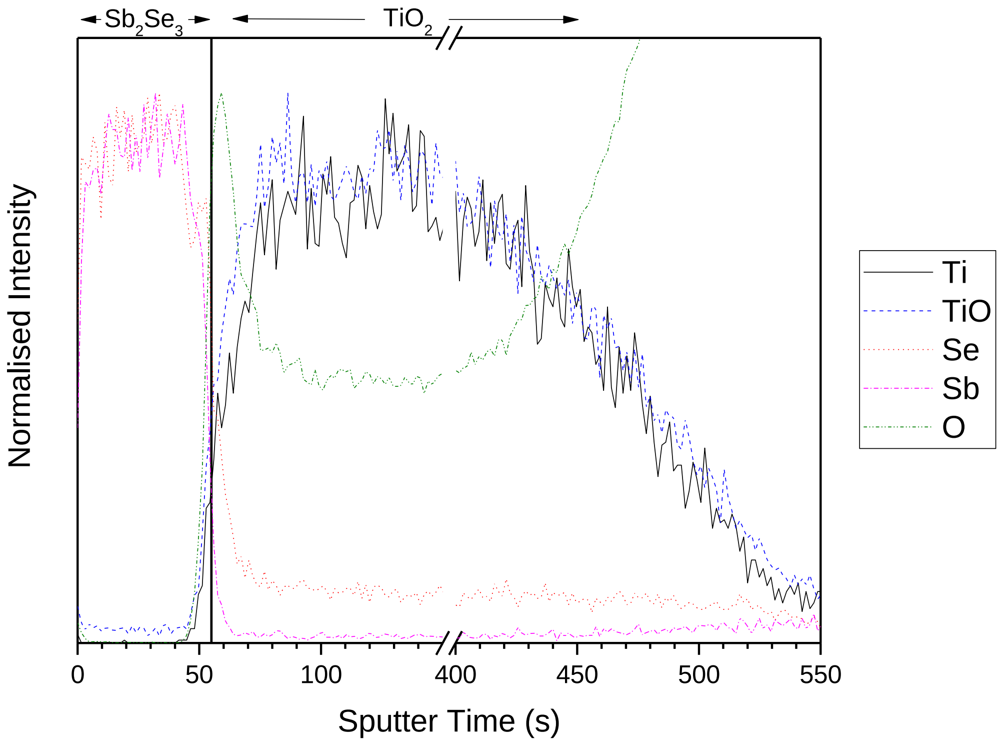

Figure 7.6: ToF SIMS of a TiO_2/Sb_2Se_3 device.

7.3.3 Sb_2Se_3 post-growth annealing conditions

The effect of varying post-growth annealing step for the Sb_2Se_3 films on the performance of devices was investigated, with the annealing being done in a N_2 atmosphere. TEC15/CdS/Sb_2Se_3 structures were placed onto a hotplate which had been preheated to the desired temperature and removed after 30 minutes. Devices were completed by the spin coating of P3HT, 150°C air anneal and evaporation of Au contacts.

Figure 7.7 shows the typical current-voltage response of cells with post-growth annealing temperatures of 250-450°C. S-shaped curves are seen in both the lowest (250°C) and highest (450°C) temperatures but there is no evidence of this in the intermediate temperatures. Figure 7.8 shows box plots of the *PCE*,

J_{sc}, V_{oc}, and FF for each post-growth annealing temperature. V_{oc} in the 300°C sample is the highest and most consistent (an average of 287 mV and a standard deviation of 12 mV if the one shorted device is excluded). The efficiency is influenced too strongly by the J_{sc} for this higher V_{oc} to be truly beneficial, indeed, across all temperatures the relative size and spread of the J_{sc} values dominate the efficiency and despite a large spread, the 350°C annealed samples show the most promise.

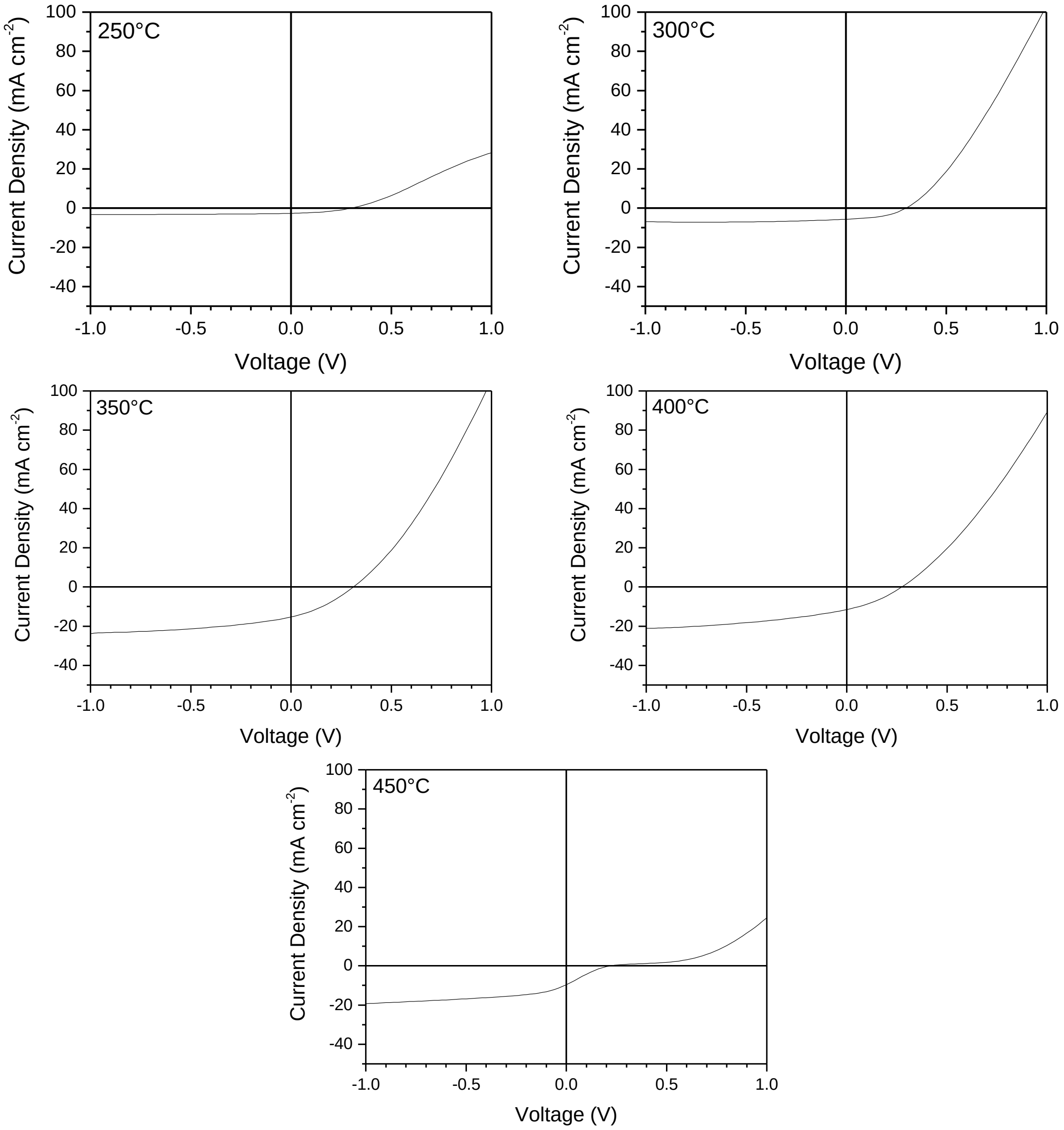

Figure 7.7: *J*-*V* response of typical Sb_2Se_3 devices with respect to the post-growth annealing temperature.

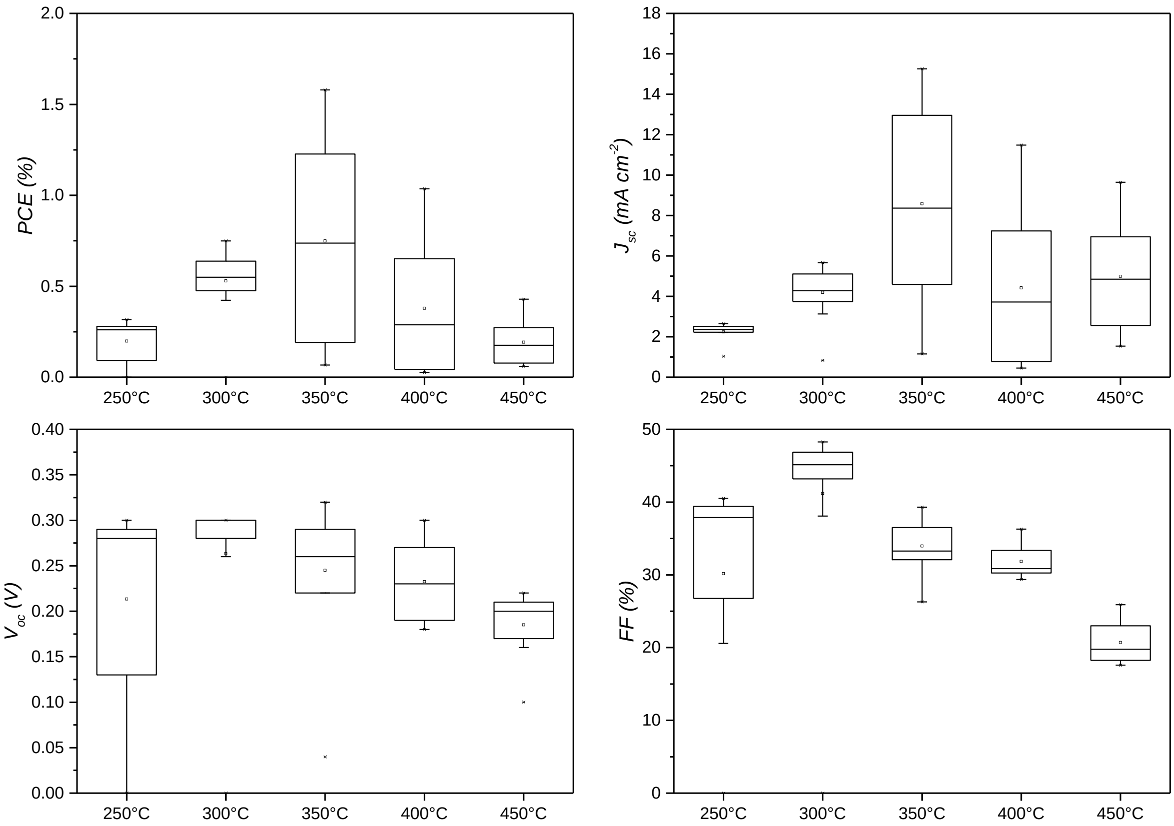

Figure 7.8: Box plots for the *PCE*, J_{sc}, V_{oc}, and *FF* of Sb_2Se_3 devices with respect to the temperature of the post-growth anneal.

7.3.4 Uniformity of evaporated Sb_2Se_3 devices

Larger area device plates (25 cm^2) were made and the efficiency variation measured on an array of contacts applied to this area was investigated for cells having CdS (Figure 7.9 and Table 7.3) or TiO_2 (Figure 7.10 and Table 7.4) window layers.

The CdS device shown has an area of low efficiency in the centre corresponding to a similar area of low J_{sc} and *FF*. The areas of high efficiency once again correspond to areas of high J_{sc} but not necessarily high *FF*.

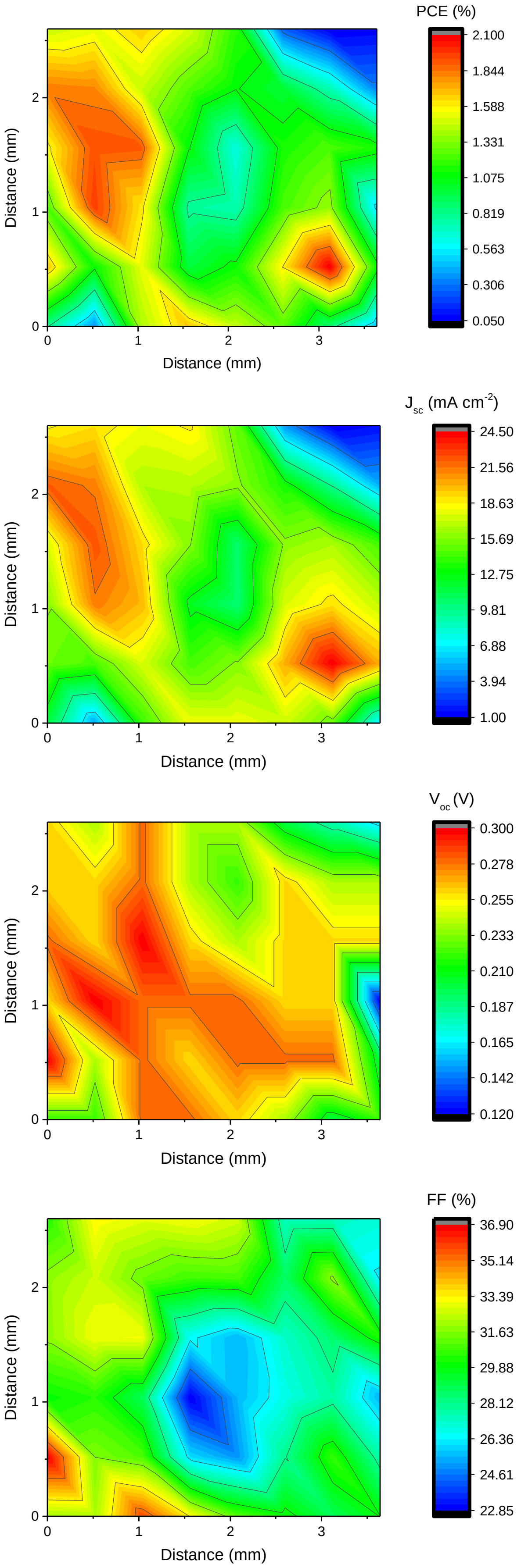

Figure 7.9: Distribution of values for *PCE*, J_{SC}, V_{OC} and *FF* in a typical 25 cm^2 CdS/Sb_2Se_3 device.

Table 7.3: Maximum, average and standard deviation for *PCE*, J_{sc}, V_{oc} and *FF* for a 25 cm^2 CdS/Sb_2Se_3 device having an array of 48 contacts.

	PCE (%)	J_{sc} (mAcm^{-2})	V_{oc} (V)	*FF* (%)
Max.	2.10	24.5	0.30	36.9
Mean	1.18	15.3	0.25	29.8
σ	0.50	5.3	0.04	3.0

The TiO_2 device shown in Figure 7.10 also has remarkable similarity to the efficiency variation in space and the J_{sc} variation. The V_{oc} and *FF* also vary in a similar pattern to the efficiency though the degree is somewhat obfuscated by the area of bad pixels at the edge of the device. This region is likely due to the improper device structure caused by the masking off of substrates for TiO_2 deposition and the subsequent coating with Sb_2Se_3 causing a large quantity of inconsistency in device structure and potentially contact of the Sb_2Se_3 with the underlying SnO_2:F TCO layer.

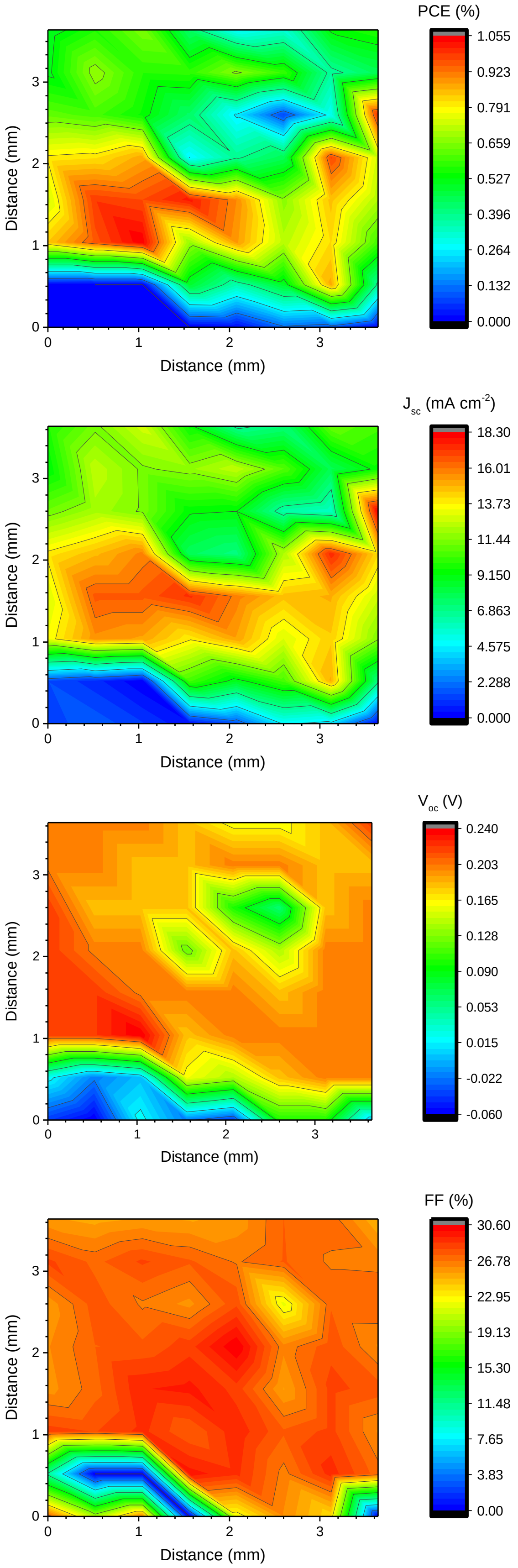

Figure 7.10: Distribution of values for *PCE*, J_{sc}, V_{oc} and *FF* in a typical 5×5 cm² TiO_2/Sb_2Se_3 device.

Table 7.4: Maximum, average and standard deviation for *PCE*, J_{sc}, V_{oc} and *FF* for a 5×5 cm^2 TiO_2/Sb_2Se_3 device having an array of 64 contacts.

	PCE (%)	J_{sc} (mAcm^{-2})	V_{oc} (V)	*FF* (%)
Max.	1.05	18.3	0.24	30.6
Mean	0.53	10.2	0.16	25.0
σ	0.31	4.9	0.08	7.0

7.3.5 Se- and Sb-rich Sb_2Se_3 devices by co-evaporation

Devices were grown Sb- and Se-rich by the co-evaporation of Sb or Se with Sb_2Se_3 onto CdS coated substrates. In both Sb- and Se-rich cases 2% weight of additional Sb or Se were co-evaporated with the Sb_2Se_3, the deposition rates for both of the materials being evaporate were held constant throughout the deposition. These device structures were annealed at 300, 350 and 400°C to allow for differences in the annealing process created by the addition of elemental Sb or Se. XRD spectra of these device structures are shown in Figure 7.11 alongside the bare CdS coated substrate for comparison. The peaks present in all the spectra belong either to the substrates or Sb_2Se_3 so there is no evidence that elemental Sb or Se remains in the films, at least in crystalline form. The Se-rich film does, however, have a more intense (120) peak at $2\theta = 16.89°$ than the pure Sb_2Se_3 and Sb-rich films. The presence of this orientation is detrimental to Sb_2Se_3 devices and must therefore be considered when comparing the performance of the devices.

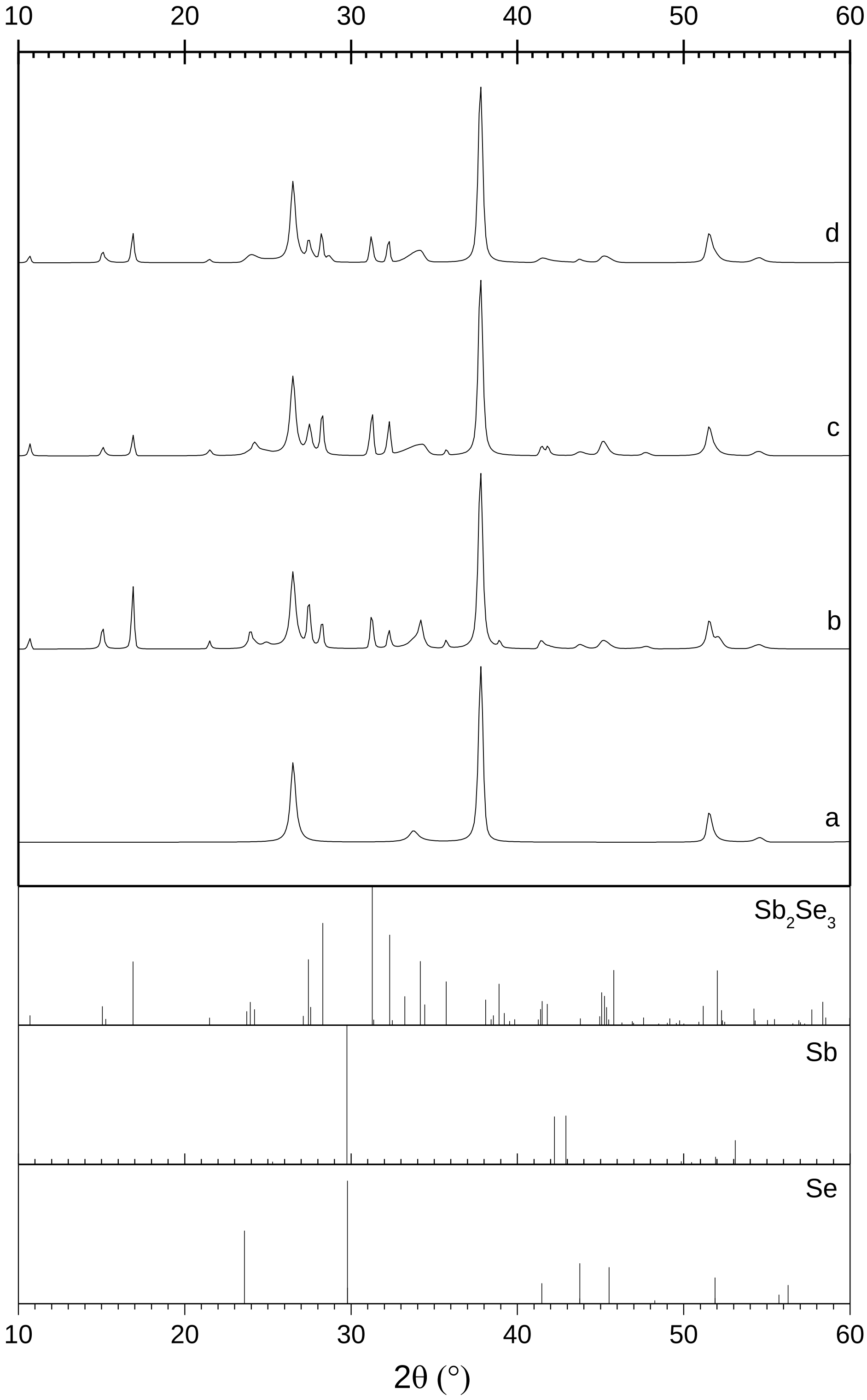

Figure 7.11: XRD spectra from (a) a CdS-coated substrate, (b) a Se-rich Sb_2Se_3 device structure after the annealing step, (c) a standard Sb_2Se_3 device structure after the annealing step and (d) a Sb-rich Sb_2Se_3 device structure after a 350°C annealing step. Literature data for S_2Se_3, Sb and Se are shown underneath.

Figures 7.12, 7.13 and 7.14 show box plots for each annealing temperature of the Sb-rich, Se-rich and pure Sb_2Se_3 devices. The Se-rich devices (Figure 7.11) have higher J_{sc} when annealed at 300°C than the higher temperatures but the poor V_{oc} values and fill factors cause the efficiency to vary significantly, higher temperatures.

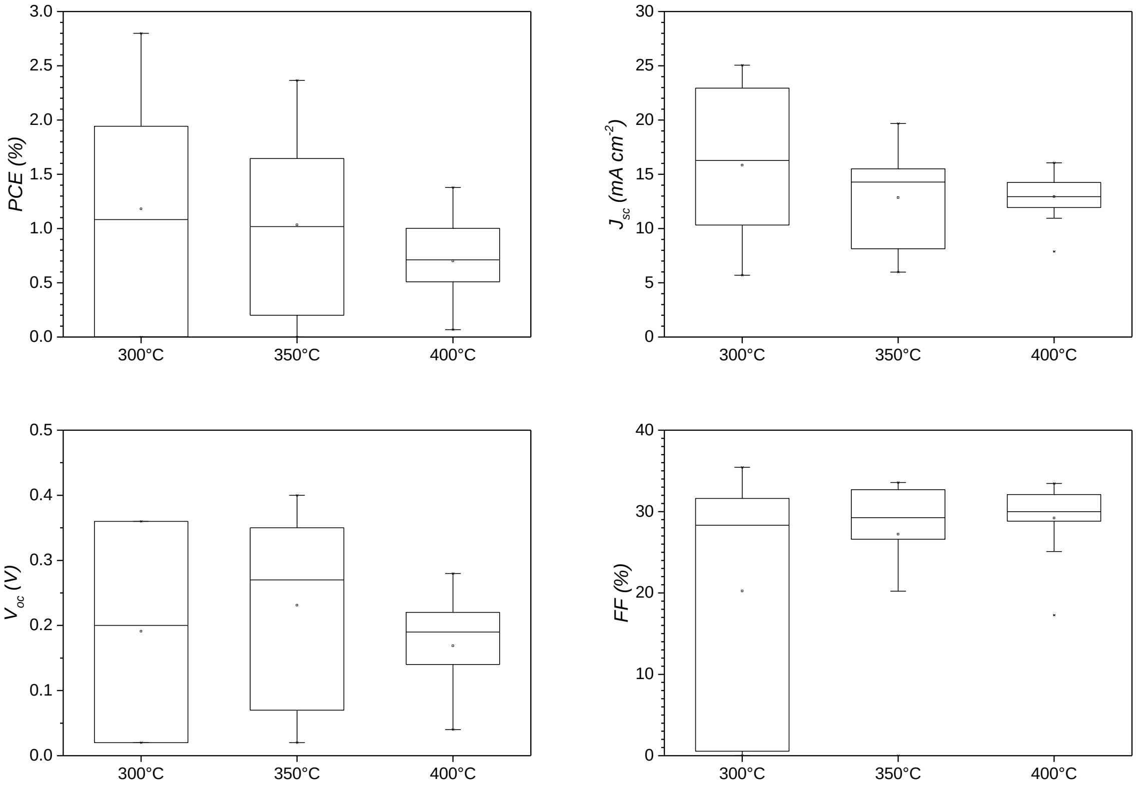

Figure 7.12: *PCE*, J_{sc}, V_{oc} and *FF* of Se-rich devices annealed at 300, 350, and 400°C.

The Sb-rich devices (Figure 7.13) have low efficiency compared to both the Se-rich and pure Sb_2Se_3 devices at 300 and 350°C. All four of the efficiency, J_{sc}, V_{oc} and *FF* are low in the Sb-rich devices. At a post-growth annealing temperature of 400°C the maximum and average values all begin to increase and are comparable to the Se-rich devices annealed at 300°C.

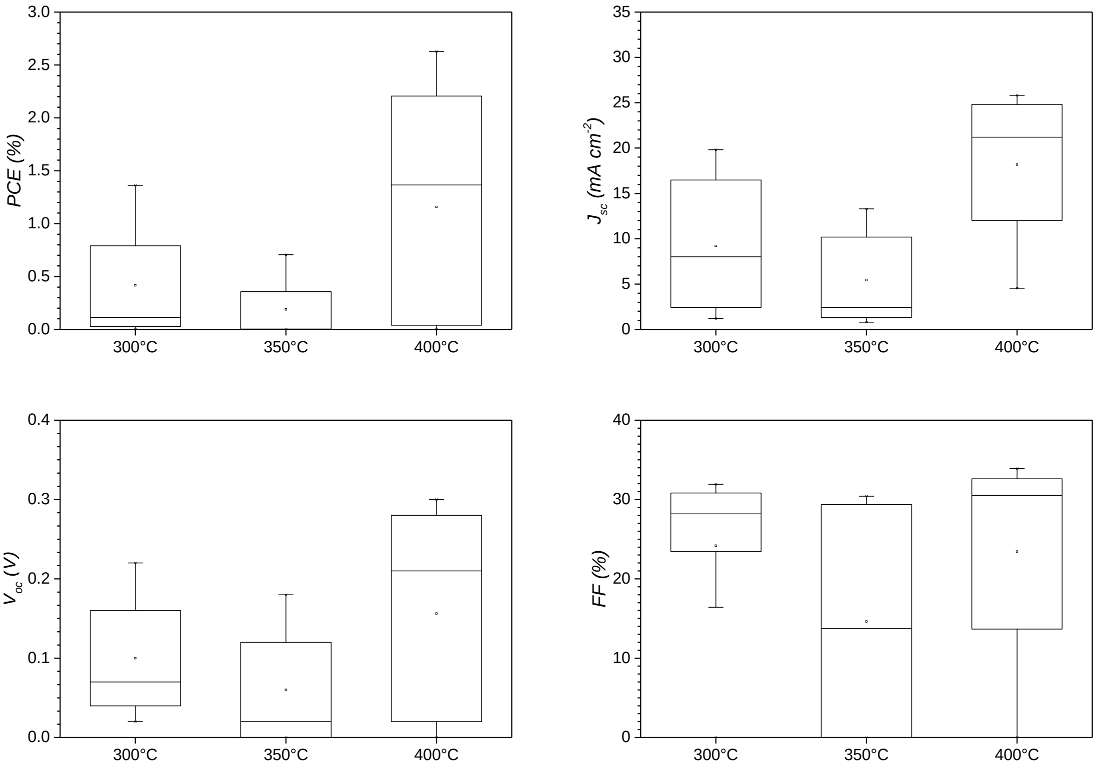

Figure 7.13: *PCE*, J_{sc}, V_{oc} and *FF* of Sb-rich devices annealed at 300, 350, and 400°C.

The performance of pure Sb_2Se_3 devices exceeds both the Sb- and Se-rich devices grown here. In concordance with the observations in Section 7.3.3, the 350°C annealed devices have the highest performance due to superior J_{sc} values. Se-rich devices are only marginally better than pure Sb_2Se_3 at 300°C (i.e. the anneal temperature resulting in the best Se-rich devices) and the pure Sb_2Se_3 (Figure 7.14) devices have better performance than the Sb-rich ones.

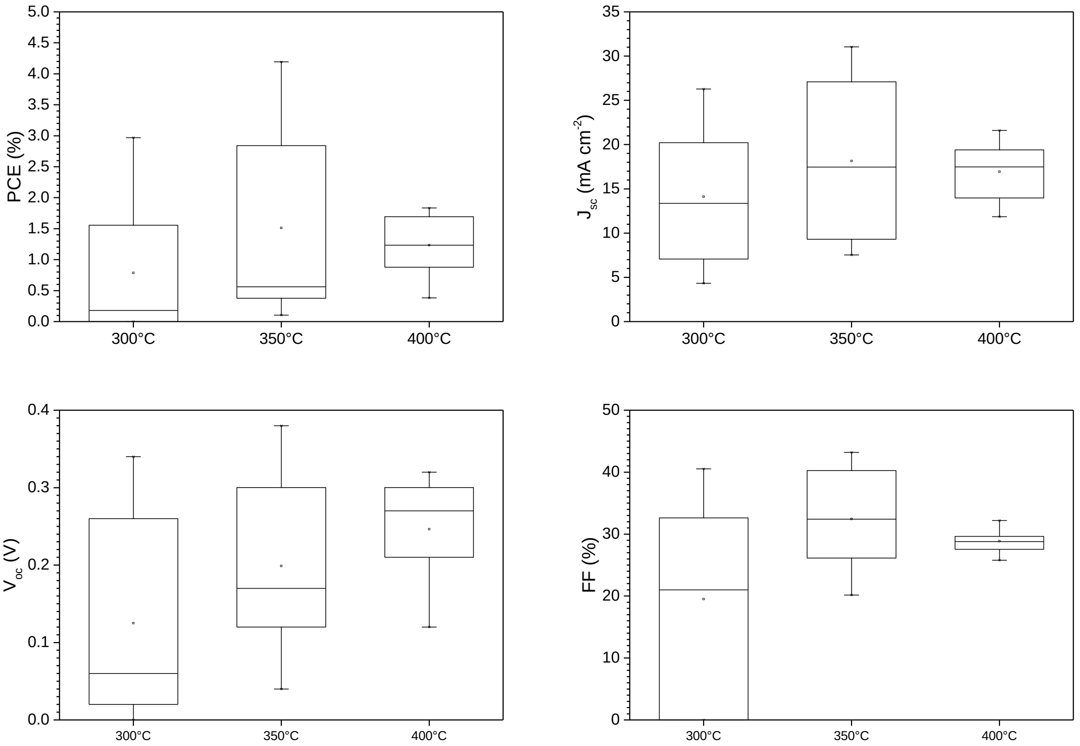

Figure 7.14: *PCE*, J_{sc}, V_{oc} and *FF* of pure Sb_2Se_3 devices annealed at 300, 350, and 400°C.

7.3.6 Champion Sb_2Se_3 device

Mohamed has reported that, according to simulations, the addition of a ZnS layer between the CdS layer and TCO increases the performance of CdTe devices[1]. Firstly, they report that the CdS layer may be thinned down to thicknesses below those possible with only a CdS layer since the ZnS works to prevent contact from the absorber layer to the TCO via the pinholes occurring in CdS when it becomes too thin. Secondly, they report that these bilayers result in fewer optical losses due to the grading of the band gap. This approach was investigated experimentally here.

Bilayers of ZnS/CdS grown by sequential sputtering, 25 nm ZnS was first sputtered onto TEC15 glass and then 25 nm CdS was sputtered on top, Sb_2Se_3 cells were grown using these bilayers in the structure

TEC15/ZnS/CdS/Sb_2Se_3/P3HT/Au. This cell has a 30 minute 350°C post-Sb_2Se_3 deposition anneal and a 10 minute 150°C drying step after the spin coating of P3HT. The total area of the device was 0.1 cm^2.

The champion device produced with this cell structure and in this work in general was 5.04% efficient. The J-V characteristics in the dark and under AM1.5 are displayed in Figure 7.15, showing a V_{oc} of 380 mV, J_{sc} of 29.3 $mA\cdot cm^{-2}$ and a fill factor of 45.3%. There is no evidence of “roll over” in the forward bias indicating the lack of an energy barrier at the back contact.

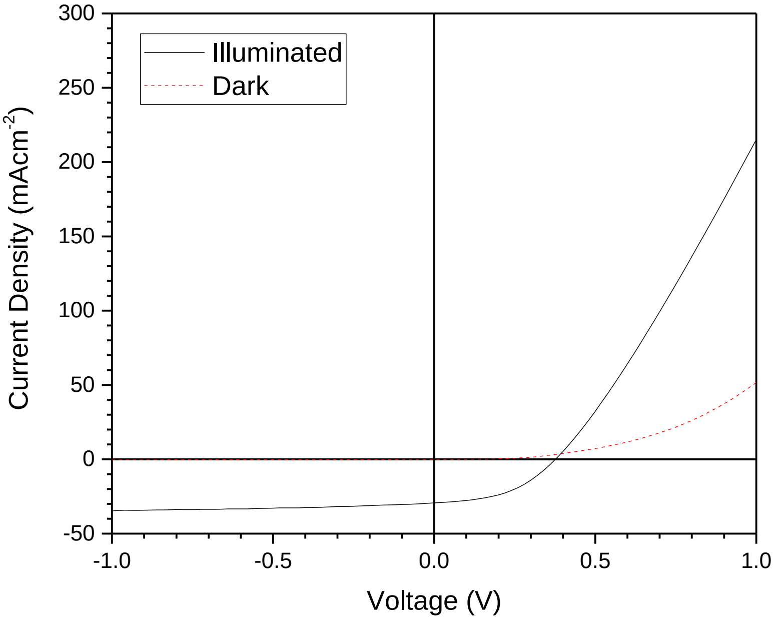

Figure 7.15: J-V response in the dark and under AM1.5 of the champion TEC15/ZnS/CdS/Sb_2Se_3/P3HT/Au device made in this work.

The data in Table 7.5 show the working parameters for the most efficient cells using CdS or ZnS/CdS as the window layer. The values for all parameters are greater in the ZnS/CdS device than the CdS one. The average values for each parameter across the champion device plate are shown in Table 7.6.

Table 7.5: Working parameters for the most efficient TEC15/CdS/Sb_2Se_3/P3HT/Au and TEC15/ZnS/CdS/Sb_2Se_3/P3HT/Au devices produced in this work.

Window Layer	PCE (%)	J_{sc} ($mAcm^{-2}$)	V_{oc} (mV)	FF (%)
CdS	4.32	27.4	360	44.9
ZnS/CdS	5.04	29.3	380	45.3

Table 7.6: Average working parameters for the cells on the device plate belonging to the champion 5.04% TEC15//ZnS/CdS/Sb_2Se_3/P3HT/Au device.

Parameter	Average Value
PCE	3.34±1.82%
V_{oc}	0.37±0.01 V
J_{sc}	23.8±7.0 $mA\cdot cm^{-2}$
FF	44.9±4.6%
R_s	55.6±17.8 $\Omega\cdot cm^2$
R_{sh}	626±157 $\Omega\cdot cm^2$

Figure 7.16 shows a comparison between the normalised EQE response from TEC15/CdS/Sb_2Se_3/P3HT/Au and TEC15/ZnS/CdS/Sb_2Se_3/P3HT/Au devices.

Both devices have shallower gradients on the long wavelength side than would be expected from pure-phase Sb_2Se_3. This is likely to do with some combination of intermixing of the CdS and Sb_2Se_3 layers and the presence of amorphous Sb_2Se_3. The CdS absorption shoulder is present in both curves, starting at the wavelength cut-off of CdS (≈ 510 nm). As expected, the device with the CdS only window layer has lower EQE in this region until the ZnS band gap (≈ 325 nm) is approached. Furthermore, the high-wavelength cut-off is shifted slightly towards lower wavelength (and hence higher energy) in the CdS only device, indicating widening of the band gap which may occur due to the introduction of S atoms in the Sb_2Se_3 layer. Both devices have a maximum wavelength cut-off of approximately 1040 nm (≈ 1.19 eV) and neither cell exhibits a sharp high-wavelength cut-off, indicative of S diffusion into the Sb_2Se_3 layer. The onset of the cut-off of the ZnS/CdS device is approximately 920 nm (≈ 1.34 eV) versus the 840 nm (≈ 1.48 eV) of the CdS only device suggesting that this diffusion is more severe in the CdS only device.

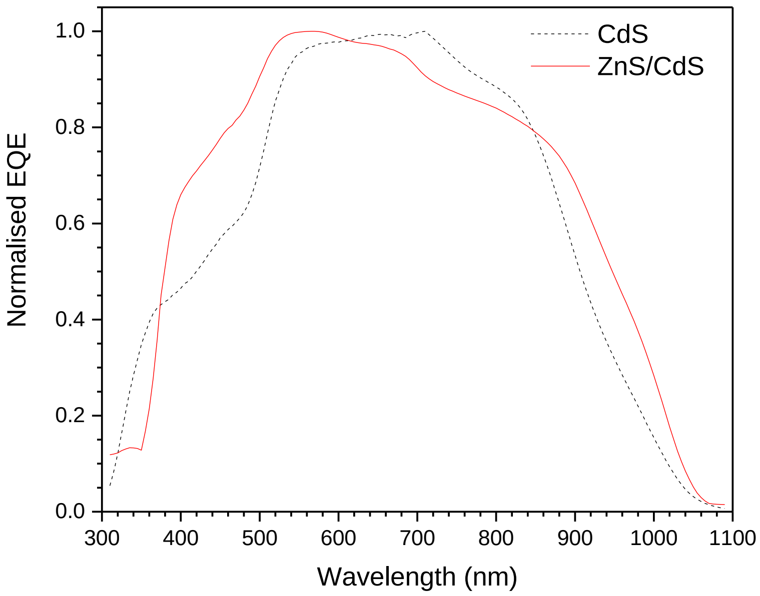

Figure 7.16: EQE data for the champion devices having CdS and Zns/CdS window layers. Both responses have been normalised.

Dark field STEM was performed on a FIB lift-out from a device having the structure TEC15/ZnS/CdS/Sb_2Se_3/P3HT/Au. Figure 7.17 shows an aberration corrected image taken with an accelerating voltage of 200 kV with a beam direction of [100]. In both the as-acquired and the FFT filtered image the van der Waals bonded sections are clearly visible as dark lines. The covalently bonded ribbons are clearly identifiable as the high contrast regions of the images. The image was processed as follows: Figure 7.17a) is the as-acquired image, this was converted to reciprocal space by an FFT using the Digital Micrograph programme to yield a pattern equivalent to an electron diffraction pattern. This was then filtered to remove intensity corresponding to non-periodic artefacts (i.e. image noise) to generate the image in Figure 7.17c). Finally, this is reverse transformed to give the clean image in Figure 7.17b) which shows the atomic positions much more clearly.

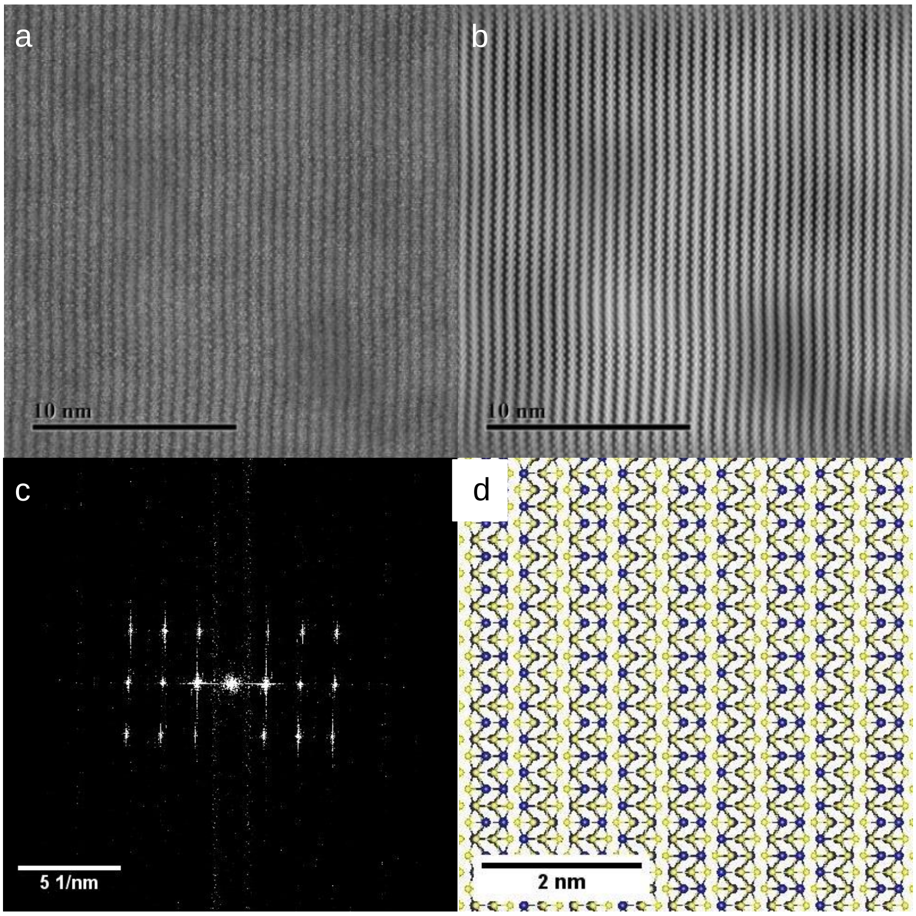

Figure 7.17: STEM dark field of the Sb_2Se_3 chains a) is the image as-acquired b) is the image after FFT filtering c) is the FFT of the image and d) is the VESTA model of Sb_2Se_3 viewed down the a-axis to match the beam direction in the TEM images.

Figure 7.18 shows a DF STEM image of an Sb_2Se_3 grain boundary. The chains are terminated at the grain boundary (i.e. there are wrong bonds at the grain boundary). Generally, it is expected that wrong bonds ae responsible for deep levels in the band gap of semiconductors and hence these levels may participate in recombination that is harmful to minority carrier device operation (e.g. SRH recombination). For the example shown in Figure 7.18 there was no evidence that the grain boundary has van der Waals bonding. The XRD of films presented in Chapter 6 does not display a single preferred texture axis and it may therefore be expected that these wrong bonded grain boundaries are common in the cells grown.

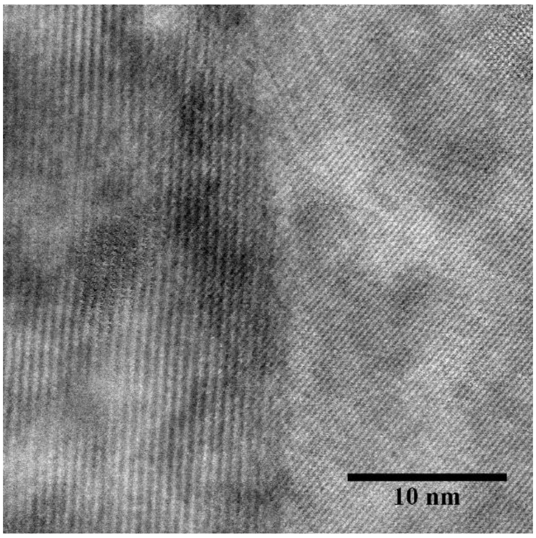

Figure 7.18: STEM image of a grain boundary in the Sb_2Se_3 layer.

The area of the device shown in the micrograph in Figure 7.19 was investigated using EDX spectroscopy. The micrograph shows distinct layers for each of the films deposited. Consulting the EDX data shown in Figure 7.20 the layers (from top to bottom in Figure 7.19) are composed of: Sn and O, the Sb signal seen here is most likely due to secondary fluorescence; Zn and S; Cd and S; Sb and Se; C; Au. These results are as expected from the device structure grown. Contrary to what is seen in the ToF SIMS data in Section 7.3.2, intermixing between the CdS and Sb_2Se_3 layers is not observed in the EDX data.

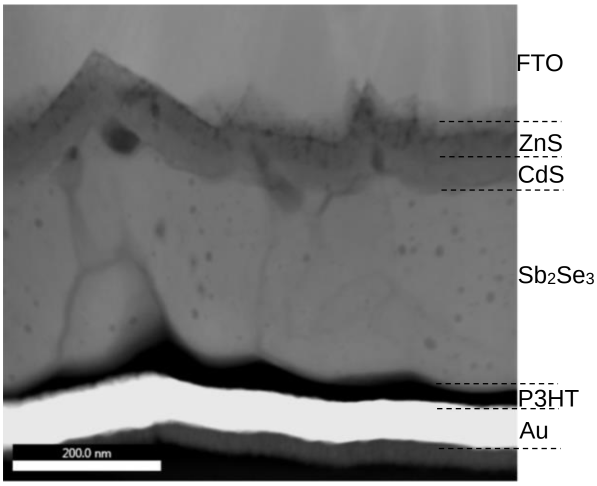

Figure 7.19: STEM image of the region for EDX analysis.

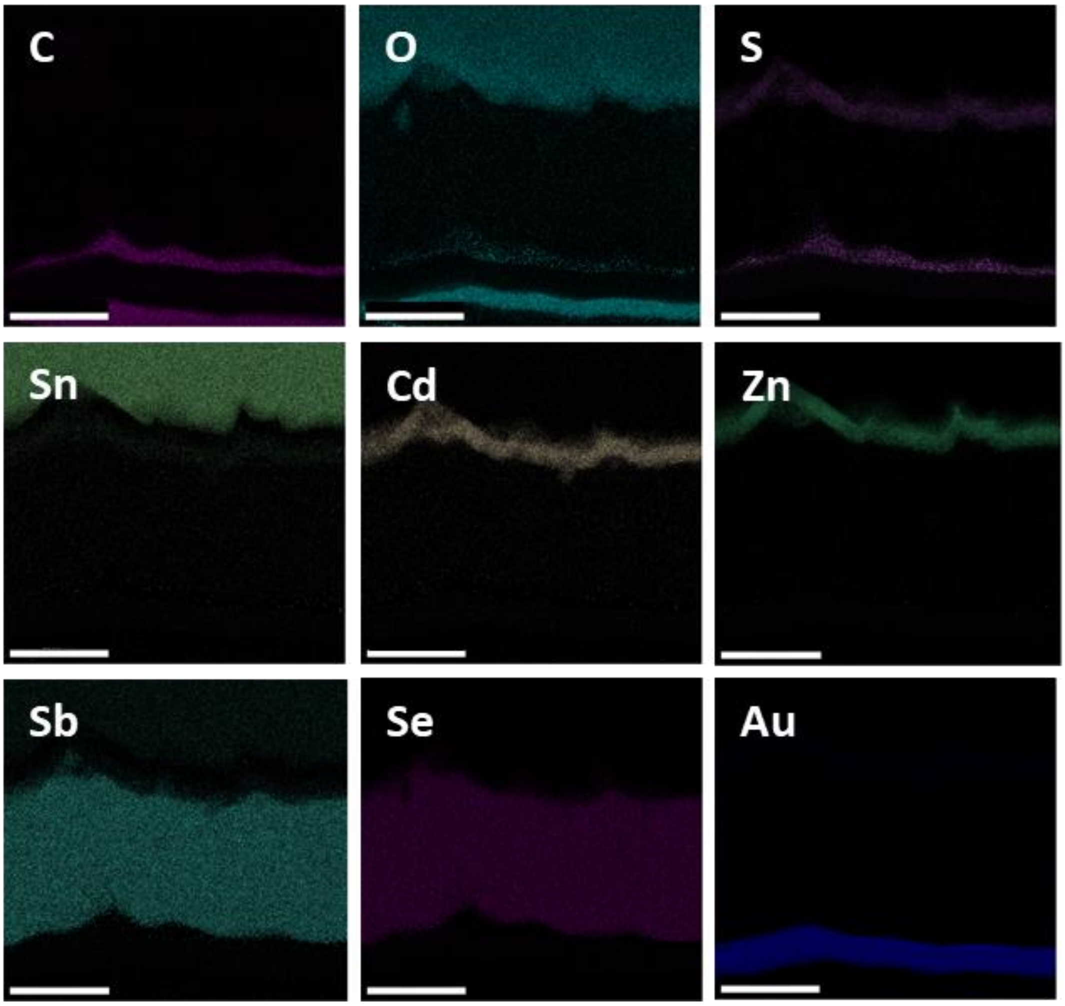

Figure 7.20: STEM/EDX data for the main elements in the SnO_2:F/ZnS/CdS/Sb_2Se_3/P3HT/Au structure. The scale bar represents 200 nm.

7.4 Discussion

Devices without the P3HT pinhole blocking layer completely shunted and therefore did not produce any photocurrent. The removal of or compensation for pinholes is vital in this material and thus P3HT layers have been used in all devices in this work. There are three main concerns when considering the addition of this layer. The first of these is the introduction of another layer and fabrication step into the process, introducing more variability into lab scale devices and more cost if the technology is to be scaled up for widespread distribution as a competitive PV material. The second concern is the cost of P3HT although there has been investigation into alternative polymers for application as a pinhole blocking layer so with further study it is possible that cheaper alternatives may be discovered somewhat nullifying this concern [2]. Lastly, the addition of another layer into the device adds series resistance into the system, reducing the fill factor of devices and hence hampering their performance. The drying step used for the P3HT appears to have a positive effect on the devices, though the lack of diode behaviour and photocurrent for the devices without P3HT make it difficult to conclude whether this is to do with the heat treatment's effect on the device as a whole or the P3HT itself.

When considering window layers, three were investigated here: ZnS, CdS, TiO_2, and a ZnS/CdS bilayer (the bilayer will be discussed later in this section). CdS and TiO_2 were both shown to be viable candidates as window layers for further work on this system. The efficiency, J_{sc}, V_{oc} and fill factor were observed to be lower across the board in the TiO_2 devices when compared to those made using CdS window layers. It is expected that the J_{sc} suffers in those CdS devices on account of the parasitic absorption in the CdS layer. Absorption in the CdS ($E_g = 2.42$ eV) prevents blue photons from being absorbed in the Sb_2Se_3 and therefore do not contribute to photocurrent generation. This is a known issue in CdS/CdTe devices and is often combatted by thinning of the CdS layer[1] or the use of tuneable band gap window layers[3,4]. The band gap of TiO_2 exceeds 3.0 eV [5] so the parasitic absorption is not a concern. Compared to the CdS/Sb_2Se_3 devices, however, the TiO_2/Sb_2Se_3 show lower J_{sc}, V_{oc}, *FF* and *PCE*. Other factors must therefore be more detrimental to performance in the devices having TiO_2 window layers than the absorption in those with CdS. ZnS was excluded for further study due to lack of photocurrent produced from devices incorporating is as a window layer. Notably, however, the devices produced with ZnS still formed a p-n junction and diode-like behaviour was observed. Since a photocurrent is observed in cells with other window layers its absence in ZnS devices is likely to do with poor electronic interface properties.

ToF SIMS was performed on device structures containing both CdS and TiO_2 window layers. Intermixing does appear to occur in both the device with a CdS window layer and that with a TiO_2 window layer since the species associated with the respective window layers are detected in the Sb_2Se_3 layer. Examination of the STEM image shown in Figure 7.19, however, reveals roughness in the Sb_2Se_3/window layer interface which may be responsible for this observation. Interdiffusion is understood to occur in CdTe devices where the CdTe layer can completely consume the CdS[6]. At the interface between the Sb_2Se_3 and TiO_2 layers there is a lower signal belonging to Ti and TiO species and a higher signal for O species compared to the bulk indicating that there may be an oxide-rich layer at this interface. The thickness of this layer in unclear, the sputtering time to pass through the TiO_2 layer is high (the sputtering rate is matrix dependent. If this is not the case the oxide may impede charge transport and thereby reduce the performance of the device which would be in agreement with the characteristics observed in the J-V data. Further optimisation of the TiO_2 layer in this system may result in higher performing devices due to the removal of the parasitic absorption associated with the CdS window layer however for the purposes of this work, on account of the vastly superior performance, work on CdS/Sb_2Se_3 devices was pursued.

The s-shaped curves produced in the TiO_2 devices are also observed in other technologies. Generally, such curves indicate a barrier to transport. For example, Sundqvist reports the occurrence of these characteristics in inverted organic solar cells with a TiO_2 electron transport layer[7]. As in the devices shown in this work, s-shaped curves were observed in pristine devices and light quenching was seen to remove this behaviour. The authors attribute this to the high work function of the TCO/TiO_2 contact causing the accumulation of holes at the TiO_2/organic interface giving rise to increased recombination. Exposure to UV light then reduces the work function at the interface, reducing the hole accumulation, the recombination rate and hence removing the s-shaped characteristic and increasing the efficiency of the devices.

As shown in Section 6.3, when deposited by thermal evaporation the Sb_2Se_3 forms amorphous layers on room temperature substrates and therefore requires an annealing step to form a crystalline film. Annealing conditions of 250 and 450°C both resulted in poor device performance due to severely s-shaped J-V curves. An annealing temperature of 300°C produced devices with the highest V_{oc} and fill factors of all the conditions investigated, however poor J_{sc} prevented the devices from having high PCEs. The most promising efficiencies were obtained from devices annealed at 350°C, however the true ideal temperature probably lies between 350 and 400°C. The variability of the crystal texture present caused by small changes in the annealing temperature of the post-growth step shown in Section 6.3.2 are likely to outweigh any advantage gained from optimising this further so the annealing step for further production of devices was carried out at 350°C.

Variability across the cells in a device plate was fairly significant in the standard size (2.5×2.5 cm^2) produced in this work; the maximum, average and standard deviation of efficiency of a typical 16 cell device being 2.85%, 1.95% and 0.9% respectively (taken from the CdS device in Section 7.3.2). Devices with four times the area were grown using both CdS and TiO_2 window layers and characterised. Both types of device showed significant variation across the surface with the efficiency variation map matching the J_{sc} map and to a lesser extent the fill factor. V_{oc} values are comparatively constant across the device. Since it is J_{sc} which is predominantly affected, the issue is likely to be one of recombination or absorption. If recombination is an issue the non-uniformity probably arises from the annealing step which is known to produce different orientations across the area of the device: the recombination centres due to covalent grain boundaries may be more prevalent in those regions with orientations where the Sb_2Se_3 ribbons lay flat on the substrate. A similar situation is observed in the TiO_2/Sb_2Se_3 devices indicating that the non-uniformity is not dependent on the window layer. Another potential source of the inconsistency in the fabrication of these large area devices is the spin coating of

P3HT. A good indicator of this being the cause would be a radial variation in the number of shunting pixels – there is no strong evidence of this, however.

Liu reports that growing films Se rich should increase performance[8], the defects giving rise to deep level traps being V_{Se} and Sb_{Se}. Furthermore, since the most energetically favourable defects are the antisites Sb_{Se} and Se_{Sb} with the latter being a shallow acceptor (potentially contributing beneficially to p-doping) mean that if the Sb_{Se} defect is adequately compensated for, the device performance should increase. Indeed, they report improvement by in situ Se compensation and achieved a record efficiency for the material at the time of their paper. Similar results are reported by Li[9] produced by the co-evaporation of Sb_2Se_3 and elemental Se. The Sb-rich devices do indeed have lower J_{sc} than their pure Sb_2Se_3 and Se-rich counterparts as would be expected due to the creation of Sb_{Se} and V_{Se} defects, however there is no evidence of the improvement of devices by the introduction of Se by co-evaporation using the setup from this work. This may, however, be due to the increased fraction of grains oriented with Sb_2Se_3 ribbons oriented parallel to the substrate whose presence is indicated by the higher intensity (120) peak seen in the Se-rich film's XRD spectrum. This may negate any benefits from stoichiometric control by encouraging grain boundaries containing recombination centres.

The flux of Se in the co-evaporation also adds another variable to the system which is already difficult to control. There are fluctuations in the deposition rate given constant power supplied to the source so constant adjustment is required for a constant rate. This is less of a problem for single source evaporations in thermally evaporated films since the microstructure originates from post-growth annealing, however the introduction of a second source may produce variation in composition through the depth of the film. The system used by Liu in their report was custom-made for the purpose of producing these Sb_2Se_3 devices (full details of the system are not supplied beyond that the Se source has variable position) so a similar apparatus may be required for noticeable improvement in this system.

The thinning of the CdS reported in Section 7.3.6 was shown to reduce the parasitic absorption in the CdS, offsetting the additional absorption by the ZnS layer by enough to give a measurable increase in device performance. The addition of the bilayer increased both the J_{sc} and V_{oc} resulting in a higher efficiency. In this TEC15/ZnS/CdS/Sb_2Se_3/P3HT/Au device no evidence of intermixing was observed when investigated with TEM/EDX. This is in contrast with the data from the ToF SIMS on the TEC15/CdS/Sb_2Se_3 structure. The discrepancy here may due to craters forming in the material during the SIMS operation, resulting in different depths of the sample being sputtered simultaneously.

The champion device produced in this work has an efficiency of 5.04% from an active area of 0.1 cm^2. The record efficiency at the time of writing for this technology is 7.6% produced by a "Vapour Transport Deposition" technique is reported by Wen[10] and the record for CSS growth is 6.6% reported by Hutter[11]. For the devices reported in this thesis the V_{oc} and J_{sc} values are approaching those of the record devices but the fill factor is limited.

The main obstacles for the devices presented here are consistency of devices and the limiting of the parasitic absorption in the CdS window layer observed in the EQE, though somewhat alleviated by thinning of the CdS layer and the addition of a thin ZnS to prevent shunting. Increased consistency may be achieved using more specialised heating apparatus for the post-growth annealing step and, if successful, allowing for finer tuning of the process. The parasitic losses from absorption in the CdS layer are more problematic since the CdS layer is already thin (~50 nm) and at least half of this thickness is lost to the Sb_2Se_3 intermixing observed in the SIMS data (Section 7.3.2). TiO_2 would be expected to be a good candidate for replacement since it has been shown here to produce devices with >1% efficiency and, indeed, it is the partner layer of choice in the most efficient CSS-grown devices[11]. The RTE-grown devices[12] use CdS partner layers but uses a colloidal PbS quantum dot film as the hole transport material in place of the P3HT used in this work - this may account for some of the differences.

7.5 Conclusions

Sb_2Se_3 devices have successfully been made by thermal evaporation. The necessity of a pinhole blocking layer, such as P3HT, in devices grown by the thermal evaporation method has been demonstrated. ZnS, CdS and TiO_2 have been investigated as potential n-type partner layers for the Sb_2Se_3. ZnS was unsuccessful due to lack of photocurrent in the devices produced. Both TiO_2 and CdS were shown to be viable, however CdS showed much more immediate promise and was thus pursued. The post-growth annealing process necessary for the production of crystalline Sb_2Se_3 was investigated in the range 250-450°C and the value of 350°C was found to produce the best devices. The heating process was, however speculated to be the main cause of the poor consistency of performance across the area of the devices produced. Devices were grown Sb- and Se-rich by co-evaporation; in agreement with theory, the Sb-rich devices exhibited lower J_{sc} and this was likely to be due to recombination effects. Se-rich devices, however, were not found to have better performance than those grown from a single compound source in this experimental setup. The champion device produced was 5.04% efficient though there is still room for improvement through the optimisation of the window layer.

Table 7.7: A summary of the optimisation steps carried out for evaporated Sb_2Se_2 PV devices.

Optimisation Step	**Results**
Inclusion of the P3HT layer	P3HT was found to be near essential for the growth of working devices from evaporated Sb_2Se_3. Annealing at 150°C for 10 minutes post-P3HT deposition was found to be beneficial.
Post Sb_2Se_3 deposition anneal	Annealing the Sb_2Se_3 films post deposition substantially increases the efficiency of devices. A 350°C anneal for 30 minutes was optimal.
Off-stoichiometric growth	Growing Sb-rich films produced substantially lower efficiency devices than stoichiometric Sb_2Se_3 films. Growing Se-rich films produced slightly lower efficiency devices than stoichiometric Sb_2Se_3 films.
Window layer choice	Of the three window layers investigated ZnS was the least successful, photocurrent was not observed. Both CdS and TiO_2 window layers produce good devices. The performance of devices may be improved further by the use of a ZnS/CdS bilayer of the same total thickness as the original CdS layer.

References for Chapter 7

1. Mohamed, H. A., Mohamed, A. S. & Ali, H. M. Theoretical study of ZnS/CdS bi-layer for thin-film CdTe solar cell. *Mater. Res. Express* **5**, 056411 (2018).

2. Hutter, O. S., Phillips, L. J., Durose, K. & Major, J. D. 6.6% Efficient Antimony Selenide Solar Cells Using Grain Structure Control and an Organic Contact Layer. *Sol. Energy Mater. Sol. Cells* **188**, 177–181 (2018).

3. Wang, T., Ren, S., Li, C., Li, W., Liu, C., Zhang, J., Wu, L., Li, B. & Zeng, G. Exploring window buffer layer technology to enhance CdTe solar cell performance. *Sol. Energy* **164**, 180–186 (2018).

4. Kartopu, G., Clayton, A. J., Brooks, W. S. M., Hodgson, S. D., Barrioz, V., Maertens, A., Lamb, D. A. & Irvine, S. J. C. Effect of window layer composition in $Cd_{1-x}Zn_xS$/CdTe solar cells. *Prog. Photovoltaics Res. Appl.* **22**, 18–23 (2018).

5. Scanlon, D. O., Dunnill, C. W., Buckeridge, J., Shevlin, S. A., Logsdail, A. J., Woodley, S. M., Catlow, C. R. A., Powell, M. J., Palgrave, R. G., Parkin, I. P., Watson, G. W., Keal, T. W., Sherwood, P., Walsh, A. & Sokol, A. A. Band alignment of rutile and anatase TiO_2. *Nat. Mater.* **12**, 798–801 (2013).

6. Romeo, A., Bätzner, D. L., Zogg, H. & Tiwari, A. N. Recrystallization in CdTe/CdS. *Thin Solid Films* **362**, 420–425 (2000).

7. Sundqvist, A., Sandberg, O. J., Nyman, M., Smått, J. H. & Österbacka, R. Origin of the S-Shaped JV Curve and the Light-Soaking Issue in Inverted Organic Solar Cells. *Adv. Energy Mater.* **6**, 1–7 (2016).

8. Liu, X., Xiao, X., Yang, Y., Xue, D. J., Li, D. B., Chen, C., Lu, S., Gao, L., He, Y., Beard, M. C., Wang, G., Chen, S. & Tang, J. Enhanced Sb_2Se_3 solar cell performance through theory-guided defect control. *Prog. Photovoltaics Res. Appl.* **25**, 861–870 (2017).

9. Li, Z., Zhu, H., Guo, Y., Niu, X., Chen, X., Zhang, C., Zhang, W., Liang, X., Zhou, D., Chen, J. & Mai, Y. Efficiency enhancement of Sb_2Se_3 thin-film solar cells by the co-evaporation of Se and Sb_2Se_3. *Appl. Phys. Express* **9**, (2016).

10. Wen, X., Chen, C., Lu, S., Li, K., Kondrotas, R., Zhao, Y., Chen, W., Gao, L., Wang, C., Zhang, J., Niu, G. & Tang, J. Vapor transport deposition of antimony selenide thin film solar cells with 7.6% efficiency. *Nat. Commun.* **9**, (2018).

11. Hutter, O. S., Phillips, L. J., Durose, K. & Major, J. D. 6.6% Efficient Antimony Selenide Solar Cells Using Grain Structure Control and an Organic Contact Layer. *Submitt. to Sol. Energy Mater. Sol. Cells* **188**, 177–181 (2018).

12. Chen, C., Wang, L., Gao, L., Nam, D., Li, D., Li, K., Zhao, Y., Ge, C., Cheong, H., Liu, H., Song, H. & Tang, J. 6.5% Certified Efficiency Sb_2Se_3 Solar Cells Using PbS Colloidal Quantum Dot Film as Hole-Transporting Layer. *ACS Energy Lett.* **2**, 2125–2132 (2017).

8. Summary, Conclusions and Suggestions for Future Work

8.1 Results summary

8.1.1 Cu_3BiS_3

In this work Cu_3BiS_3 was grown on glass and Mo by the sulfurisation of thermally evaporated metal “precursor film” stacks. The tolerance to composition and temperature was shown to be high when producing phase-pure films of the material. Device structures were made using both glass/Mo/Cu_3BiS_3/ZnS/ITO and glass/Mo/Cu_3BiS_3/CdS/ITO structures. The ZnS window layer devices were shown to produce diode-like behaviour, whereas the CdS window layer devices did not due to a combination of shunting and poor band structure at the interface. In neither case, however, was a measurable photocurrent produced.

8.1.2 Sb_2Se_3 films

Sb_2Se_3 was shown to deposit as an amorphous film by thermal evaporation onto both glass and CdS. High substrate temperatures (≥ 500°C) or an annealing step were required to produce crystalline material. Films could be templated somewhat by growth onto highly ordered (wafers of (100) InP) substrates, however this preferred orientation was not maintained through an annealing step. There was found to be run-to-run inconsistency in the orientations of the Sb_2Se_3 produced by the annealing step.

8.1.3 Sb_2Se_3 devices

Devices with the structure TEC15/window/Sb_2Se_3/P3HT/Au were grown, the window layers used were: CdS, ZnS, TiO_2 or ZnS/CdS. Devices with ZnS did not produce a measurable photocurrent, the other three combinations did, however. The impact of annealing temperature on device performance was investigated and a value of 350°C was found to produce the best performing devices. Parasitic absorption in the CdS window layer was shown to be reduced by the thinning of the layer from 50 to 25 nm and the addition of a 25 nm layer of ZnS to prevent shunting and reduce reflection losses. The champion device produced had an efficiency of 5.04%.

8.2 Discussion and conclusions

8.2.1 Cu_3BiS_3

Other authors have confirmed the formation of single phase Cu_3BiS_3 films by sulfurisation of metal[1,2]. With a H_2S sulfurising gas the authors report ideal conditions of 270°C for heating times exceeding 16 hours in a 5 Torr H_2S/5 Torr Ar atmosphere[1]. With elemental sulfur instead as the sulfurisation gas the required sulfurisation time is reduced significantly to 30 minutes albeit with temperatures of 450°C and above necessary[2]. The authors suggested the difference in conditions for the production of pure phase is due to the difference in partial pressures on the sulfurisation gasses. However, since the Gibbs free energy of reaction starting from elemental sulfur is expected to be greater than for the H_2S, the former is expected to promote reaction more strongly. Further to these observations, in this work a broad range of conditions are also presented which successfully generate the desired phase:

growth of single phase Cu_3BiS_3 appears to be achievable relatively easily by a variety of methods. Facile growth of materials is an extremely desirable property in a material due to the ability to tailor the conditions used to match those from other steps in the process of making full device structures. The conformity and adherence issues observed in multiple studies are only seen here at the extremes of the tolerance range in compositions at each temperature.

As previously stated in Section 3.1 the literature reports of working devices having Cu_3BiS_3 as the active layer are limited to one dye cell and one planar heterojunction, neither of which are have high efficiency. The devices produced by this study demonstrate the presence of a p-n junction but not a photocurrent; similarly, the device produced by Hernádez-Mota shows diode-like behaviour but has extremely low photocurrent[3]. This low (or lack of) photocurrent may be due to either low carrier lifetimes or the devices having a field position, carrier lifetime or else a collection issue. The latter may make the form of a buried junction (i.e. inaccessible to the light) or else a collapsed junction in which the conductivity of the absorber is high, and the depletion width is very low. For the case of their sulfurisation-grown Cu_3BiS_3 devices Colombara presents an investigation of the photoelectrochemical properties of the material. The EQE measurement performed using a $Eu(NO_3)_3$ electrolyte did not exceed 12%. Since in this system the junction position is at the interface between the Cu_3BiS_3 and the electrolyte, the low EQE is likely to be due to poor carrier lifetimes rather than due to poor junction position. One study has been performed to investigate the trap states in the material using thermally stimulated conductivity which shows nine deep traps having high

($>10^{17}$ cm^{-3}) densities[4]. These deep levels are likely to contribute to SRH recombination which would explain the low EQE and very poor or absent photocurrent. Ideally a DFT study into the origins of these defects would aid in establishing the identities of and hence possible methods of compensation for these defects. There are, however, potentially too many of these problematic traps to compensate for, ultimately meaning that the material has weaker prospects than its band gap and absorption coefficient would suggest.

Synthesis of Cu_3BiSe_3 was, in contrast with the sulfide analogue, not achieved here. While it does feature in a scarcely reported in more comprehensive publications on the Cu-Sb/Bi-S/Se system[5]. The Cu_3BiSe_3 phase was created by Babanly by a process of incongruent melting, alloying and annealing of binary compounds[6]. There are no reports of producing the phase by a chalcogenisation process and it may be the case that Cu_3BiSe_3 cannot be made by selenisation.

- The Cu:Bi composition tolerance windows for 375, 400 and 425°C sulfurisation temperatures are 9:5 to 9:2, 9:4 to 18:5 and 18:7 respectively. Sulfurisation at 450°C and above did not produce films of high enough quality to do phase identification. Films sulfurised at temperatures from 375-425°C had good film adhesion Cu:Bi 6:1 through to 3:2, the most Bi-rich ratio tested. As a result of this large tolerance region, the conditions for growth may be selected in accordance with the needs of the other processes. If these processes are not restrictive then the sulfurisation may be performed at 375°C since it has the widest tolerance range.

- When sulfurising precursor stacks on Mo substrates instead of plain soda-lime glass, additional XRD peaks were observed not belonging to the desired phase. These were attributed to a (002) $CuBiS_2$ and a (111) Cu orientation and were observed to be produced for conditions which resulted in phase-pure films on glass (375°C, atomic Cu:Bi 9:4). Both of these phases were observed in Bi-rich films on glass and but not in films grown with reduced Bi precursor content (375°C, atomic Cu:Bi 3:1). These conditions were used to grow Cu_3BiS_3 films on Mo for the fabrication of complete device structures.
- Devices with Cu_3BiS_3 as the absorber layer were grown using the conditions shown to produce phase-pure Cu_3BiS_3 on Mo substrates. The device structures chosen for investigation were glass/Mo/Cu_3BiS_3/CdS/ITO and glass/Cu_3BiS_3/ZnS/ITO. The devices with the former structure presented current-voltage behaviour indicative of shunting pathways though the device. The devices with the latter were shown to have diode-like current-voltage response but no measurable photocurrent.

8.2.2 Sb_2Se_3

The motivation for investigation of Sb_2Se_3 as a PV absorber material was predicated on its structure and thus the possibility for electrically benign grain boundaries. Accordingly, orientation control of the material would be necessary to access this potential. In their 2014 paper Benjamin et al. report a change in orientation produced in different temperature zones of the LPCVD used to grow Sb_2X_3 (X = Se, Te) films. Evidence of this is presented for Sb_2Te_3 having variation in orientations with respect to temperature produced by this method, though has a different space group ($R\bar{3}m$) with a 2D structure. Only one Sb_2Se_3 XRD pattern is presented from which conclusions about orientation control cannot be drawn.

Conductivity anisotropy in Sb_2Se_3 has been demonstrated by Kosek [7] and while it has not been demonstrated for work function, it is expected to be present in the material. Orientations with the Sb_2Se_3 ribbons parallel to the film surface will lead to increased series resistance in the devices. More vitally, with the work function at the surface changing the relative band positions at the interface will vary also. This variation will affect the matching of partner layers thus making the correct choice of materials extremely difficult unless precise control of the orientation is possible.

In this work, the deposition and post growth annealing of Sb_2Se_3 was investigated. It was observed that the material was very sensitive to the heating conditions in the annealing step. This sensitivity manifests in run-to-run difference between the phases obtained in the polycrystalline films after the post-growth anneal step and, contrastingly, common textures in separate samples annealed simultaneously. Films and devices consequently are irreproducible using the methods presented here and available equipment. At laboratory-scale this variability is impactful due to reliability concerns when comparing devices to controls and each other. On an industrial scale this may be even more restrictive due to the need for conformity across large areas and between modules and the material's sensitive nature being at odds with this.

- Sb_2Se_3 films were grown onto soda-lime glass substrates having substrate temperatures in the range 24-550°C. XRD data showed the appearance of crystalline peaks for Sb_2Se_3 at temperatures at and above 500°C, agreeing with the apparent shift in optical absorption observed in the UV-Vis-NIR data obtained from the same samples.

- An alternative solution for the production of crystalline films was the post-growth annealing of the films. The substrate temperature during deposition was not found to be a factor in the crystallographic texture of the films. A large degree of the crystallographic texture variation was observed to be due to the annealing step, however there was no discernible relationship of texture with temperature. Rather, small variations in annealing conditions which are very difficult to avoid on a hotplate lead to vastly different crystallographic textures in the annealed films.
- Due to the initial promise shown by Sb_2Se_3 devices with CdS window layers, the structure TEC15/CdS/Sb_2Se_3/P3HT/ITO was pursued. CdS is known to reduce device performance by the absorption of light in the approximate range of 300-500 nm. This behaviour was observed in the Sb_2Se_3 devices grown in this work even with the CdS layer being thin (50 nm) so an alternative was sought. The use of a ZnS/CdS bilayer with the same total thickness as the original CdS layer was able to reduce the parasitic absorption and hence increase performance.
- The champion device produced in this work had structure TEC15/ZnS/CdS/Sb_2Se_3/P3HT/Au. The device had an efficiency of 5.04%, J_{sc} of 29.3 mA·cm^{-2}, V_{oc} of 380 mV and fill factor of 45.3%.

8.2.3 Comparison of the two materials

Of the two materials investigated in this work, Sb_2Se_3 is by far the most promising candidate. The first reason for Sb_2Se_3 being more successful than Cu_3BiS_3 could be ease of phase control in a binary over a ternary compound. The second may be the presence of multiple deep level traps in Cu_3BiS_3. The XRD data taken in this work indicates that the Cu_3BiS_3 films can be made phase-pure and hence the phase control is not considered likely to be the main culprit for the material's lack of performance. The deep level traps in Cu_3BiS_3, on the other hand, are a serious concern and if the material is to see further study it is imperative that the trap states are better understood so that they may be compensated for. Sb_2Se_3, however, with neither of these factors being as detrimental is instead limited somewhat by orientation control issues. While difficult, fine control over the temperature is expected to be key.

8.3 Recommendations for future work

- Since the basic optical and electronic properties of Cu_3BiS_3 are well established in the literature, focus on the material in the field of photovoltaics must therefore shift towards the production of functional devices. The author suggests that, in light of factors discussed in this thesis, the primary concern to be addressed is the origin of the lack of photocurrent. Two obstacles for the material are trap type and density and carrier lifetimes. The traps in Cu_3BiS_3 may be studied by a combination of theoretical, e.g. density functional theory (DFT), and practical, e.g. deep level transient spectroscopy (DLTS), techniques. Carrier lifetime may be investigated using a technique such as timeresolved photoluminescence. Once these properties of the material have been established it is possible that the reasons for the lack of photocurrent may be uncovered, compensated for and their effects on device performance observed.

- A primary concern in the Sb_2Se_3 films and devices was the inconsistency in the Sb_2Se_3 orientations produced during the annealing step required to produce crystalline films. In other materials orientation is not so much of a concern but the anisotropy of Sb_2Se_3 leads to its increased importance. The starting point for investigation of this orientation control is suggested to be the development of a system with a N_2 atmosphere and with precise control of temperature within its volume.
- Due to the success of the ZnS/CdS window bilayer presented here, alternative window layers may be investigated. Potential candidates may be those with tuneable band gaps such as $Mg_xZn_{1-x}O$, $Cd_xZn_{1-x}S$ or CdS:O. The relative success of CdS-containing devices in this work would suggest that $Cd_xZn_{1-x}S$ or CdS:O would be the most reasonable starting points.
- The fill factors in the devices with Sb_2Se_3 window layers were low. The origin of these low values is likely due to the presence of pinholes in the layers reducing the shunt resistance (this may be seen in the low values of R_{sh} reported in Section 7.3.6). Furthermore, as shown in Section 7.3.1, the presence of pinholes necessitates the use of a pinhole blocking layer (P3HT here) which is both expensive and a source of additional series resistance in the devices. The investigation

of methods to improve the structure of the deposited films, the reduction of material-loss during the annealing step or other means for blocking pinholes may facilitate the omission of the P3HT layer. The resulting reduction in R_s and increase of R_{sh} may increase fill factor and hence device efficiency.

References for Chapter 8

1. Gerein, N. J. & Haber, J. A. Synthesis of Cu_3BiS_3 Thin Films by Heating Metal and Metal Sulfide Precursor Films under Hydrogen Sulfide. *Chem. Mater.* **18**, 6289–6296 (2006).
2. Colombara, D., Peter, L. M., Hutchings, K., Rogers, K. D., Schäfer, S., Dufton, J. T. R. & Islam, M. S. Formation of Cu_3BiS_3 thin films via sulfurization of Bi–Cu metal precursors. *Thin Solid Films* **520**, 5165–5171 (2012).
3. Hernádez-Mota, J., Espíndola-Rodríguez, M., Sánchez, Y., López, I., Peña, Y. & Saucedo, E. Thin film photovoltaic devices prepared with Cu_3BiS_3 ternary compound. *Mater. Sci. Semicond. Process.* **87**, 37–43 (2018).
4. Dussan, A., Murillo, J. M. & Mesa, F. Thermally stimulated conductivity of Cu_3BiS_3 thin films deposited by co-evaporation: Determination of trap parameters related to defects in the gap. *J. Mater. Sci.* **47**, 6688–6692 (2012).
5. Yu, L., Kokenyesi, R. S., Keszler, D. A. & Zunger, A. Inverse design of high absorption thin-film photovoltaic materials. *Adv. Energy Mater.* **3**, 43–48 (2013).
6. Babanly, N. B., Yusibov, Y. A., Aliev, Z. S. & Babanly, M. B. Phase equilibria in the Cu-Bi-Se system and thermodynamic properties of copper selenobismuthates. *Russ. J. Inorg. Chem.* **55**, 1471–1481 (2010).
7. Kosek, F., Tulka, J. & Štourač, L. Optical, photoelectric and electric properties of single-crystalline Sb_2Se_3. *Czechoslov. J. Phys.* **28**, 325–330 (1978).